NASA CR-120858

# EXPERIMENTAL QUIET ENGINE PROGRAM AERODYNAMIC PERFORMANCE OF FAN A

(NASA-CR-120858) EXPERIMENTAL QUIET ENGINE PROGRAM AERODYNAMIC PERFORMANCE OF FAN A
R.G. Giffin, et al (General Electric Co.)
May 1971 112 p CSCL 21E
N72-26695
Unclas
G3/28 33583

by

R.G. Giffin, D.E. Parker, and L.W. Dunbar

GENERAL ELECTRIC COMPANY

prepared for

NATIONAL AERONAUTICS AND SPACE ADMINISTRATION

Reproduced by
NATIONAL TECHNICAL
INFORMATION SERVICE
U S Department of Commerce
Springfield VA 22151

NASA-Lewis Research Center
Contract NAS 3-12430
Arthur A. Medeiros, Project Manager

115

1. Report No.
NASA CR-120858

2. Government Accession No.

3. Recipient's Catalog No.

4. Title and Subtitle
Experimental Quiet Engine Program Aerodynamic Performance of Fan A

5. Report Date
May 1971

6. Performing Organization Code

7. Author(s)
Giffin, R.G., Parker, D.E. and Dunbar, L.W.

8. Performing Organization Report No.

9. Performing Organization Name and Address
General Electric Company
Aircraft Gas Turbine Division
Cincinnati, Ohio 45215

10. Work Unit No.

11. Contract or Grant No.
NAS3-12430

12. Sponsoring Agency Name and Address
National Aeronautics and Space Administration
Washington, D.C. 20546

13. Type of Report and Period Covered
Contractor Report

14. Sponsoring Agency Code

15. Supplementary Notes
Project Manager, Arthur A. Medeiros,
V/STOL & Noise Division
NASA Lewis Research Center
Cleveland, Ohio

16. Abstract

This report presents the aerodynamic component test results of Fan A, one of two high-bypass-ratio, 1160 feet per second (353.6 m/sec) single-stage fans, which was designed and tested as part of the NASA Experimental Quiet Engine Program. This fan was designed to deliver a bypass pressure ratio of 1.50 with an adiabatic efficiency of 86.5% at a total fan flow of 950 lb/sec (430.9 kg/sec). It was tested with and without inlet flow distortion. A bypass total-pressure ratio of 1.52 and an adiabatic efficiency of 88.3% at a total fan flow of 962 lb/sec (436.4 kg/sec) were actually achieved. An operating margin of 12.4% was demonstrated at design speed.

17. Key Words (Suggested by Author(s))
Fan, Compressor, Inlet Flow Distortion, Aerodynamic Performance

18. Distribution Statement
Unclassified - Unlimited

19. Security Classif. (of this report)
Unclassified

20. Security Classif. (of this page)
Unclassified

21. No. of Pages
112

22. Price*
$7.75

*For sale by the National Technical Information Service, Springfield, Virginia 22151

## TABLE OF CONTENTS

# LIST OF ILLUSTRATIONS

## LIST OF ILLUSTRATIONS (Continued)

## LIST OF ILLUSTRATIONS (Concluded)

# 1.0 SUMMARY

This report presents the aerodynamic component test results of Fan A, one of two high-bypass-ratio, 1160 feet per second (353.6 m/sec) single-stage fans, which was designed and tested as part of the NASA Experimental Quiet Engine Program. The fan was tested with an undistorted inlet flow and with circumferential, tip radial, and crosswind distortions. The hub tip radius ratio was 0.465 at rotor inlet. A flow splitter, immediately downstream of the rotor, separates the fan bypass flow from the fan core flow. An axial distance equal to two rotor chords was employed between the rotor and bypass portion outlet guide vanes (OGV). The vane-number-to-blade-number ratio was 2.3. No inlet guide vanes were employed.

The fan was designed to deliver a bypass total-pressure ratio of 1.50 at a total fan flow of 950 lb/sec (430.9 kg/sec). The design bypass adiabatic efficiency was 86.5%. A bypass portion total-pressure ratio of 1.52 and an adiabatic efficiency of 88.3% at a total flow of 962 lb/sec (436.4 kg/sec) were actually achieved. The fan core region was designed to develop a total-pressure ratio of 1.32 at a flow of 144.0 lb/sec (65.3 kg/sec). A fan core portion pressure ratio of 1.356 was actually achieved at its design flow. At this condition, a fan core adiabatic efficiency of 83.1% was measured.

The operational limit line was determined up to 100% corrected speed. Rotating stall was the operational limit at all speeds except 100% where high bypass OGV stress precluded further increases in back pressure. At 100% corrected speed, an operating margin of 12.4% was achieved relative to the design operating line at altitude-cruise conditions and at 90% corrected speed the operating margin was 10.8% relative to the design operating line at sea-level-static conditions.

The fan was tested with one-per-rev circumferential, tip radial, and crosswind distortion screens installed. At 90% corrected speed, the screens were found to produce approximately 15% distortion (maximum minus minimum pressure divided by maximum pressure). The fan demonstrated minimal operating margin loss to one-per-rev circumferential and crosswind distortions. The tip radial distortion resulted in a substantial operating margin degradation.

## 2.0 INTRODUCTION

In the last 20 years the rapid growth of the commercial aviation industry has demanded large increases in aircraft size and flight frequency. This, coupled with the increased public awareness of the noise pollution problem, has prompted the initiation of an Experimental Quiet Engine Program by the NASA-Lewis Research Center (Contract NAS3-12430). The major objectives of this program are: the demonstration of noise levels produced by turbofan engines which are designed for low noise output and confirmation that predicted noise reduction can be achieved; demonstration of the technology and design innovations which will reduce the production and radiation of noise in high-bypass turbofan engines; and acquisition of experimental acoustic and aerodynamic data for turbofan engines, which are designed for low noise output, to give a basis for correction of acoustic theory and experiment and to give a better understanding of the noise production mechanisms in fans, compressors, turbines, and nozzles.

Observations of past trends indicate that as tip speed increases, at constant aerodynamic loading, fan broadband noise increases. Also, at constant tip speed, a reduction in aerodynamic loading is observed to decrease fan pure tone noise. Hence, for given mission requirements, the minimum fan noise configuration requires consideration of the weighted sum of the two types of noise. In order to confirm acoustic noise predictions and to acquire acoustic and aerodynamic data for typical high-bypass fans two low-speed fans, designated Fan A and Fan B, and one low-aerodynamic-loading fan, designated Fan C, were designed.

The aerodynamic performance of the three fans has been determined in the General Electric Large Fan Test Facility in Lynn, Massachusetts. Upon completion of the aerodynamic testing, each fan, in turn, is to be tested in the NASA-Lewis Acoustic Test Facility.

Fan A, one of the low-speed fans, and the low-aerodynamic-loading Fan C are to be mated with a TF39/CF6 engine core. The complete full-scale high-bypass fan engines will then be tested at the General Electric Remote Test Site at Peebles, Ohio, to determine their overall aero/acoustic performance as well as thrust and specific fuel consumption.

This report presents the aerodynamic component test results on Fan A with uniform inlet flow and with tip radial, crosswind, and circumferential distortion of the inlet flow. Details of the design of Fan A, and the other fans to be evaluated in this test series, are given in Reference 1. The aerodynamic component test results of Fan B are given in Reference 2.

## 3.0 DESCRIPTION OF TEST FAN

The aerodynamic design point for this low-speed fan was selected at the altitude cruise condition, a flight Mach number of 0.82 at an altitude of 35,000 feet (10.67 km). At this condition, the corrected tip speed is 1160 ft/sec (353.6 m/sec) with an average fan bypass total pressure ratio of 1.50 and an average fan core total pressure ratio of 1.32. The design corrected fan flow of 950 lb/sec (430.9 kg/sec), with a hub tip radius ratio of 0.465 and a specific flow of 41.3 lb/sec/ft$^2$ (197.0 kg/sec/m$^2$) of annulus area, results in a tip diameter of 73.354 inches (1.863 m). The design flow for the fan core, corrected to fan inlet, was 144.0 lb/sec (65.3 kg/sec) resulting in a bypass ratio of 5.60.

Figure 1 shows a meridional view of the Fan A component test vehicle. Immediately downstream of the rotor, a flow splitter is located which separates the fan bypass flow from the fan core flow. The axial distance between the rotor and bypass outlet guide vane (OGV), expressed in number of rotor chords, is a minimum of 2.0. The axial distance between the rotor and fan core OGV, expressed in number of rotor chords, is 1.25. No inlet guide vanes were incorporated in the configuration. The moderate-aspect-ratio (2.32) tip-shrouded rotor contained 40 blades. The rotor tip and hub solidities were 1.45 and 2.50, respectively. Ninety vanes were incorporated for both the outer and inner OGV's for a vane-number-to-blade-number ratio of 2.3.

The design rotor tip relative Mach number is 1.20. The rotor blade employs a profile shape that is specifically tailored to prevent excessive shock losses on the suction surface and still be compatible from a throat area and energy addition standpoint. The blade meanline shape and point of maximum thickness vary radially. The blade is similar to a double-circular arc profile in the hub region. Profile shapes at other radii are generally similar in appearance to the NASA multiple-circular arc profiles.

The profile shapes for the bypass and core OGV's, which operate at moderate conditions of inlet Mach number and diffusion factor, were designed with a modified NASA 65 series thickness distribution on a circular arc meanline.

Tabulated below are some of the pertinent Mach numbers and diffusion factors for the rotors and outlet guide vanes:

| | | | Outlet Guide Vanes | |
|---|---|---|---|---|
| | Rotor | | Bypass | Core |
| Inlet Mach Number | OD | 1.20 | 0.71 | 0.67 |
| | ID | 0.75 | 0.65 | 0.71 |
| Diffusion Factor | OD | 0.350 | 0.442 | 0.423 |
| | ID | 0.368 | 0.412 | 0.383 |

Complete design details are presented in Reference 1.

FOLDOUT FRAME 1

PRECEDING PAGE BLANK NOT FILMED

1 FOLDOUT FRAME 2

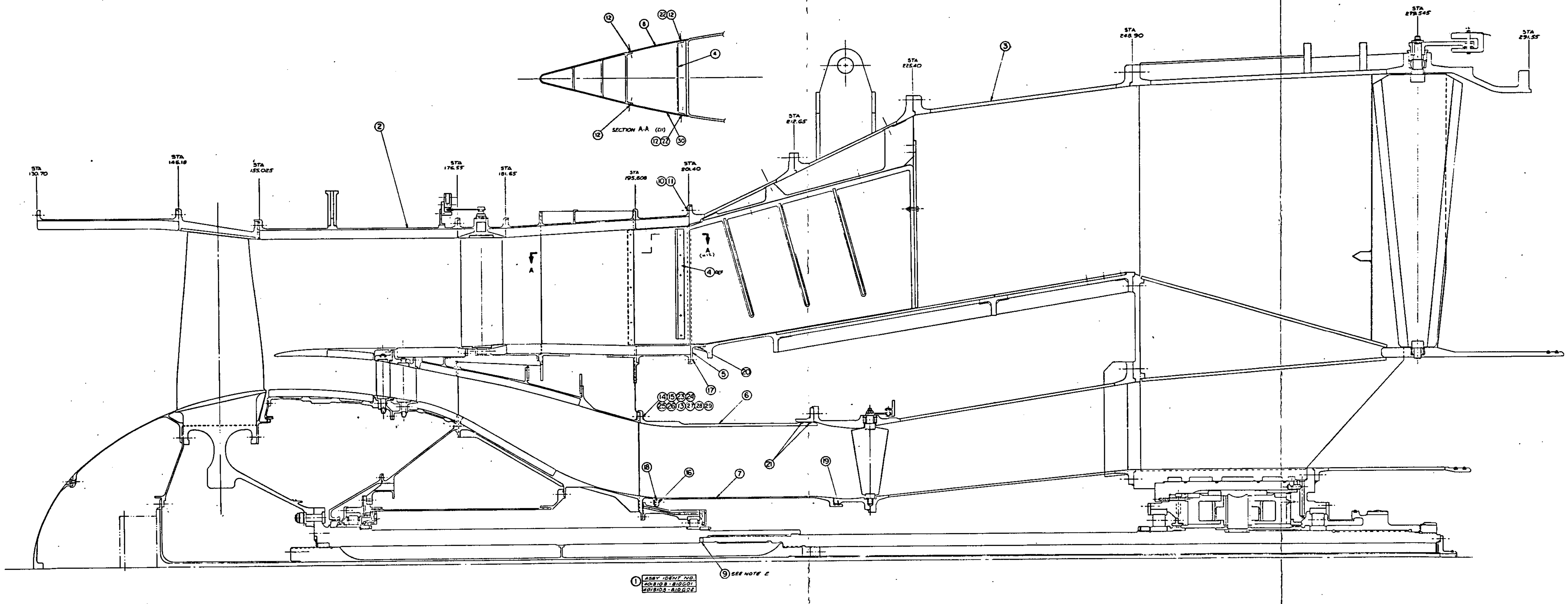

Figure 1. Fan A Component Test Vehicle Layout.

PRECEDING PAGE BLANK NOT FILMED

# 4.0 TEST SET-UP AND PROCEDURE

## 4.1 TEST FACILITY

Performance tests of fan A were made in General Electric's Large Fan Test Facility, at Lynn, Massachusetts. The general aspects of the test vehicle facility installation are shown in Figure 2. The test fan draws air vertically downward from the atmosphere through a throttling device which is located at the top of the inlet stack. Testing for this fan was performed with an open inlet throttle except for the high power extraction points where the facility power became limiting. The air then passes through a cascade of turning vanes and proceeds horizontally to a foreign object damage (FOD) protection screen and accelerates through an area ratio of 5.4 into the fan inlet. Downstream of the fan rotor, the flow is split into a fan bypass portion and a fan core portion. The bypass flow is ducted from the vehicle discharge through an adapter into the facility where the bypass discharge valve is located. This air is collected and exhausted vertically into the atmosphere. The fan core flow is ducted from the vehicle discharge through an adapter into the facility where the main discharge valve is located. This air is collected and passed through a pipe containing a flow measurement system and is finally discharged vertically into the atmosphere. Dial indicators are attached to each of the discharge valves to indicate the relative valve position, zero indicates fully closed and 100 indicates fully open.

Power to drive the test fan is provided by a steam-turbine rated at 30,000 horsepower (22.4 Mw).

## 4.2 OVERALL PERFORMANCE INSTRUMENTATION

Overall fan performance was determined from measurement of fan inlet and fan discharge total temperatures and total pressures. At fan inlet, the total pressure was measured by four six-element rakes located in the cylindrical section of the inlet duct between the bellmouth and the fan inlet. Twenty-four thermocouples attached to the inlet FOD screen were used for determination of inlet total temperatures. The pressure and temperature sensors were located approximately on centers of equal area. At fan discharge, the total temperature and total pressure were measured by circumferential arc rakes. Seven 12-element arc rakes were located behind the fan bypass OGV's and five seven-element arc rakes were located behind the fan core OGV's. The elements were circumferentially spaced so as to span two OGV passages. Radially, the arc rakes were located on centers of equal design mass flow of the fan bypass and fan core, respectively. A more detailed description of this and the other vehicle instrumentation is contained in Appendix I.

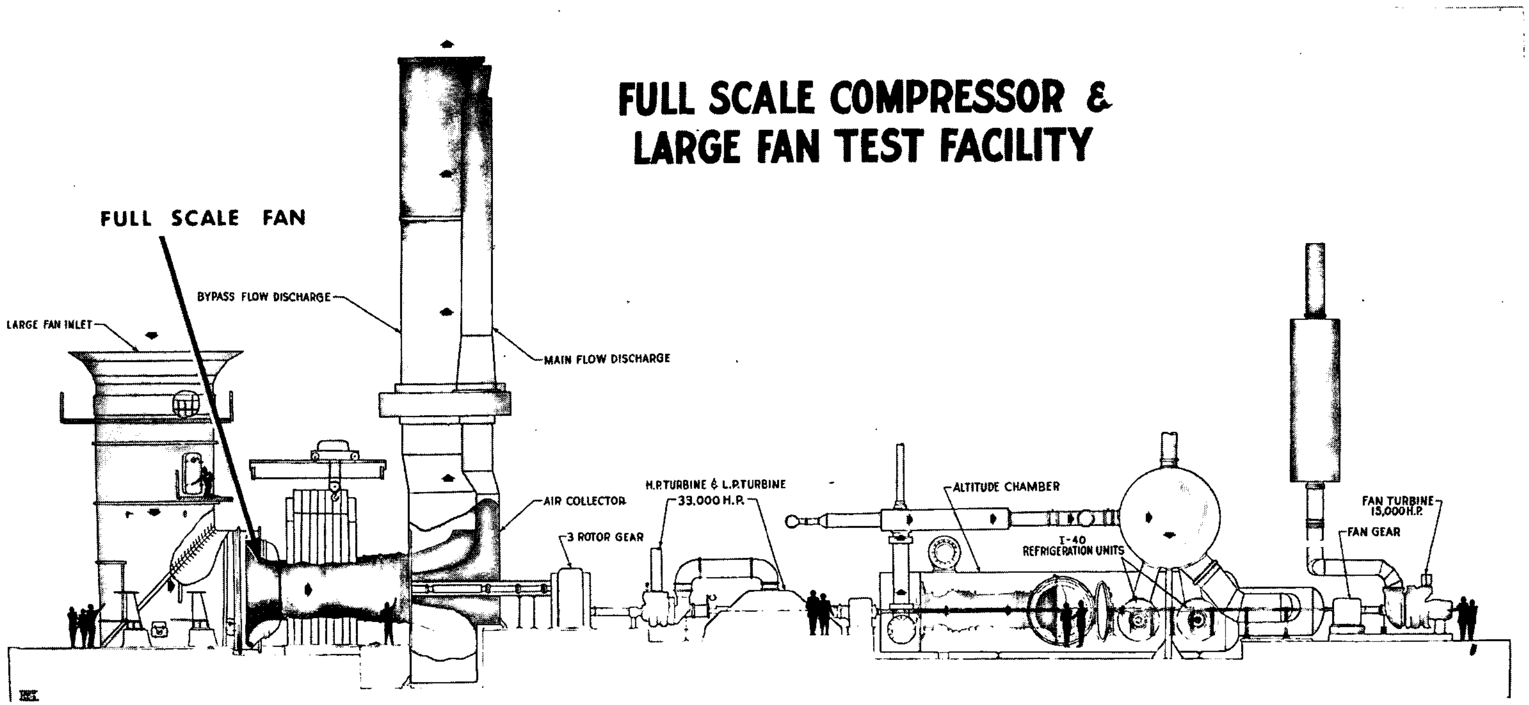

Reproduced from
best available copy.

Figure 2. Full-Scale Compressor and Fan Test Facility.

## 4.3 BYPASS RATIO SCHEDULE

The configuration of the Fan A test vehicle was designed to simulate the fan bypass and fan core flows through the fan frame region with independently controllable discharge valves for each portion. Cycle calculations for the Fan A engine system yielded a bypass ratio migration, as a function of fan speed, along a typical operating line. The procedure adopted for testing the Fan A vehicle was to set this bypass ratio, as a function of fan speed, for all operating points on a given speed line except those specific points aimed at determining the effects of bypass ratio swing on fan operation. The approximate total fan flow and fan core flow were calculated in real time by an analog computer and continuously displayed in the Data Recording Center. These data were used as a guide in setting the bypass and core discharge valves to maintain the desired bypass ratio. Generally, the detailed reduced data showed that the bypass ratios for the test points were within 0.2 count of the desired values as is shown in Figure 3.

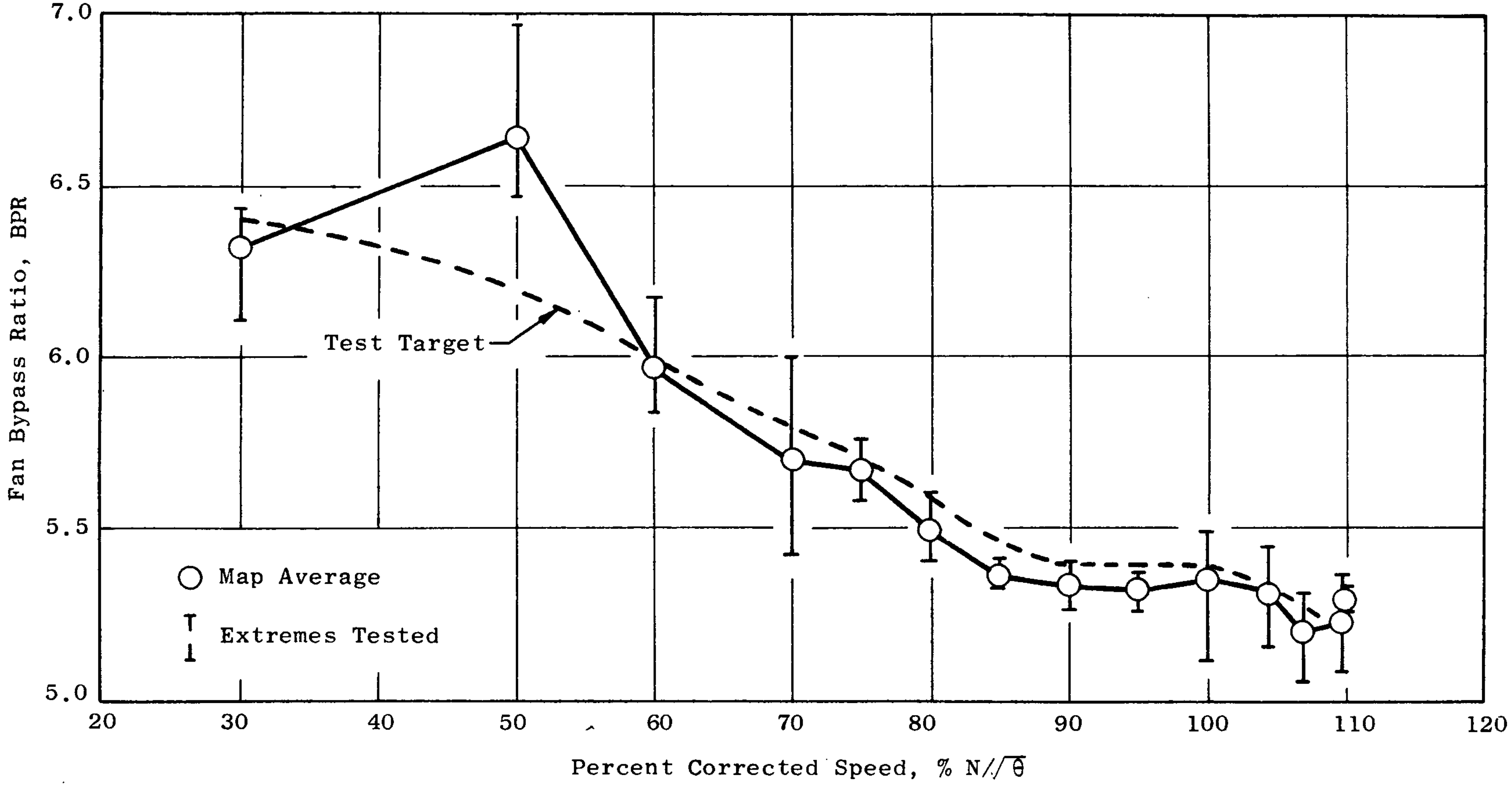

Figure 3. Clean Inlet Flow Test Bypass Ratio Schedule.

# 5.0 RESULTS AND DISCUSSION

## 5.1 PRESENTATION OF OVERALL RESULTS

The basic design of Fan A incorporates radial variations in discharge total pressure and total temperature. Additionally, deviations from design intent and the migration of the fan to other operating conditions will produce differing radial variations. Accurate cycle representation of the fan component requires recognition of these variations. Accordingly, the overall fan performance is presented in the form of two maps to distinguish the performance characteristics in the fan bypass and fan core regions. One map presents fan bypass total pressure ratio and efficiency versus total fan flow. The second map presents fan core total pressure ratio and efficiency versus fan core flow. Using total fan flow, rather than bypass flow, on the bypass map is somewhat arbitrary but does serve the purpose of providing an overall maximum flow constraint, at a given speed, when these maps are incorporated into the cycle performance calculations.

Presentation of the fan performance by two separate maps tends to imply that the results are independent, as would be the case if the splitter between the bypass flow and fan core flow extended forward through the rotor. This is not the case for the configuration employed by Fan A; a definite performance interdependence exists between the two streams. Although it is an oversimplification, it is meaningful to consider the case where the leading edge of the flow splitter is located aft of a single OGV which spans the entire annulus. In such a case, the OGV discharge pressure is largely controlled by the bypass discharge valve by virtue of the high bypass ratio for the fan. At fixed bypass discharge valve settings, a change to the fan core discharge valve will directly affect its flow rate but not significantly affect the delivery pressure of the fan core flow. Also, at fixed fan core discharge valve settings, a change to the bypass discharge valve will affect the delivery pressure into the fan core duct and thereby also affects its flow rate. The actual configuration with the splitter behind the rotor is more complex than either of the two extremes because of the influence of the splitter on the operation of the core region and the off-incidence and loading conditions forced onto the OGV's. Accordingly, for each value of bypass ratio, a separate and distinct pair of performance maps will result. A series of test points were recorded to investigate the effects of off-design bypass ratio operation; the results are presented in a later section.

## 5.2 UNDISTORTED FLOW PERFORMANCE

### 5.2.1 Fan Bypass Region

Measured performance of the Fan A stage is shown in Figures 4 and 5. The measured flow at the design bypass pressure ratio of 1.50 was 973 lb/sec (444.3 kg/sec) which is 2.42% greater than the design value of 950 lb/sec (430.9 kg/sec). The bypass adiabatic efficiency was 88.5%, 2.0 points above the objective value. A more meaningful way to compare the measured performance relative to design is at the intersection of a constant throttle

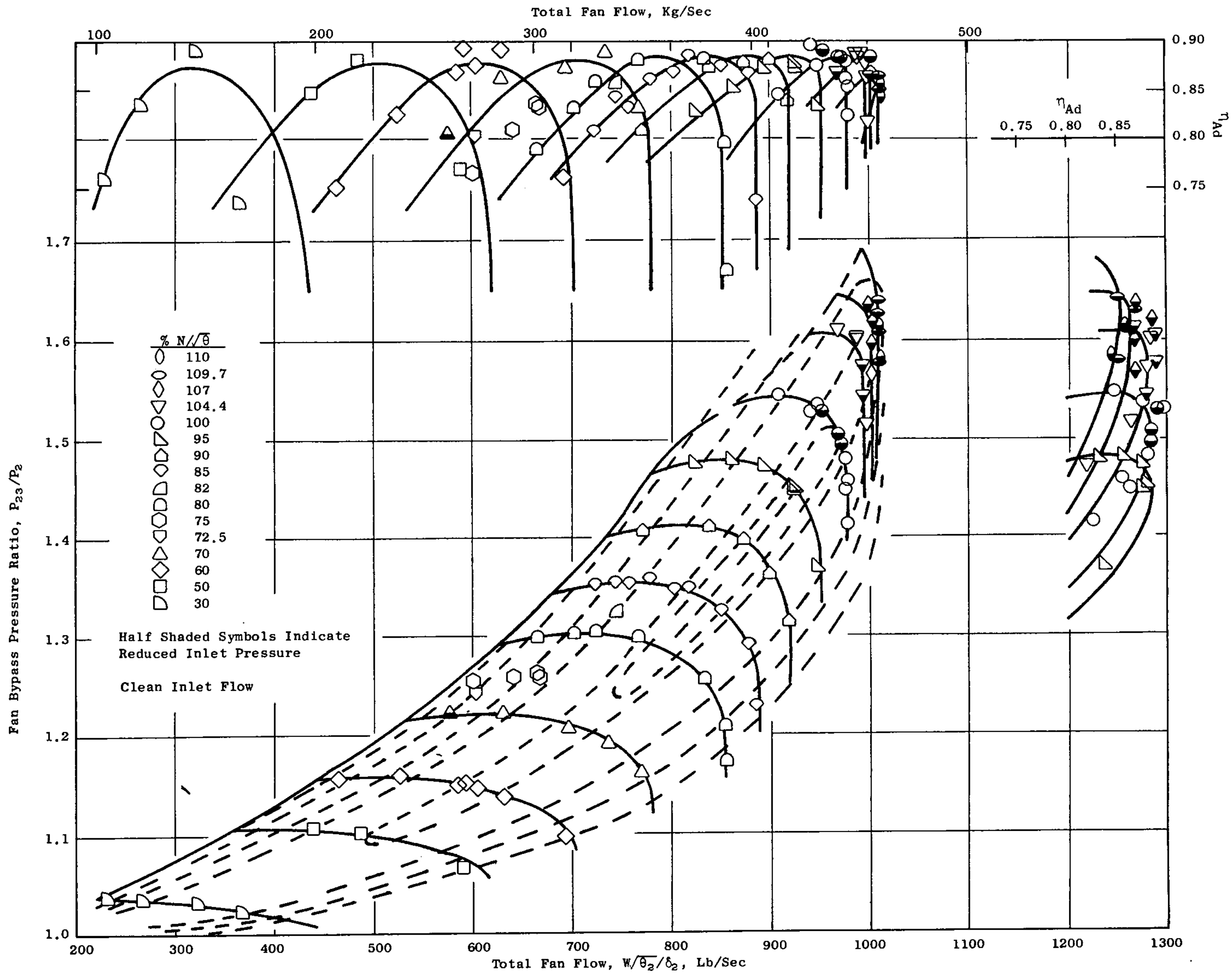

Figure 4. Fan A Performance Characteristics in the Bypass Region.

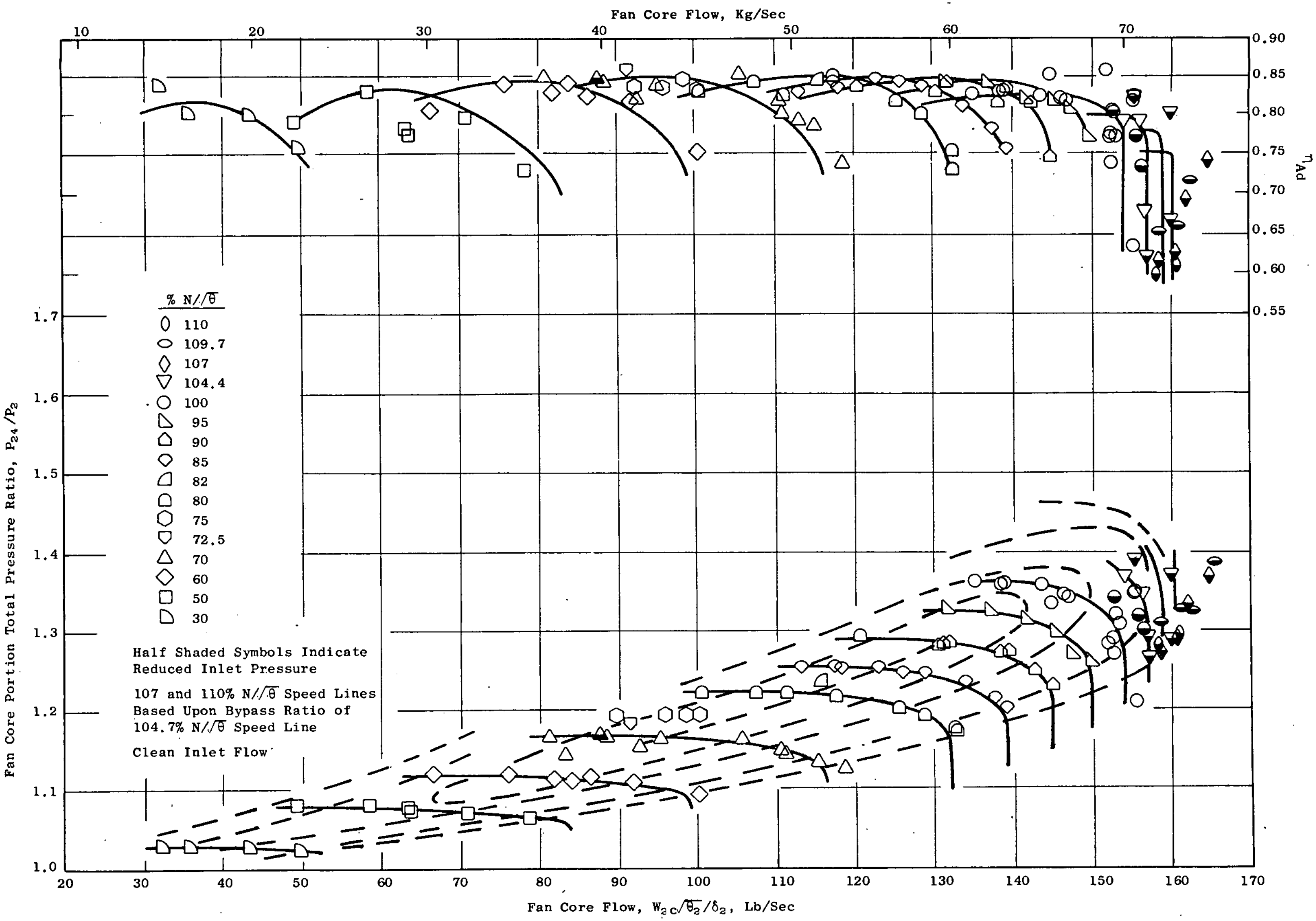

Figure 5. Fan A Performance Characteristics in the Core Region.

area line passing through the design point and the 100% corrected speed line. This method is significant since it reflects the manner in which the fan would operate in an engine system. At this point, the measured flow was 962 lb/sec (436.4 kg/sec) at a pressure ratio of 1.52. The bypass adiabatic efficiency was 88.3%. The peak efficiency at design speed was 88.5% at a bypass pressure ratio of 1.505 and a total fan flow of 970 lb/sec (440.0 kg/sec). At 110% corrected speed, a flow of 1010 lb/sec (458.1 kg/sec) was achieved, a specific flow of 43.9 $lb/sec/ft^2$ (209.4 $kg/sec/m^2$) of annulus area.

The operational limit line was determined up to, and including, 100% corrected speed. The operational limit was determined to be rotating stall at all corrected speeds except 100% where high bypass OGV stress precluded further increases in back pressure. The operating margin* achieved at 100% corrected speed relative to an operating line through the altitude cruise design point was 12.4%. However, posttest optimization of the fan operating line for minimum cruise specific fuel consumption required a 5.3% opening of the fan bypass nozzle area. With this area, the engine operating margin for 100% corrected speed at altitude is 17.2%. At 90% corrected speed, the operating margin was 10.8% relative to the design operating line, but it is 16.0% with the engine nozzle at sea-level-static conditions.

### 5.2.2 Fan Core Performance

The fan was designed to deliver a core pressure ratio of 1.32 at a core flow of 144.0 lb/sec (65.3 kg/sec). The proper selection of the map point for comparison with the design objectives is less obvious for the fan core performance than for the bypass performance since the match point for the core is not necessarily along a constant throttle area line but, instead, depends upon the overall engine operating characteristics. Selecting the objective core flow at 100% corrected speed, a core pressure ratio of 1.356 was achieved. At this condition, the core adiabatic efficiency was 83.3%. A peak adiabatic efficiency of 85.0% was achieved in the 70 to 90% corrected speed range.

The terminations of the constant speed lines on the low flow side were arbitrarily made consistent with the average bypass ratio from Figure 3 and the total fan flow limit from the bypass map. These terminations do not represent an operating limit of the fan core portion map. Furthermore, since it was the intent to maintain a constant bypass ratio

---

*Operating margin $= \left[ \dfrac{\dfrac{W}{P_{23}} \text{ at operating line}}{\dfrac{W}{P_{23}} \text{ at stall}} - 1 \right]$ x 100; % at constant speed at each speed, a vertical region in the bypass speed line results in a vertical region in the fan core speed line. A vertical fan core speed line generated in this manner does not necessarily imply a choked condition in the core stream. The apparant data scatter at high corrected speeds is a result of deviations from the nominal bypass ratio schedule (a bypass ratio excursion of 0.1 from nominal is equivalent to 2.8 lb/sec [1.3 kg/sec] in core flow at a total fan flow of 1000 lb/sec [453.6 kg/sec]).

The measured fan core efficiency was below design objectives. For high-bypass-ratio fans in general, a significant portion of the fan core flow is what would normally be classified as the "end wall" flow from the fan blade. For the Fan A configuration, the height of fan core duct expressed as a ratio to the staggered spacing of the fan blade, a significant dimension when analyzing end wall flows, is 1.32. Figure 6 shows the radial efficiency profile at stage discharge as deduced from the discharge arc rake instrumentation. Shown on this figure is an assumed efficiency profile for a redesigned configuration without a splitter. Also shown are the locations of seven arc rakes used for the efficiency evaluation of this hypothetical fan. It is observed that the actual instrumentation density in the fan core tends to emphasize the low efficiency end wall flow relative to measurements of the more conventional hypothetical fan.

As a part of the data analysis performed on Fan A, the efficiency, total pressure and temperature, OGV total-pressure-loss, and static-pressure-rise coefficients were computed for each arc rake immersion as described in Appendix II. Radial plots of this information for three points at 100% corrected speed are shown in Figures 7 through 9. Referring to Figure 7, a point near the nominal operating line, the bypass stage efficiency is lower in the end wall region but higher in the free stream region than design. This is consistent with the General Electric design policy which does not design for the entire velocity drop-off which occurs deep within the end wall region but instead tends to distribute these losses across the span. The bypass OGV total-pressure-loss coefficient, related to the difference between rotor and stage efficiency, is relatively consistent with design except at the vane ends. It is believed that the larger than design losses at the outside diameter and inside diameter of the OGV is caused by the relatively thick boundary layer entering the vane row as a result of the larger than normal axial spacing between the rotor and OGV (approximately 16 inches [0.41 m]). In the fan core region, the rotor exit total temperature profile shows that the design work input was nearly achieved. However, the total pressure profile tails off relative to design intent showing that the work input was not accomplished efficiently, as is also shown by the efficiency profile. The core OGV total-pressure-loss coefficients are high in the vane end regions. Boundary layer growth along the wall in the 9-inch (0.29-m) axial spacing between the rotor and OGV is a contributing factor. Also, as previously discussed, the instrumentation density tends to emphasize the low-energy end wall flow.

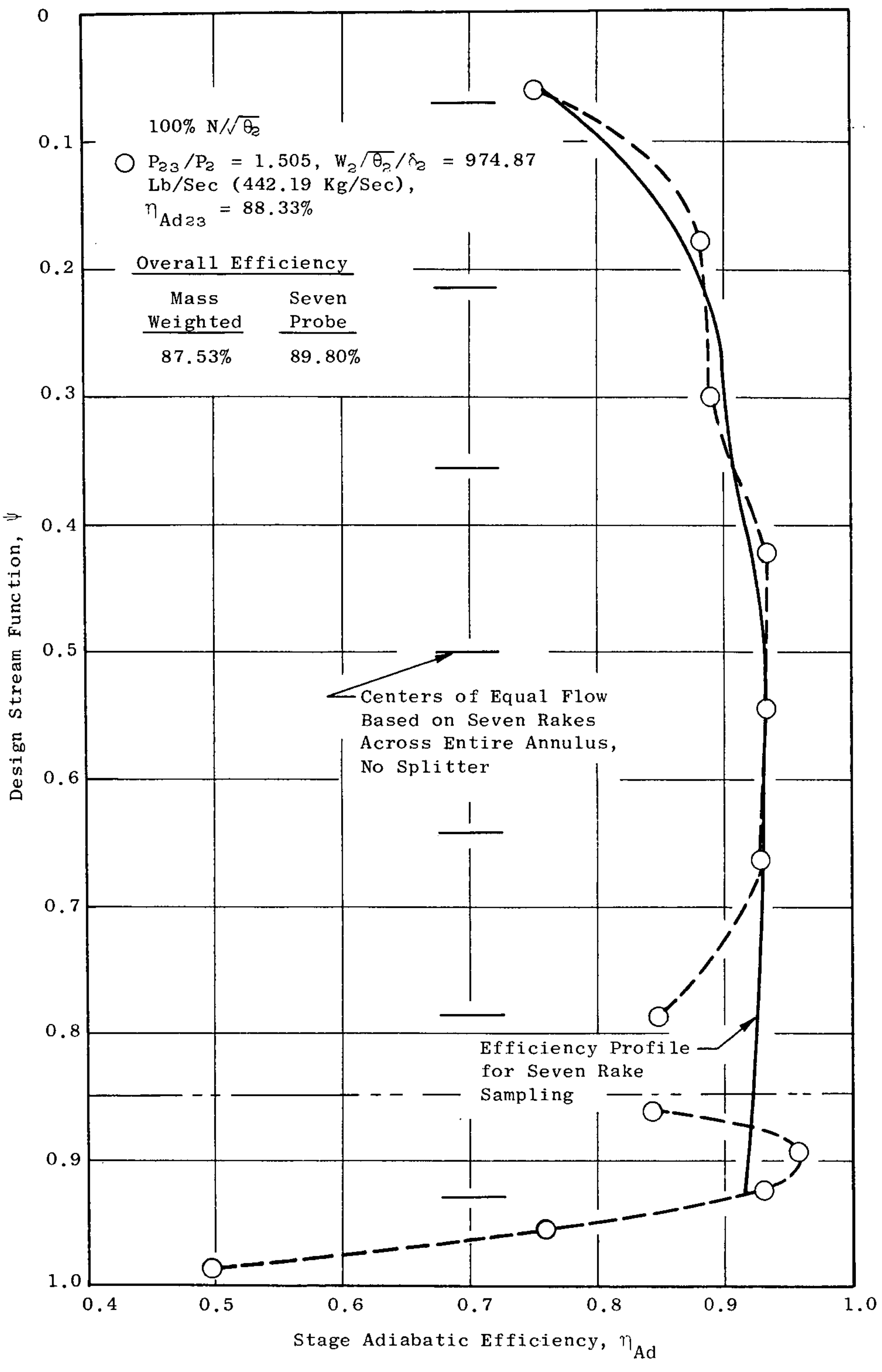

Figure 6. Radial Efficiency Profile at Discharge.

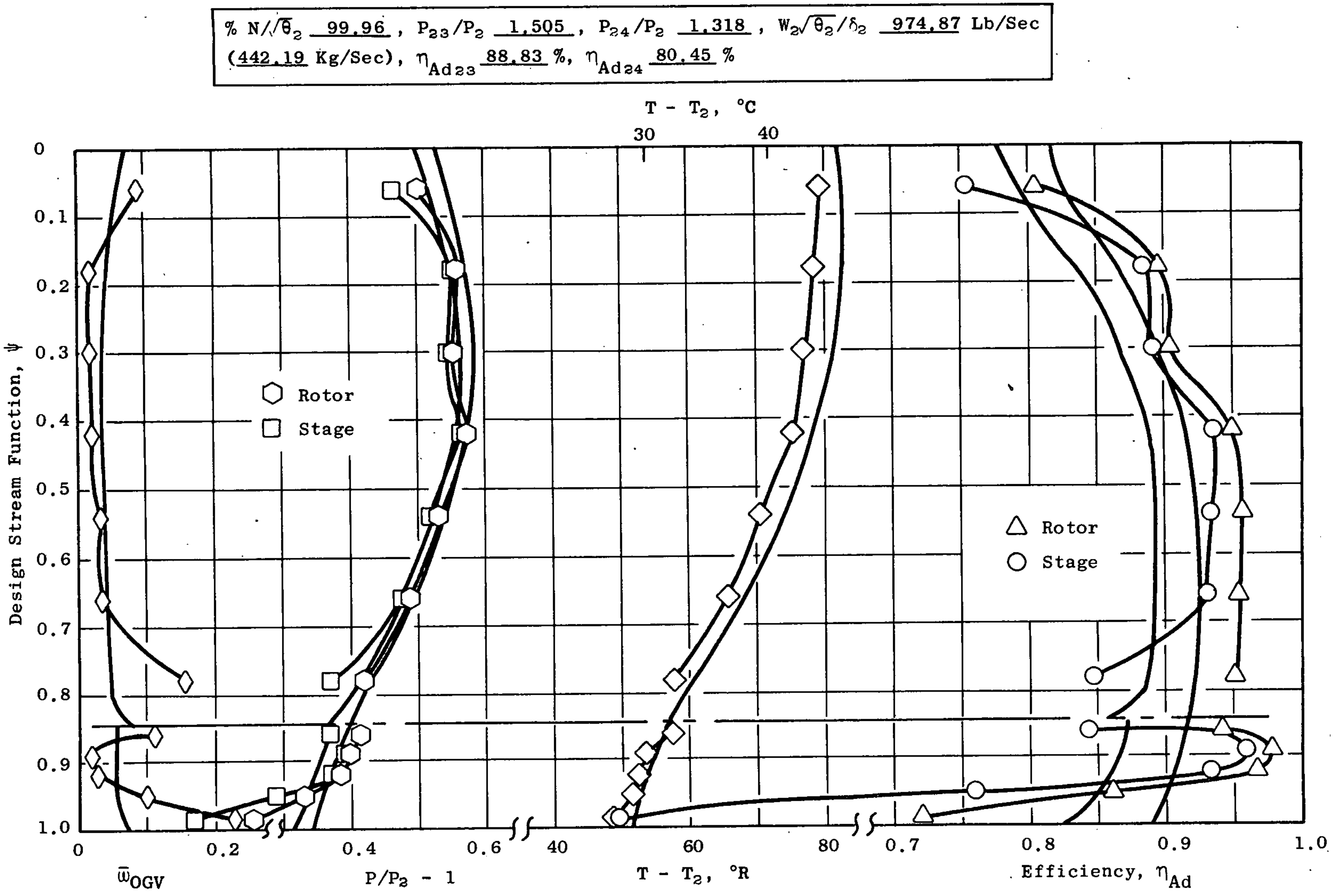

Figure 7. Radial Profiles.

$\% \ N/\sqrt{\theta_2}$ 99.96, $P_{23}/P_2$ 1.534, $P_{24}/P_2$ 1.339, $W_2\sqrt{\theta_2}/\delta_2$ 949.69 Lb/Sec (430.77 Kg/Sec), $\eta_{Ad_{23}}$ 87.62 %, $\eta_{Ad_{24}}$ 81.98 %

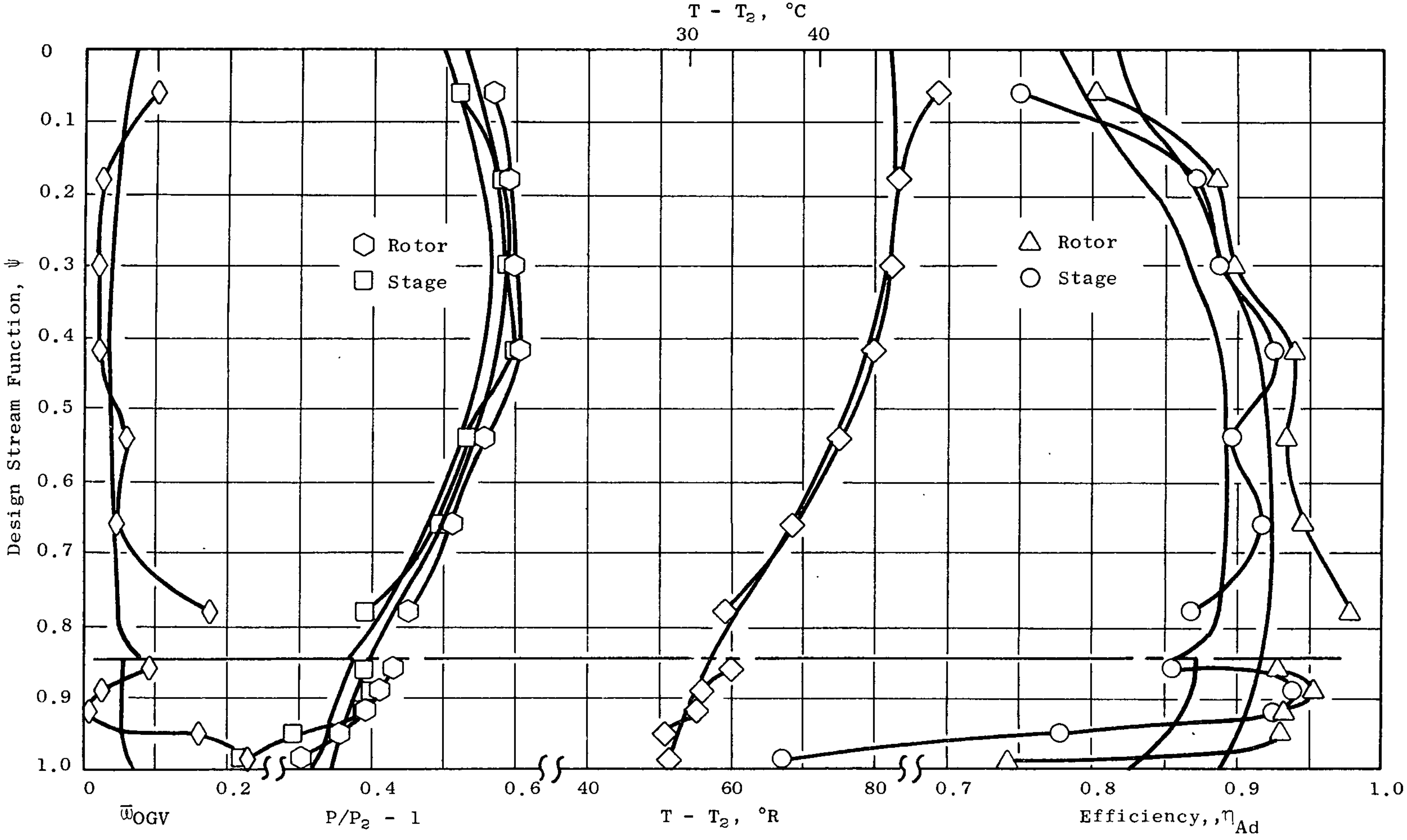

Figure 8. Radial Profiles.

$\% N/\sqrt{\theta_2}$ 99.49, $P_{23}/P_2$ 1.447, $P_{24}/P_2$ 1.288, $W_2\sqrt{\theta_2}/\delta_2$ 978.06 Lb/Sec (443.64 Kg/Sec), $\eta_{Ad_{23}}$ 86.33 %, $\eta_{Ad_{24}}$ 77.18%

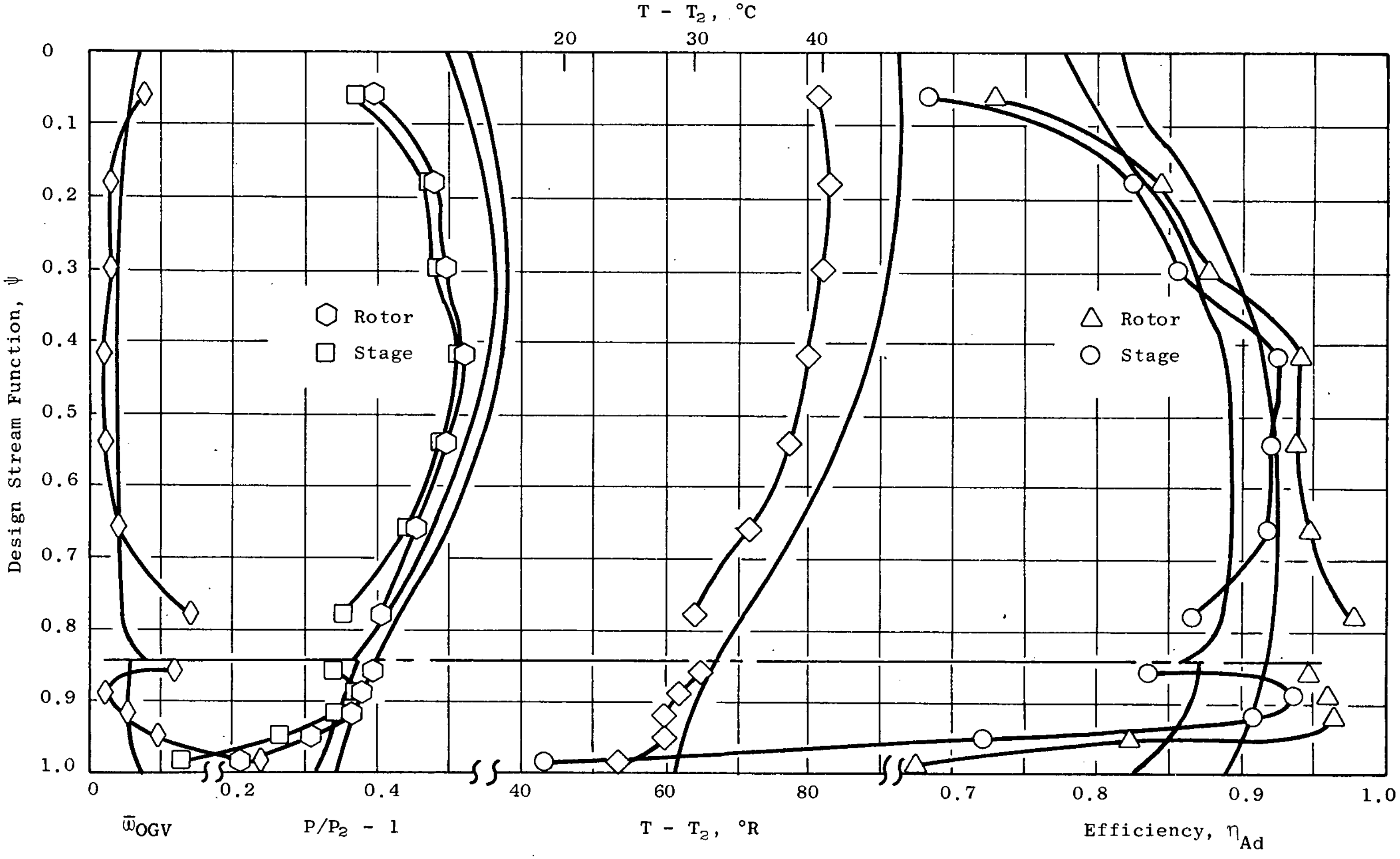

Figure 9. Radial Profiles.

The rotor and stage efficiency, OGV total-pressure-loss and static-pressure-rise coefficients are plotted against ideal throttle area for immersions 1, 3, 5, and 7 (which correspond to stream functions of 0.06, 0.30, 0.54, and 0.78, respectively) in the fan bypass and for each of the five immersions in the fan core (which correspond to stream functions of 0.86, 0.89, 0.92, 0.95, and 0.98) in Figures 10 through 18. The bypass throttle area on these figures is the nozzle throat area required to pass the bypass flow, assuming an isentropic expansion from measured discharge total pressure and total temperature to ambient static pressure. For the bypass, the peak rotor efficiency and minimum OGV total-pressure-loss coefficient for each immersion occurs in the near vicinity of the design throttle area indicating that this portion of the fan is well matched radially. The outer three immersions of the fan core behave similarly. The inner two immersions of the fan core show a large improvement in rotor efficiency with throttling, the peak efficiency being observed at or near the most highly throttled point. The OGV total-pressure-loss coefficient for these immersions shows only modest changes with throttling.

### 5.2.3 Bypass Ratio Excursion

Tolerance of the fan to off-design bypass ratio operation was systematically investigated as a part of the test investigation on Fan A. A fan corrected speed of 90% was selected as representative, and for each of three bypass discharge valve settings, readings were taken for five fan core portion discharge valve settings. The overall performance maps are shown in Figures 19 and 20. Superimposed on these performance maps are lines of constant bypass ratio. Peak efficiency is observed to occur near the design bypass ratio of 5.6 for both portions. For increased bypass ratios, Figure 20 shows that the core portion suffers large efficiency losses while the bypass portion (Figure 19) has only moderate losses. This resulted because, to simulate engine operation, the core discharge valve variation employed was much greater than that of the bypass discharge valve. At the highest bypass ratios, the core portion incidence angles and diffusion factors were significantly greater than their design values, particularly for the outlet guide vanes, and the splitter was subjected to a high enough incidence to cause high losses on its upper surface, implying flow separation there.

To aid in the understanding of these effects, stage and rotor efficiencies and OGV total-pressure-loss and static-pressure-rise coefficients were computed as described in Appendix II for each arc rake immersion at a bypass discharge valve setting 37.0, which is near the nominal operating line, of the bypass ratio investigation. The results of these computations are shown in Figures 21 through 29. The immersion for each of the figures is identified in terms of its design stream function, 0 being the OD, 0.84 being the splitter, and 1.0 being the ID. Referring to Figures 21 through 24, which correspond to the bypass flow, only very modest changes to stage and rotor efficiency and OGV total-pressure-loss and static-pressure-rise coefficients are observed. This indicates that the bypass configuration is tolerant to bypass ratio migrations, at least over the range tested, and that no significant flow breakdown occurs. (An exception to this is the drop in rotor and stage efficiency observed on the bypass ID immersion, Figure 24, for the highest

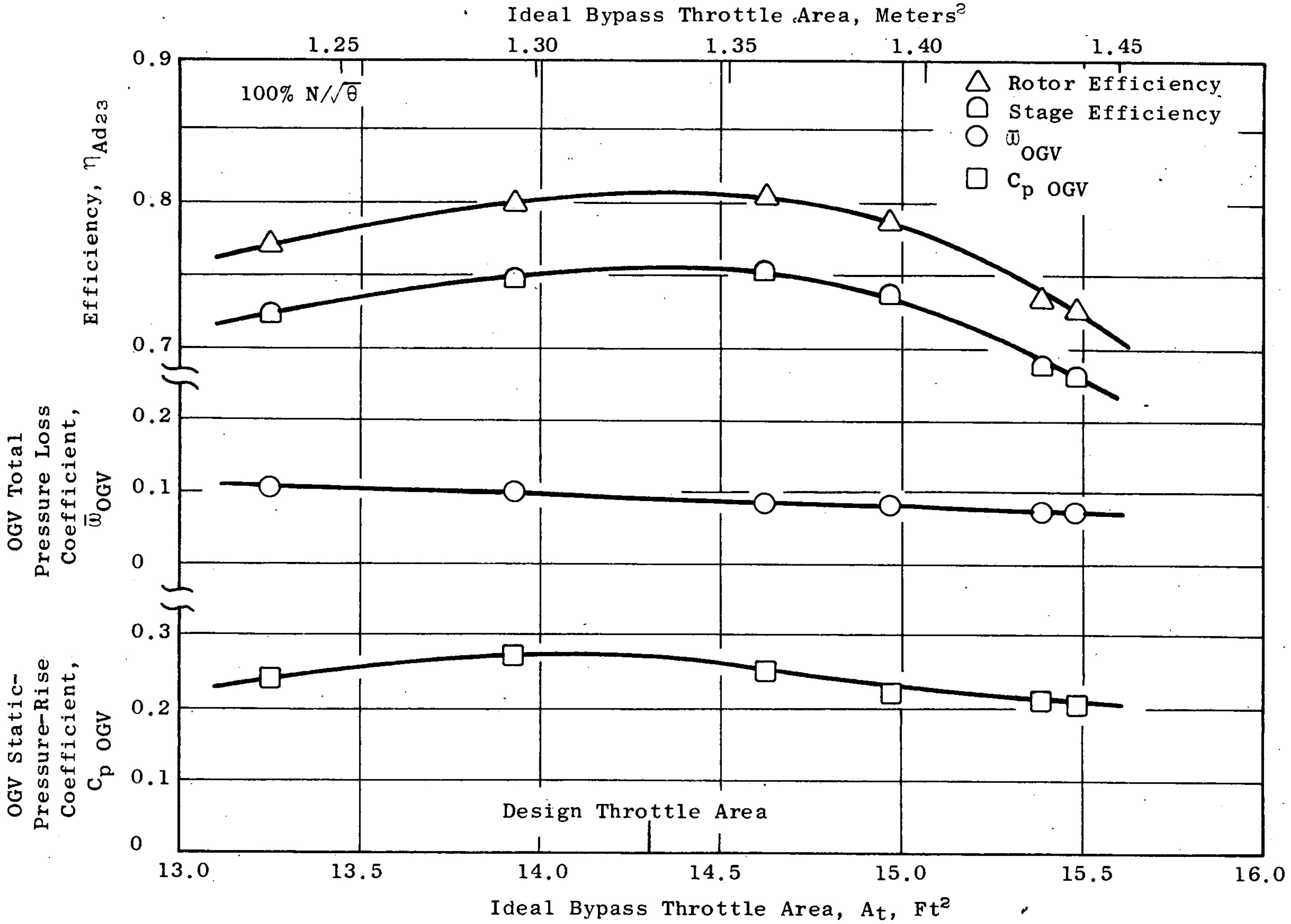

Figure 10. Variation of Element Properties with Throttling, Design Stream Function = 0.0606. (Bypass OD).

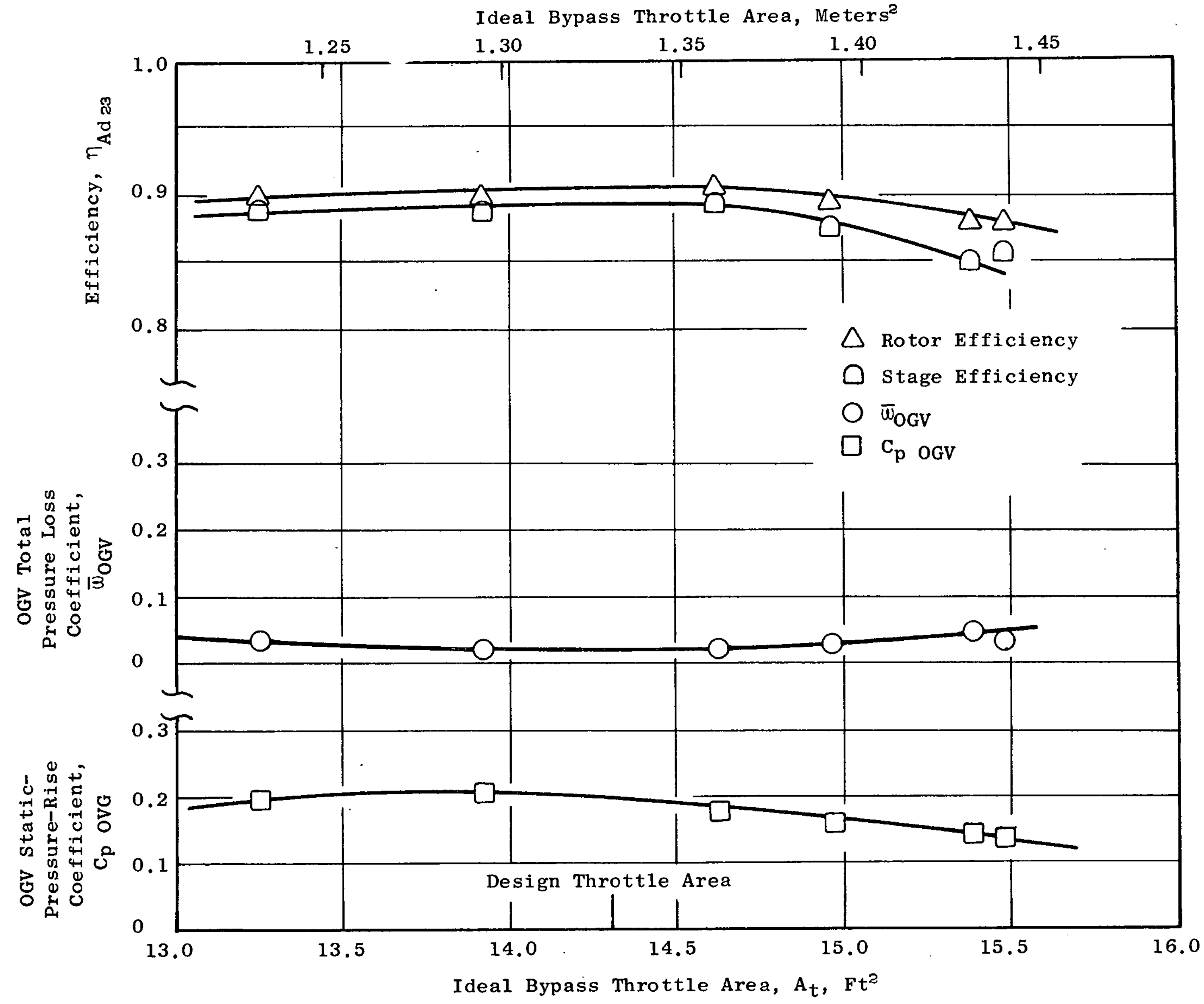

Figure 11. Variation of Element Properties with Throttling, Design Stream Function = 0.303.

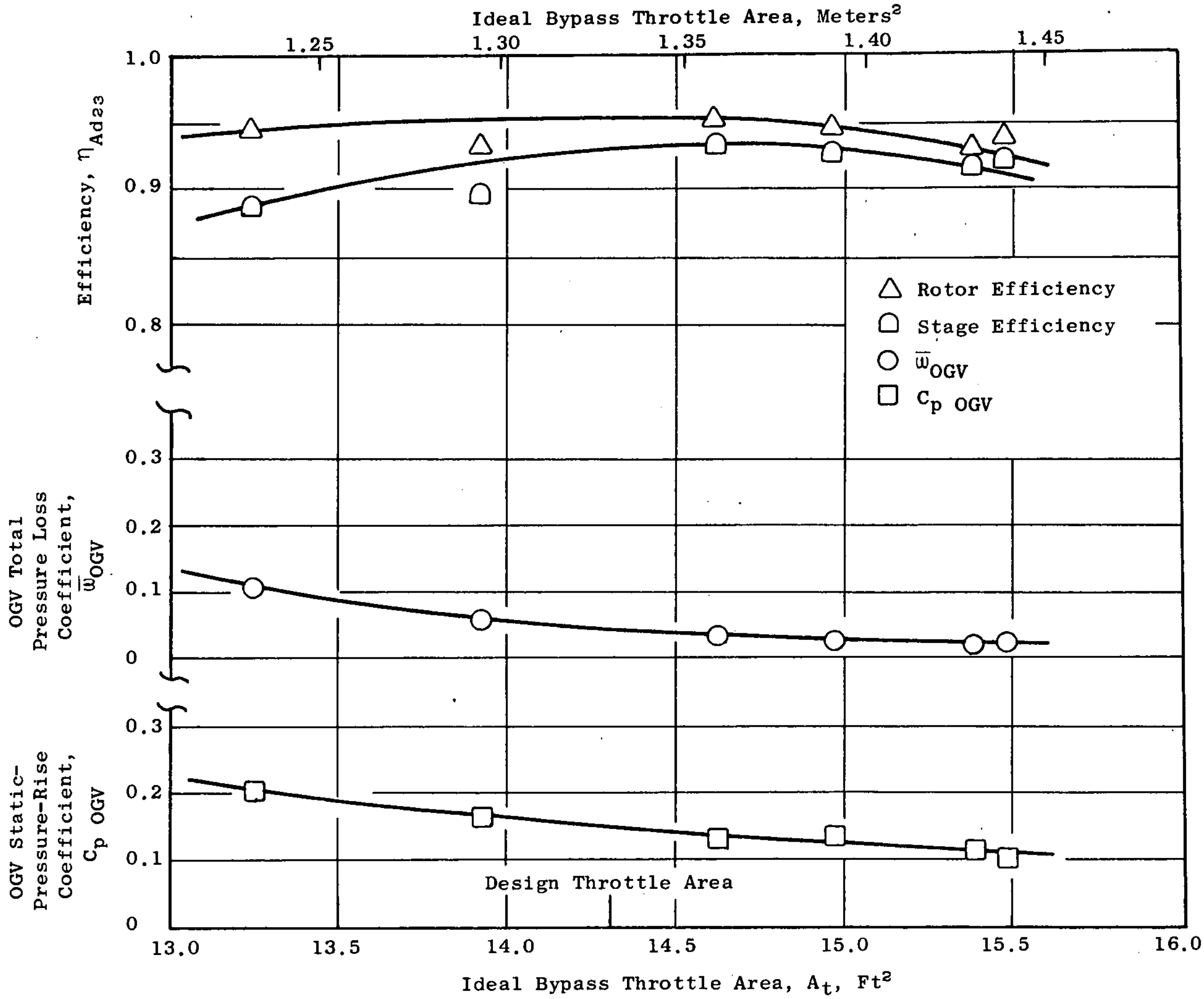

Figure 12. Variation of Element Properties with Throttling, Design Stream Function = 0.5454.

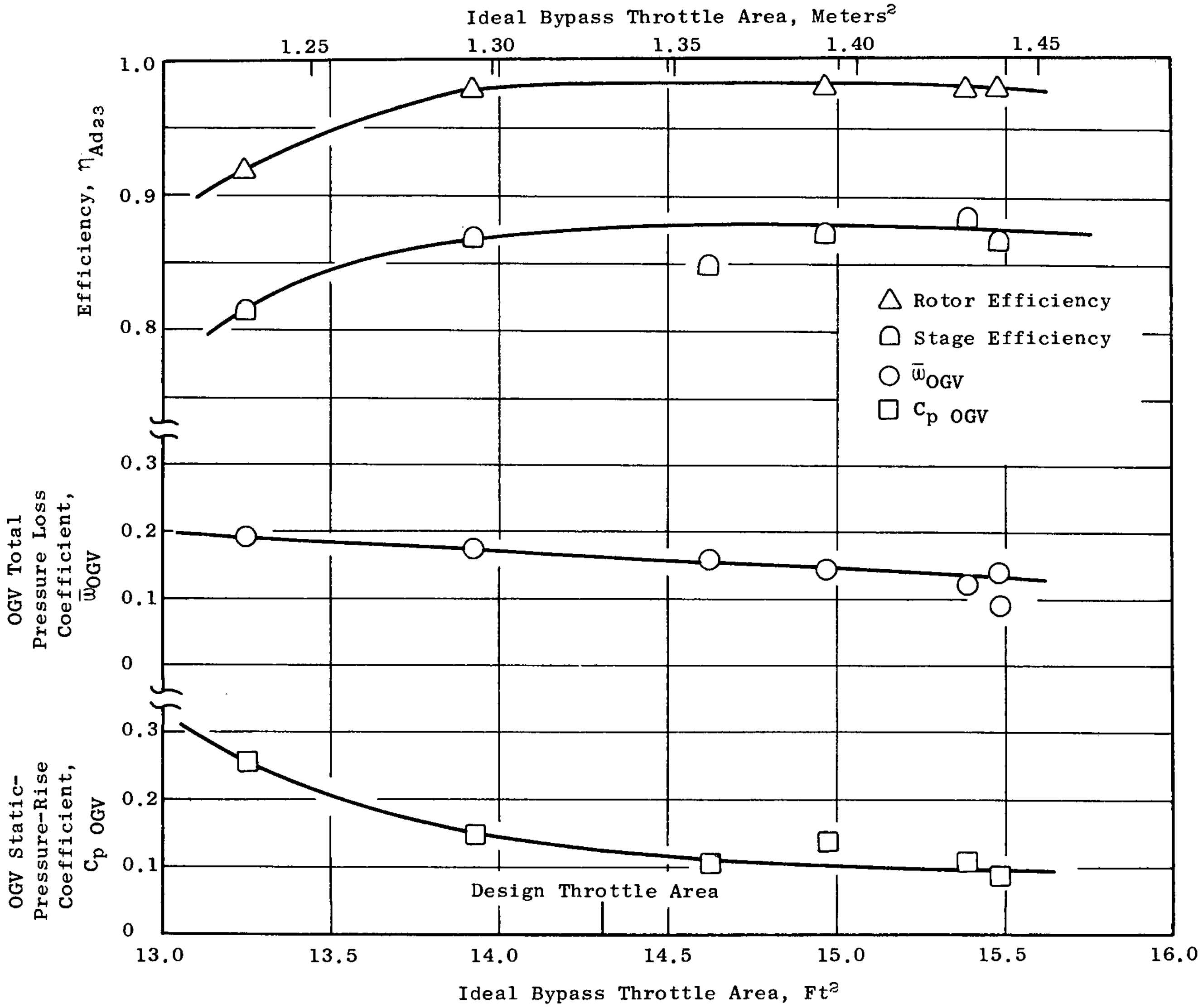

Figure 13. Variation of Element Properties with Throttling, Design Stream Function = 0.7878 (Bypass ID).

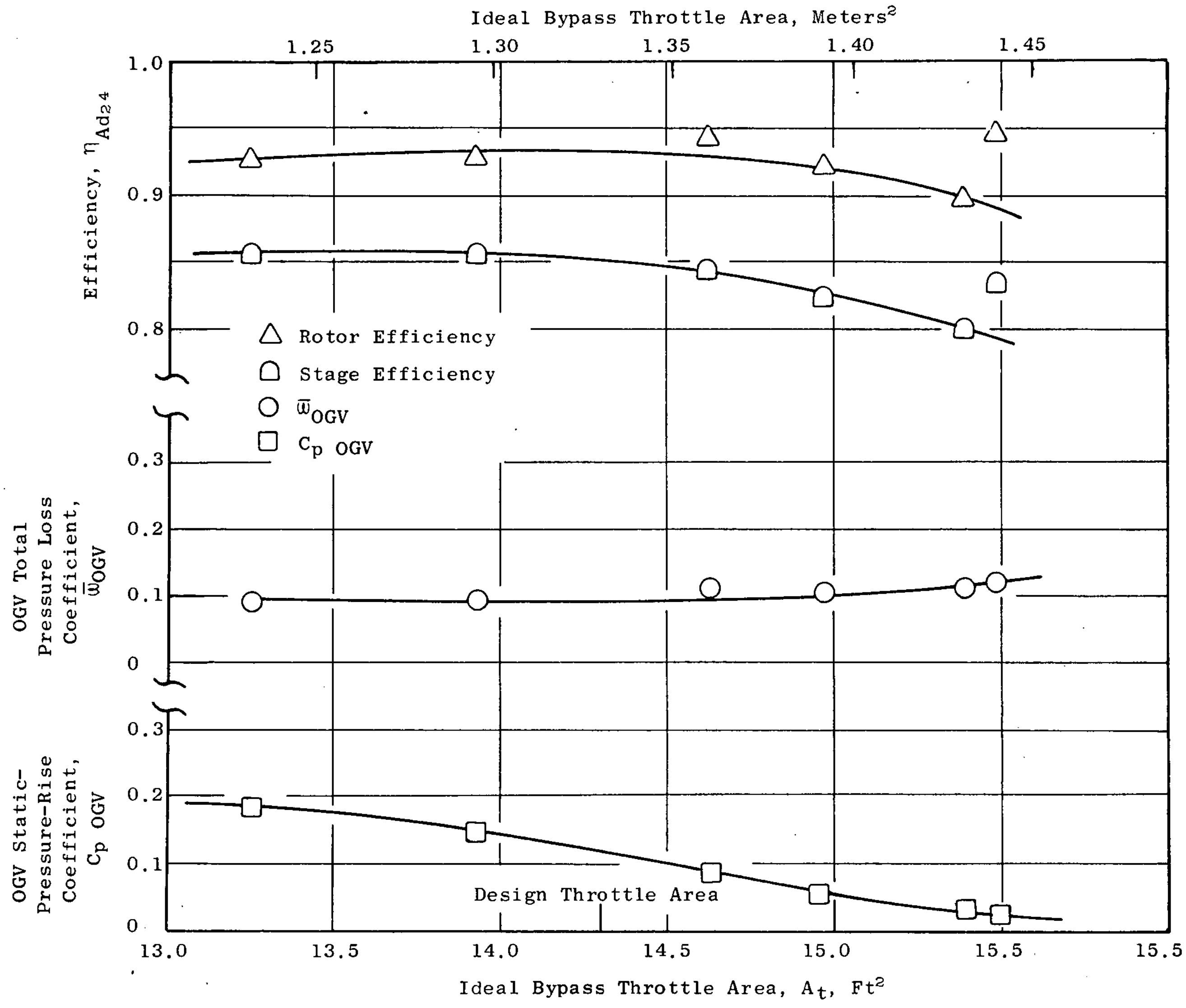

Figure 14. Variation of Element Properties with Throttling, Design Stream Function = 0.8637 (Core OD).

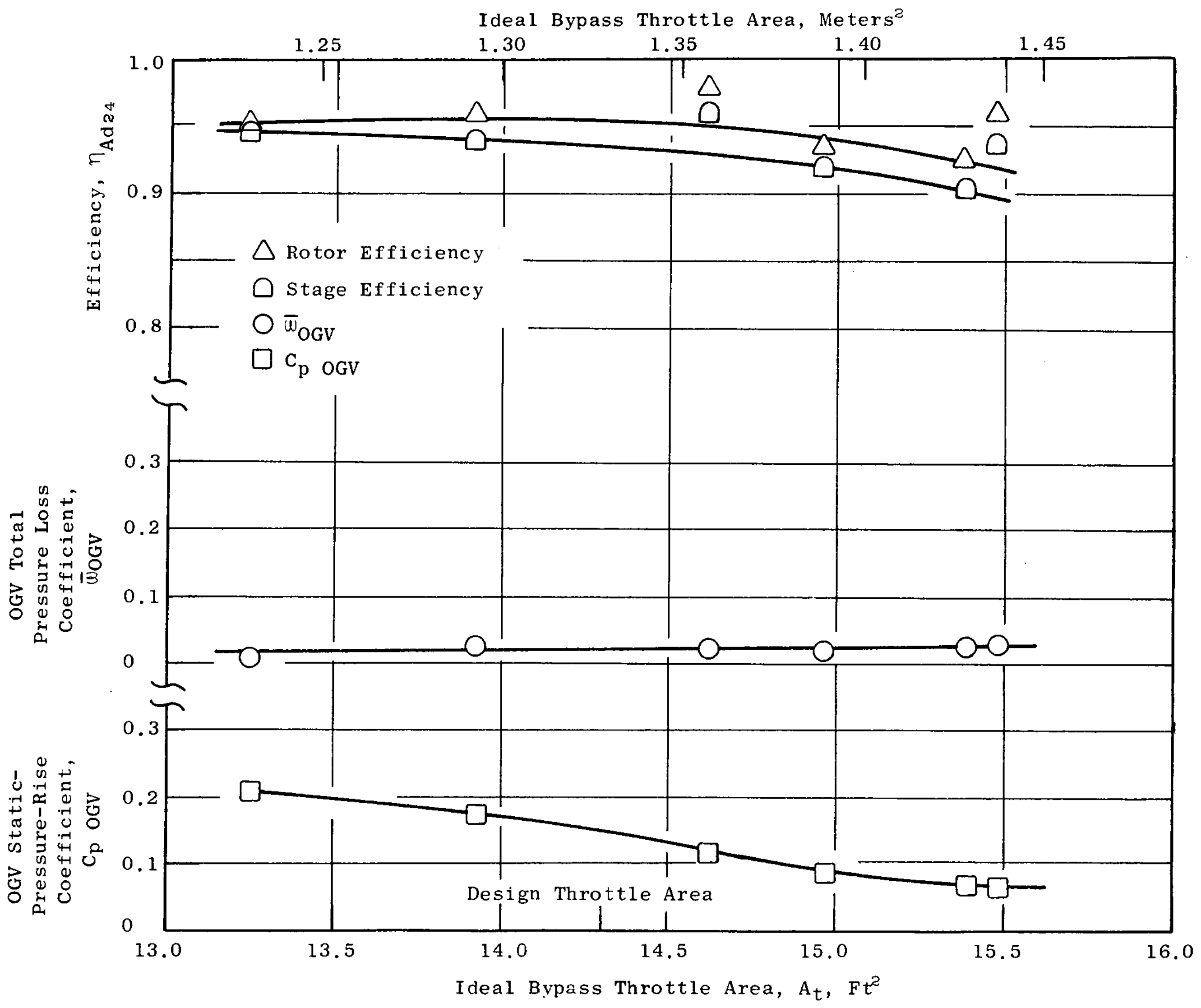

Figure 15. Variation of Element Properties with Throttling, Design Stream Function = 0.8947.

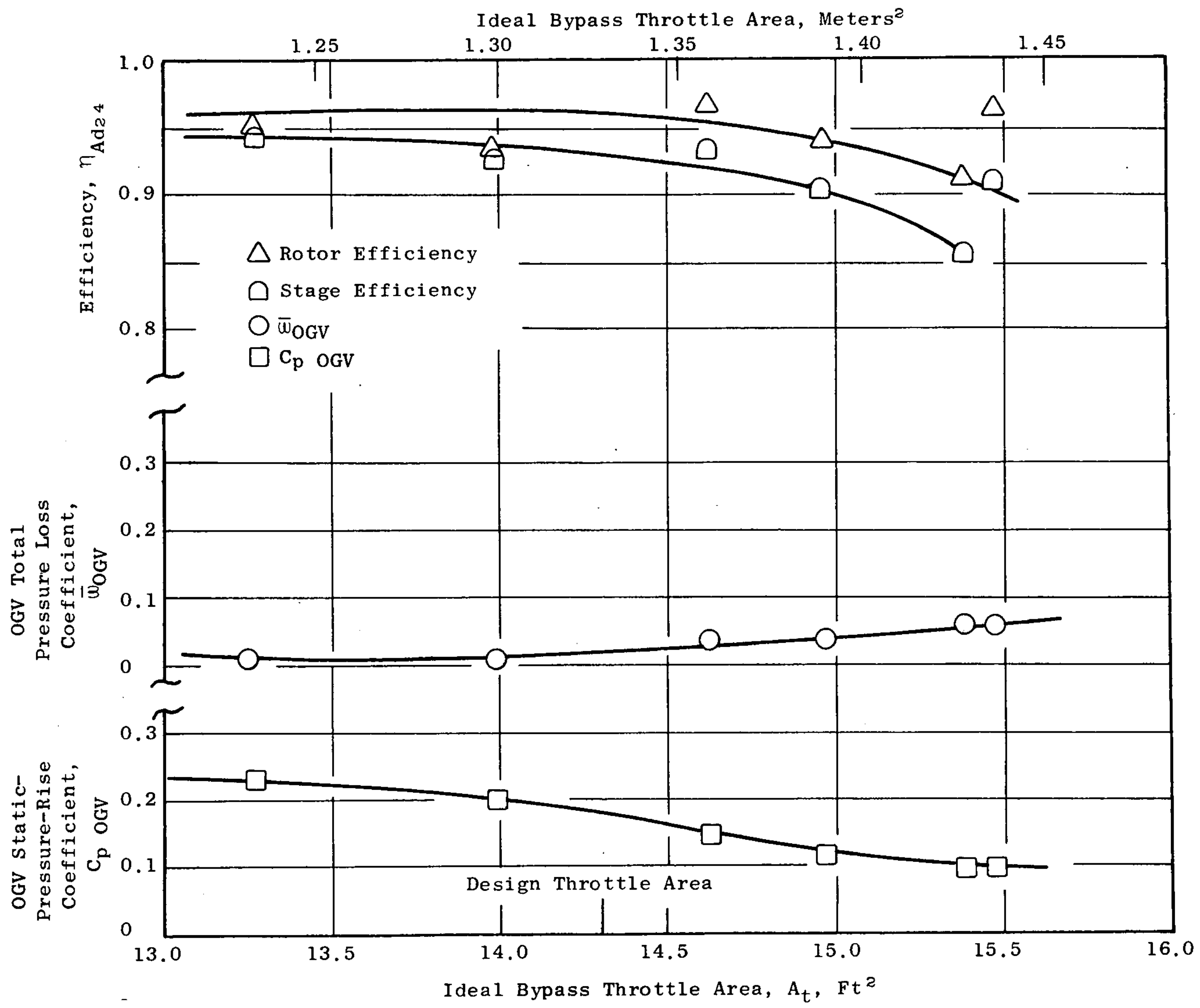

Figure 16. Variation of Element Properties with Throttling, Design Stream Function = 0.92.

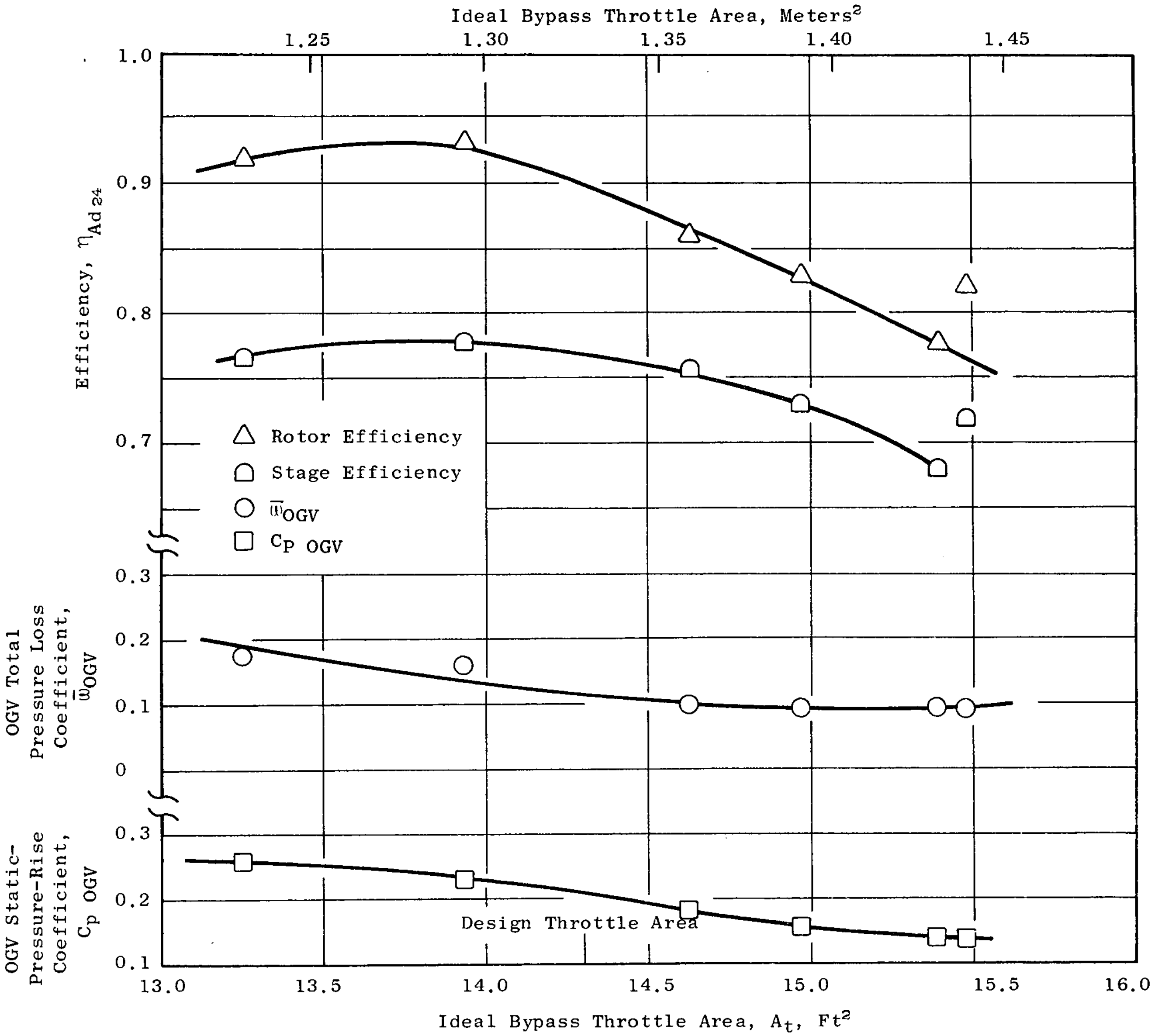

Figure 17. Variation of Element Properties with Throttling, Design Stream Function = 0.9546.

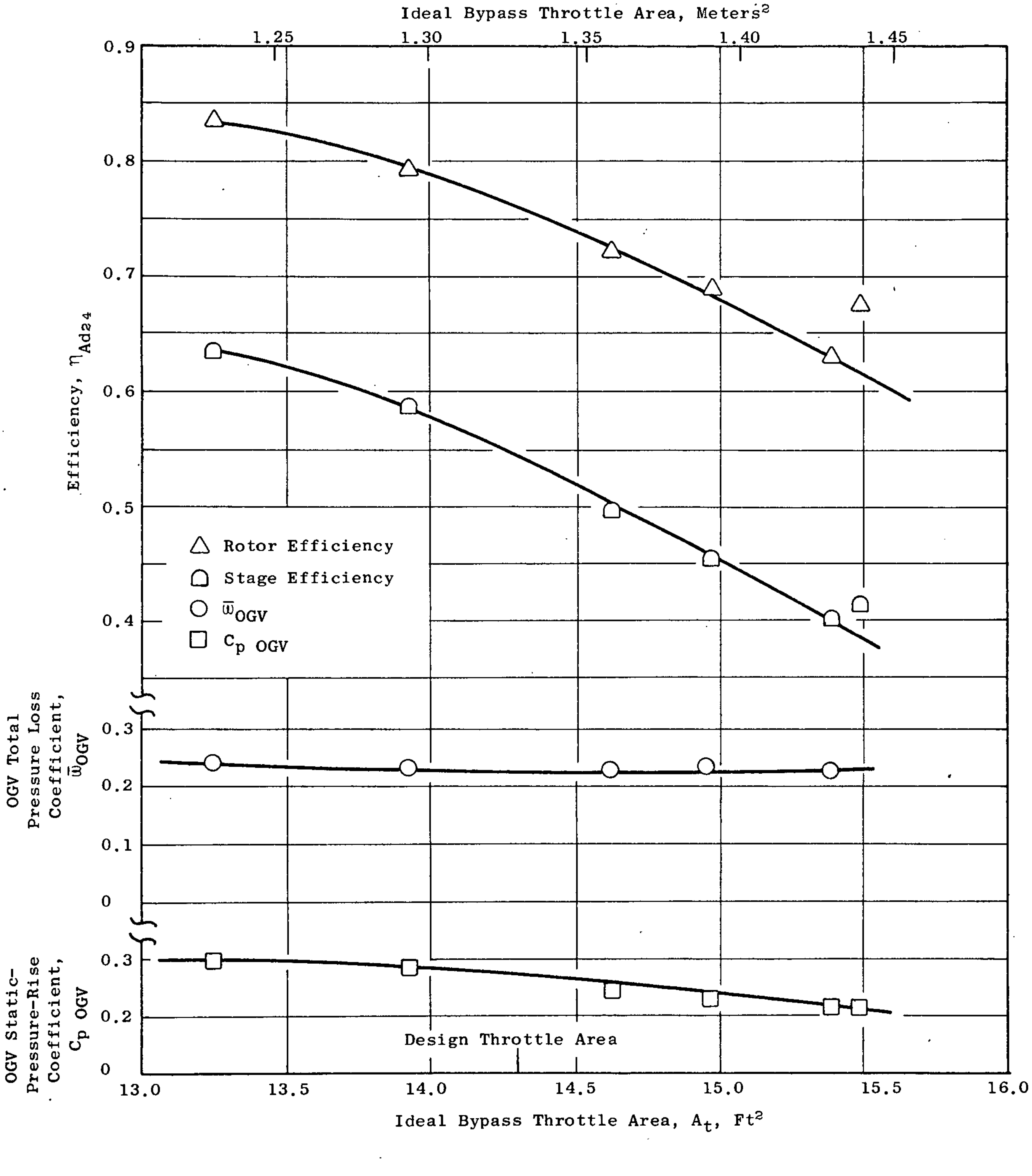

Figure 18. Variation of Element Properties with Throttling, Design Stream Function = 0.985 (Core ID).

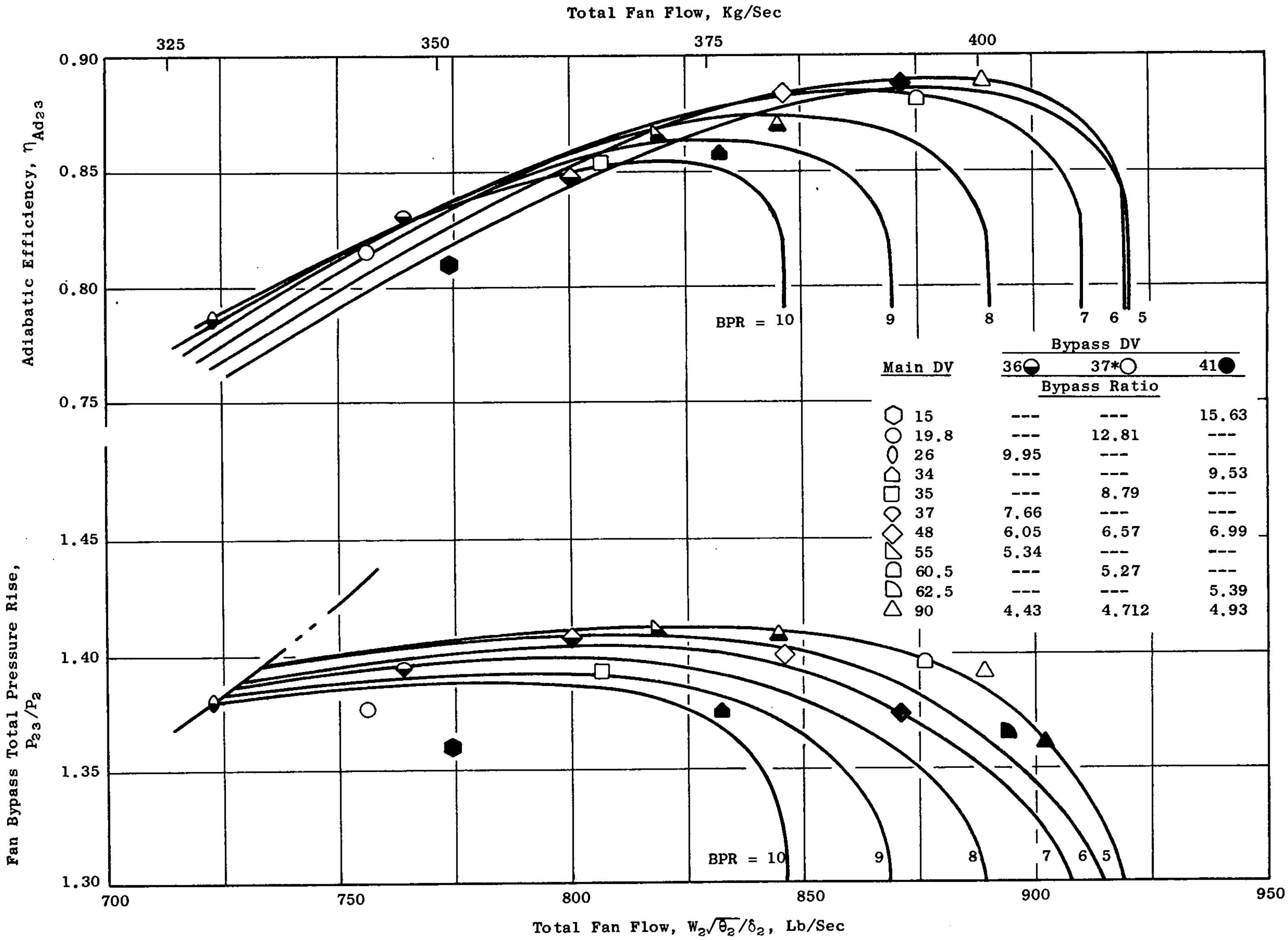

Figure 19. Bypass Ratio Excursion, Bypass Performance.

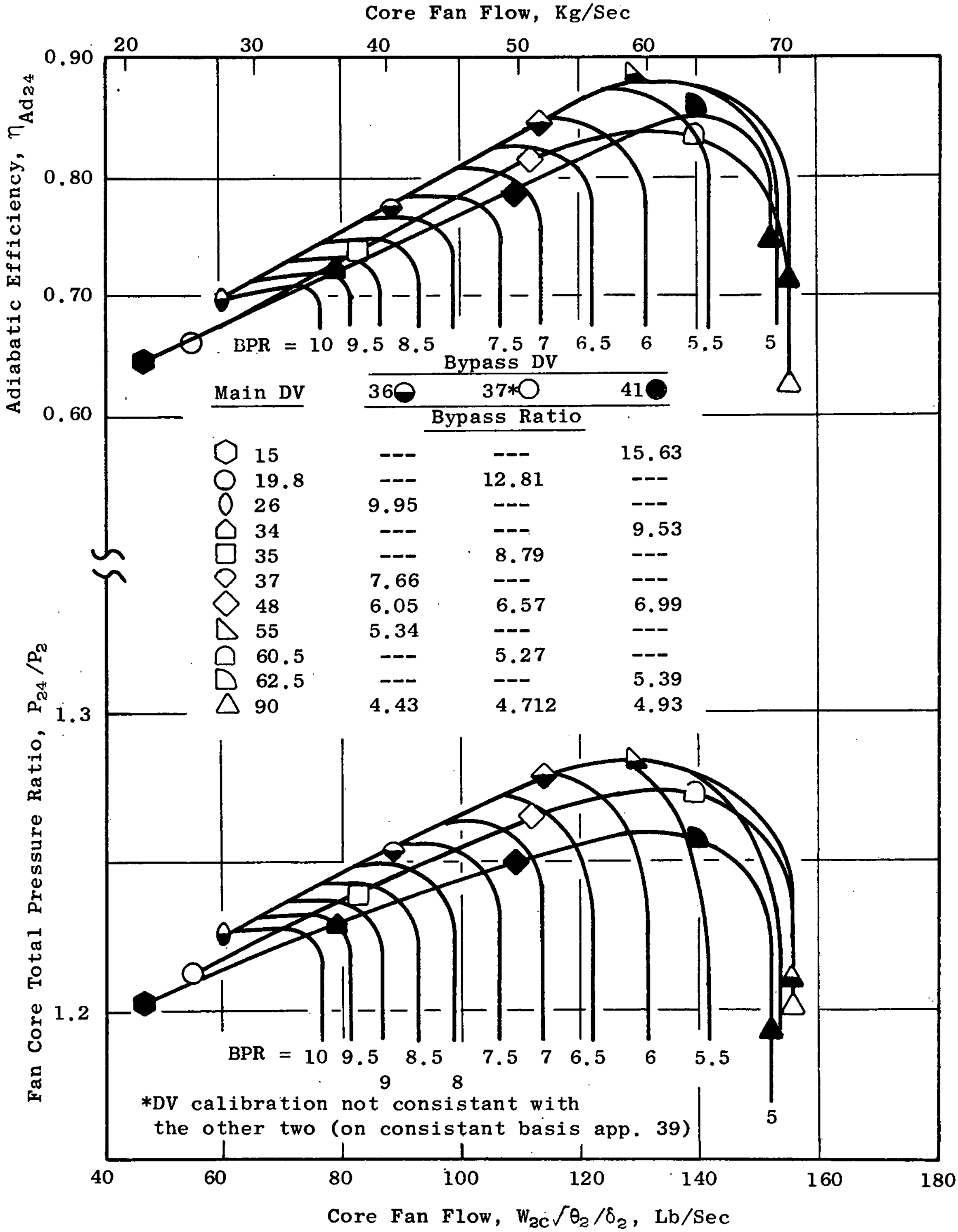

| Main DV | Bypass DV 36◒ | Bypass DV 37*○ | Bypass DV 41● |
|---|---|---|---|
|  | Bypass Ratio |  |  |
| ⬡ 15 | --- | --- | 15.63 |
| ○ 19.8 | --- | 12.81 | --- |
| 0 26 | 9.95 | --- | --- |
| ⌂ 34 | --- | --- | 9.53 |
| □ 35 | --- | 8.79 | --- |
| ♢ 37 | 7.66 | --- | --- |
| ◇ 48 | 6.05 | 6.57 | 6.99 |
| ◺ 55 | 5.34 | --- | --- |
| ⌓ 60.5 | --- | 5.27 | --- |
| D 62.5 | --- | --- | 5.39 |
| △ 90 | 4.43 | 4.712 | 4.93 |

*DV calibration not consistant with the other two (on consistant basis app. 39)

Figure 20. Bypass Ratio Excursion, Core Performance.

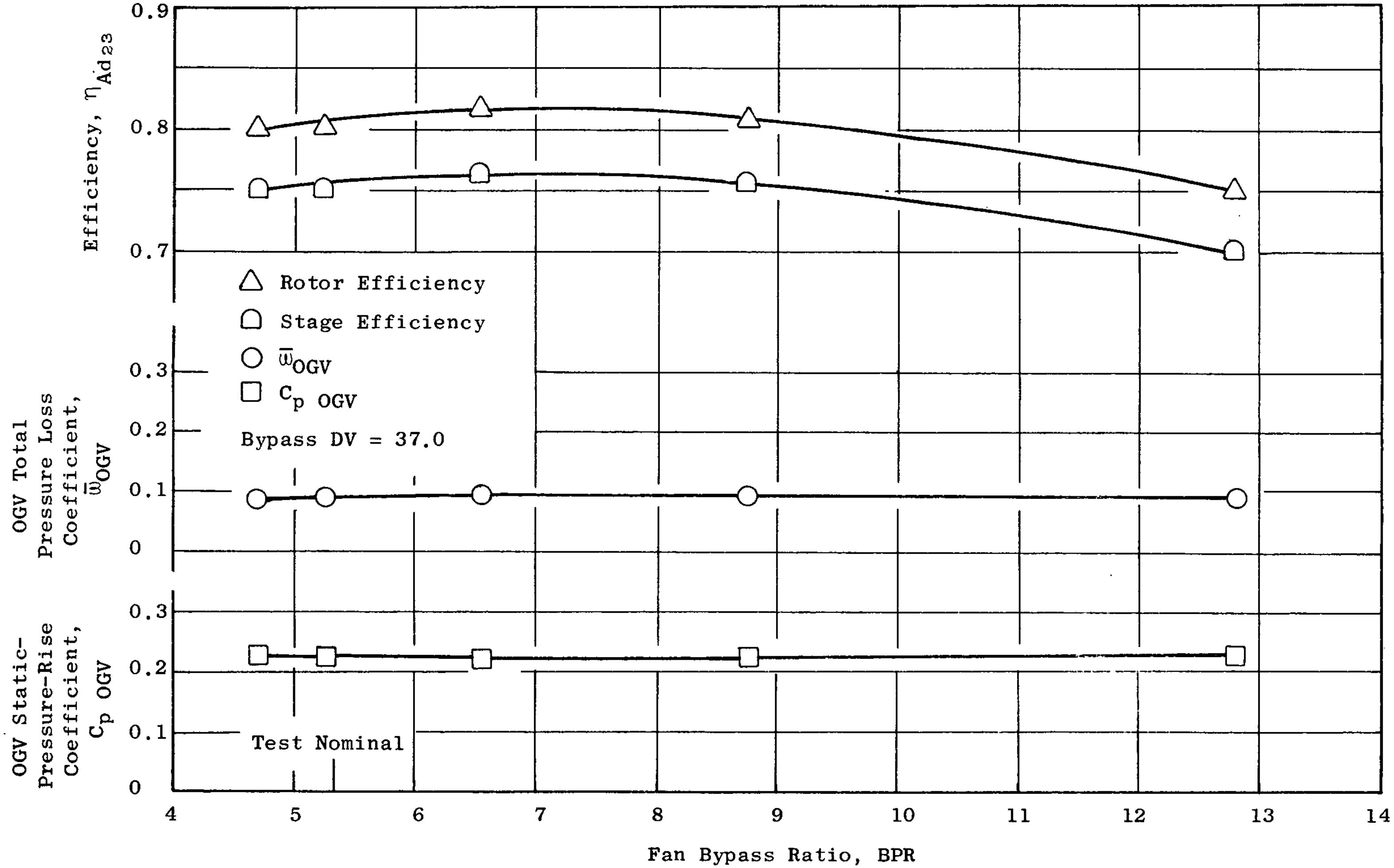

Figure 21. Variation of Element Properties with Bypass Ratio, Design Stream Function = 0.0606 (Bypass OD).

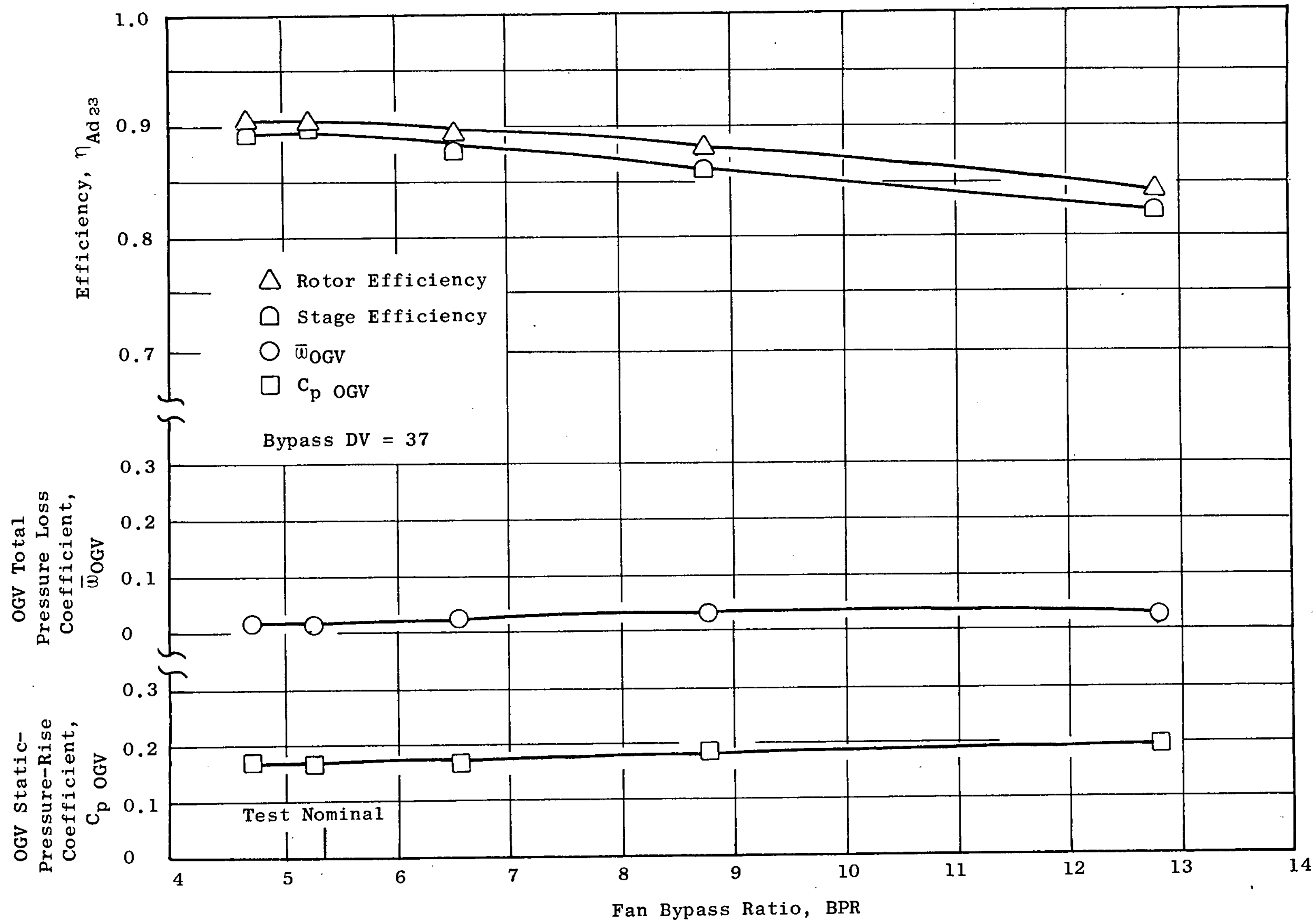

Figure 22. Variation of Element Properties with Bypass Ratio, Design Stream Function = 0.303.

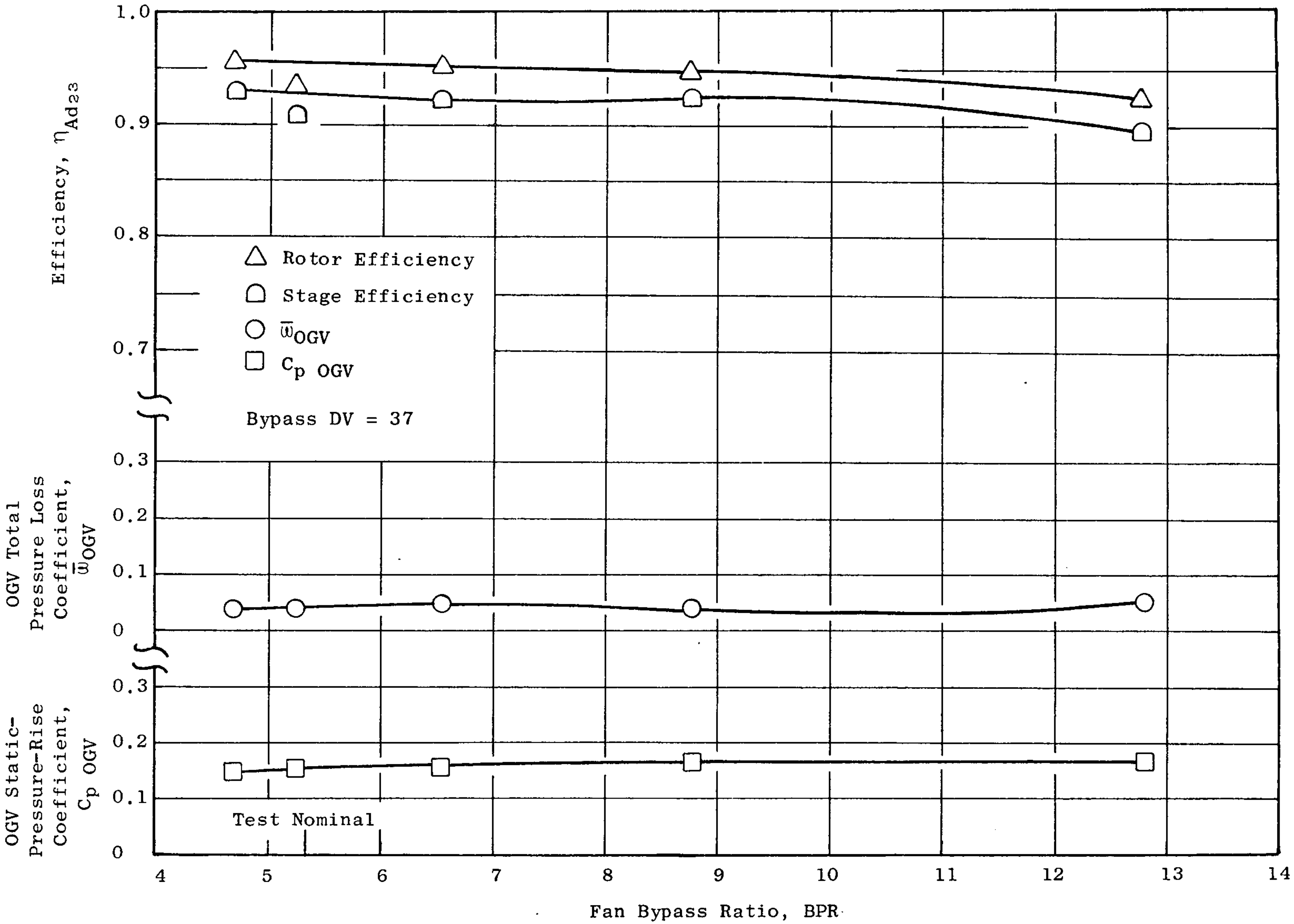

Figure 23. Variation of Element Properties with Bypass Ratio, Design Stream Function = 0.5454.

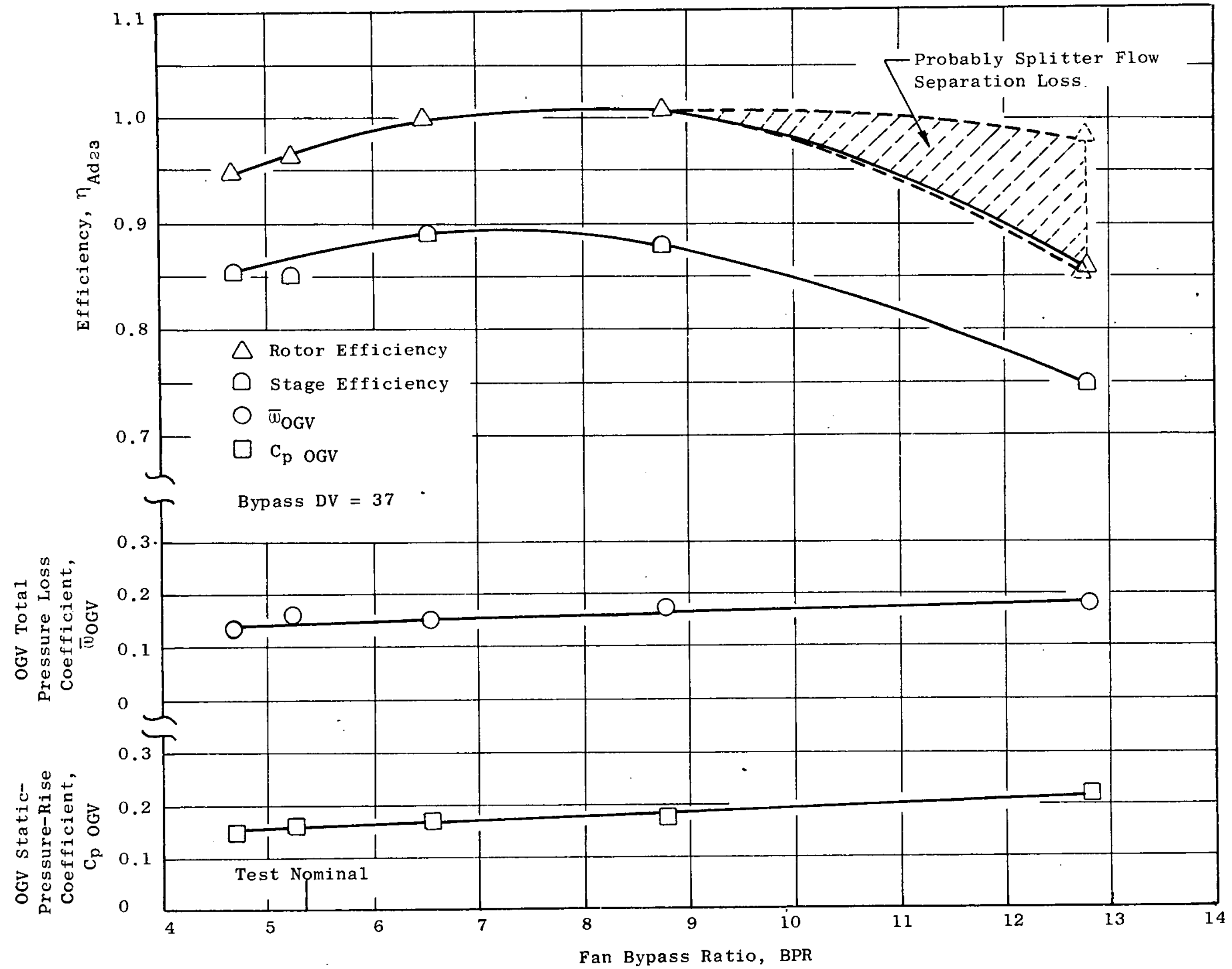

Figure 24. Variation of Element Properties with Bypass Ratio, Design Stream Function = 0.7878 (Bypass ID).

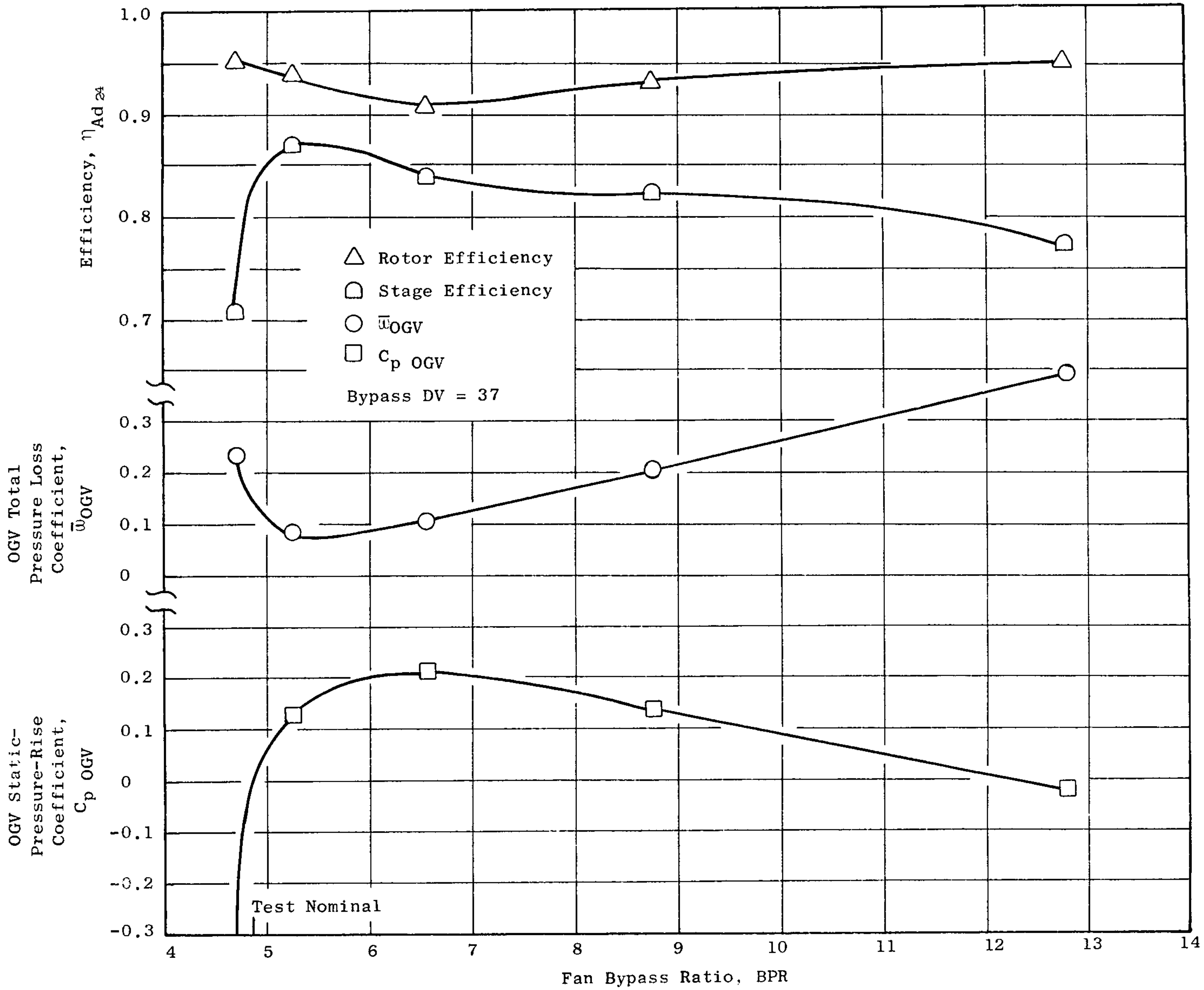

Figure 25. Variation of Element Properties with Bypass Ratio, Design Stream Function = 0.8637 (Core OD).

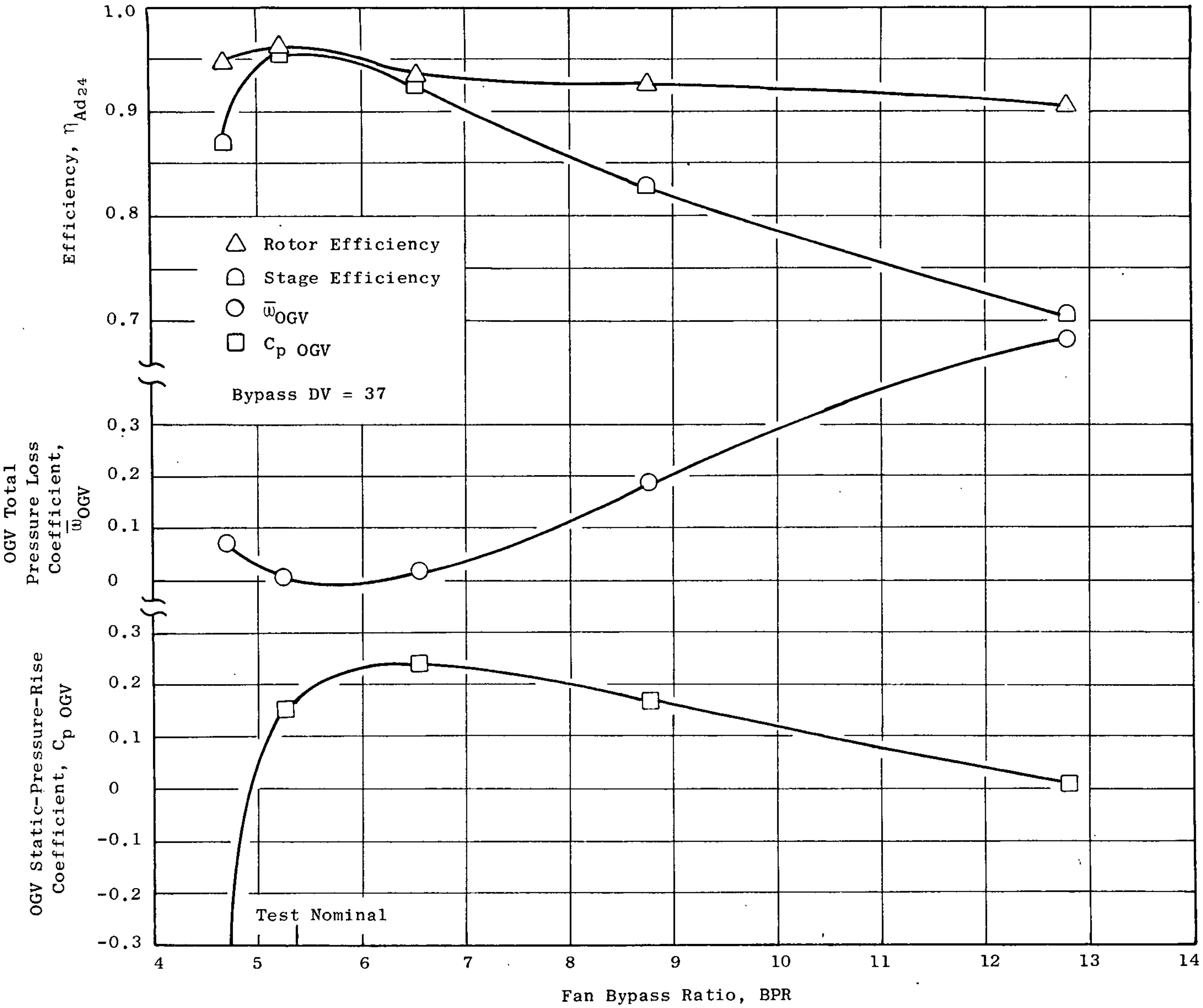

Figure 26. Variation of Element Properties with Bypass Ratio, Design Stream Function = 0.894.

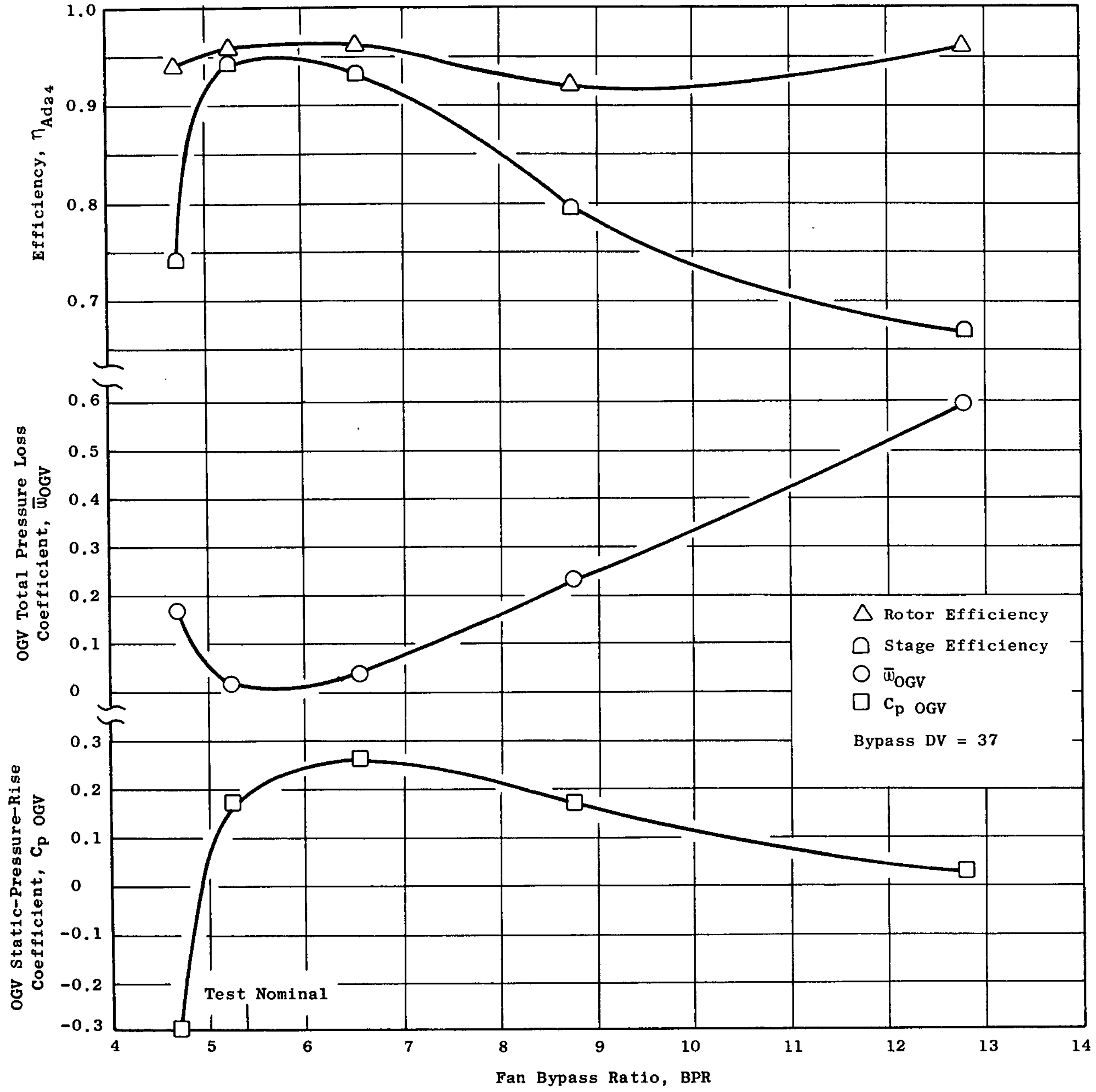

Figure 27. Variation of Element Properties with Bypass Ratio, Design Stream Function = 0.9243.

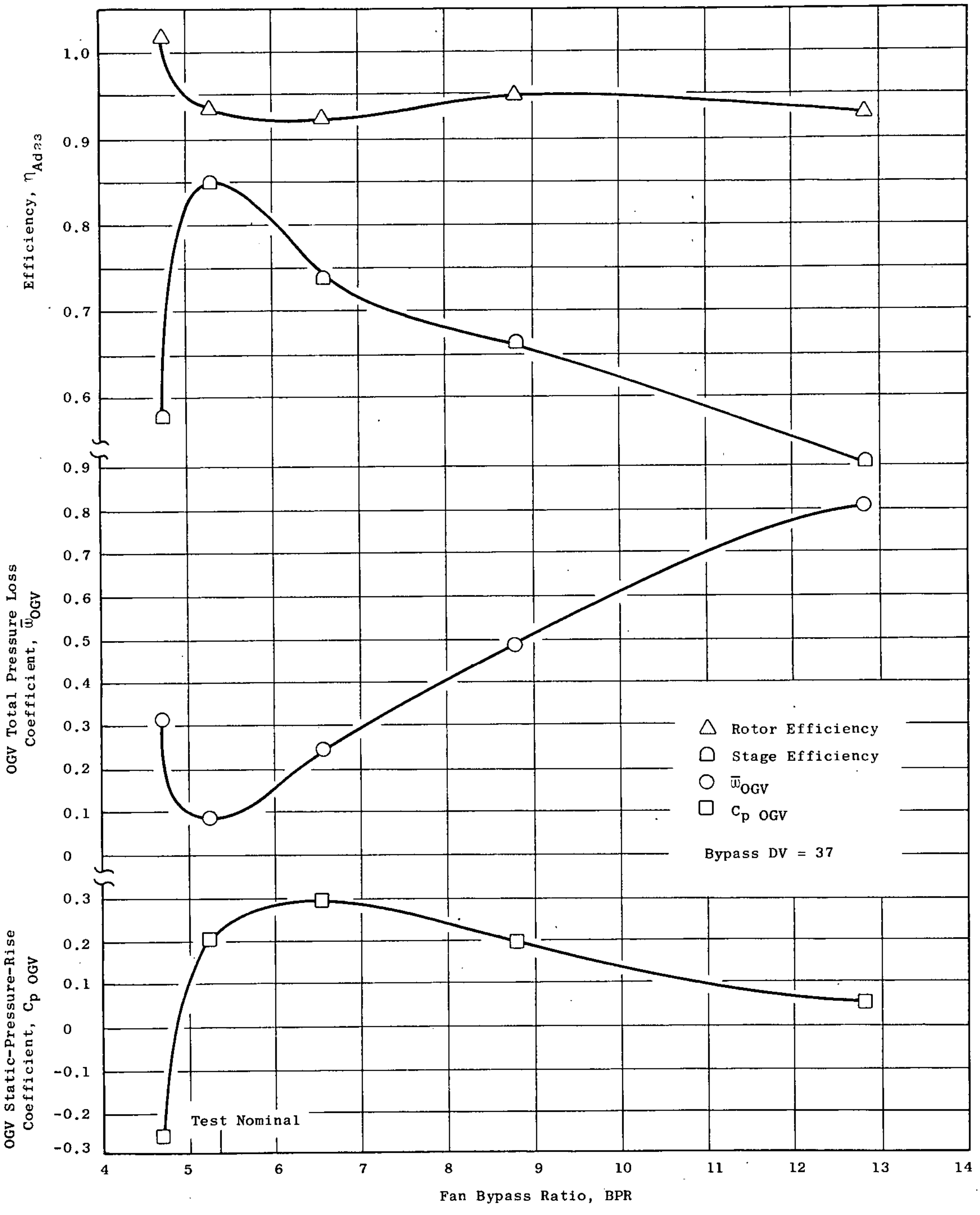

Figure 28. Variation of Element Properties with Bypass Ratio, Design Stream Function = 0.9546.

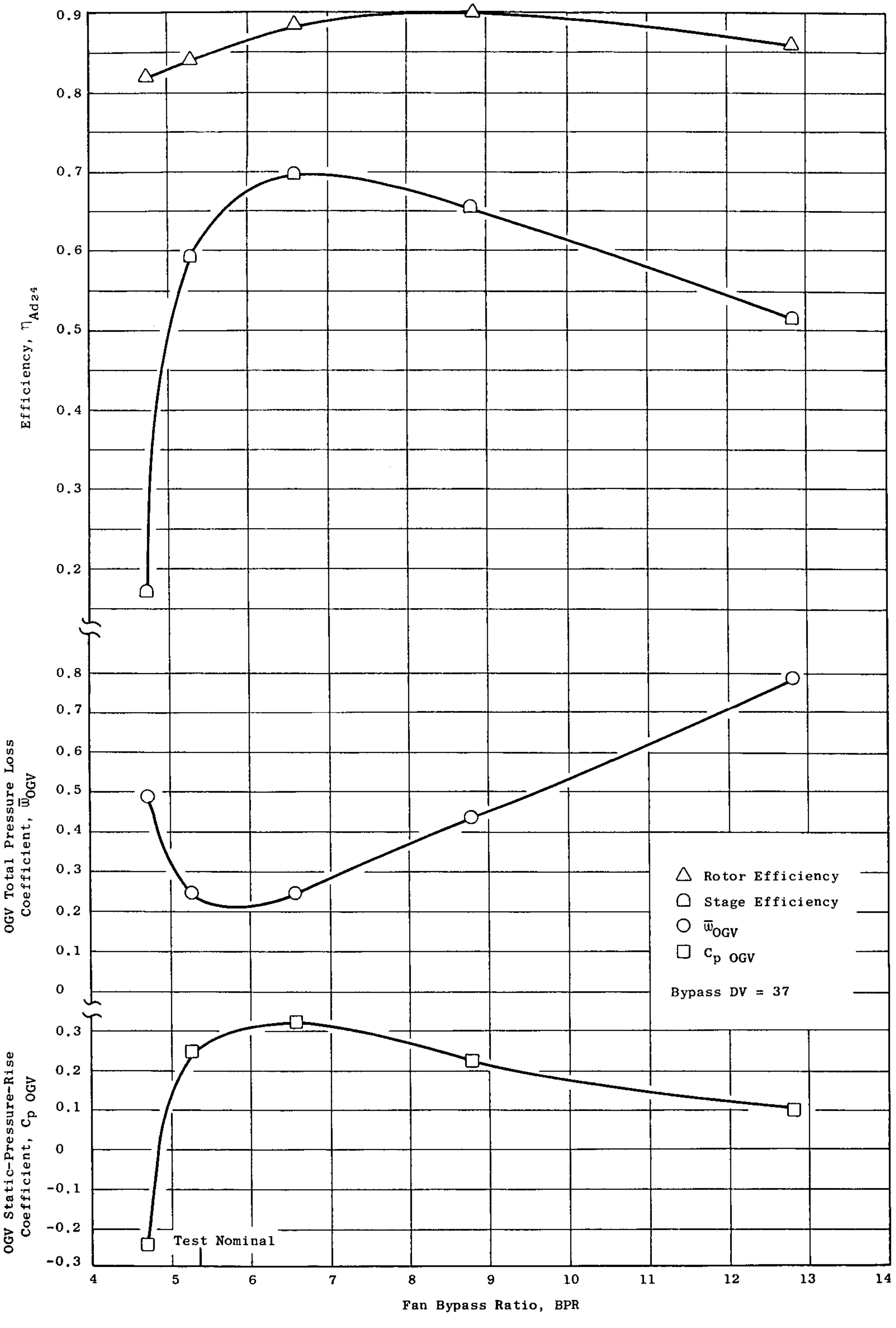

Figure 29. Variation of Element Properties with Bypass Ratio, Design Stream Function = 0.9849 (Core ID).

bypass ratio point. Discussion of this item is given later in this section.) Referring to Figures 25 through 29 for the fan core, the rotor efficiency is relatively unaffected by the bypass ratio migration. At lower than design bypass ratio, the negative static-pressure-rise coefficient and the rapid upswing in total-pressure-loss coefficient indicate the approach of a choke condition in the OGV. As bypass ratio is increased beyond about 6.5 the increase in total-pressure-loss coefficient and decrease in static-pressure-rise coefficient indicate high positive incidence in the OGV. The deterioration in stage efficiency at high bypass ratio is a reflection of the deteriorated OGV performance. Throughout the bypass ratio migration, continuous monitoring of blade and vane vibratory stresses and high response pressure transducers flush mounted in the casing at fan discharge and in the core flowpath did not indicate a fluctuating flow field as would be caused by a rotating stall zone.

Figure 30 shows the total pressure profile in front of the bypass and core OGV's and traces its development during the bypass ratio swing. A radial rake mounted on the splitter midway between fan rotor and OGV was used to determine the total pressure in the bypass stream. A circumferential average of the three radial rakes at core OGV inlet was used for total pressure in that portion of the annulus. Figure 31 shows the surface static pressure distribution on both the top side and the under side of the splitter and shows its variation with bypass ratio. The data presented in these two figures is from the same series of readings as the data from Figures 21 through 29 wherein the bypass discharge valve was set at 37.0 which back pressures the fan approximately the same as the design bypass nozzle.

Referring to Figure 30, the two highest bypass ratio readings show a deterioration in total pressure profile in the bypass region near the splitter. The high angle of attack forced on the splitter during high bypass ratio operation creates a severe aerodynamic loading on the bypass side leading edge region, as evidenced by the splitter surface static pressure distribution shown in Figure 31, which causes high losses and ultimately will produce a flow separation from the surface. The lack of significant deterioration in the fan core indicates that the rotor performance is not adversely affected by the bypass ratio migration. The previously noted apparent drop in rotor and stage efficiency in Figure 24 can be explained by the high splitter loss since the method used to determine the efficiencies is not capable of separating the rotor and splitter performance. The fact that the rotor and stage efficiency in Figure 24 deteriorate by an approximately equal amount, hence the OGV total-pressure-loss coefficient remains relatively unchanged, indicates that the performance of the OGV is not seriously affected by the high splitter loss, at least over the range tested.

### 5.2.4 Bypass OGV Schedule

A brief investigation to verify the correctness of the bypass OGV setting was conducted at 95% corrected speed for an approximate nominal fan bypass operating line. At this condition, which corresponds to a bypass pressure ratio of 1.45, the bypass OGV was opened and closed 4°. The recorded bypass overall efficiencies were 87.49% and 87.99%, for the

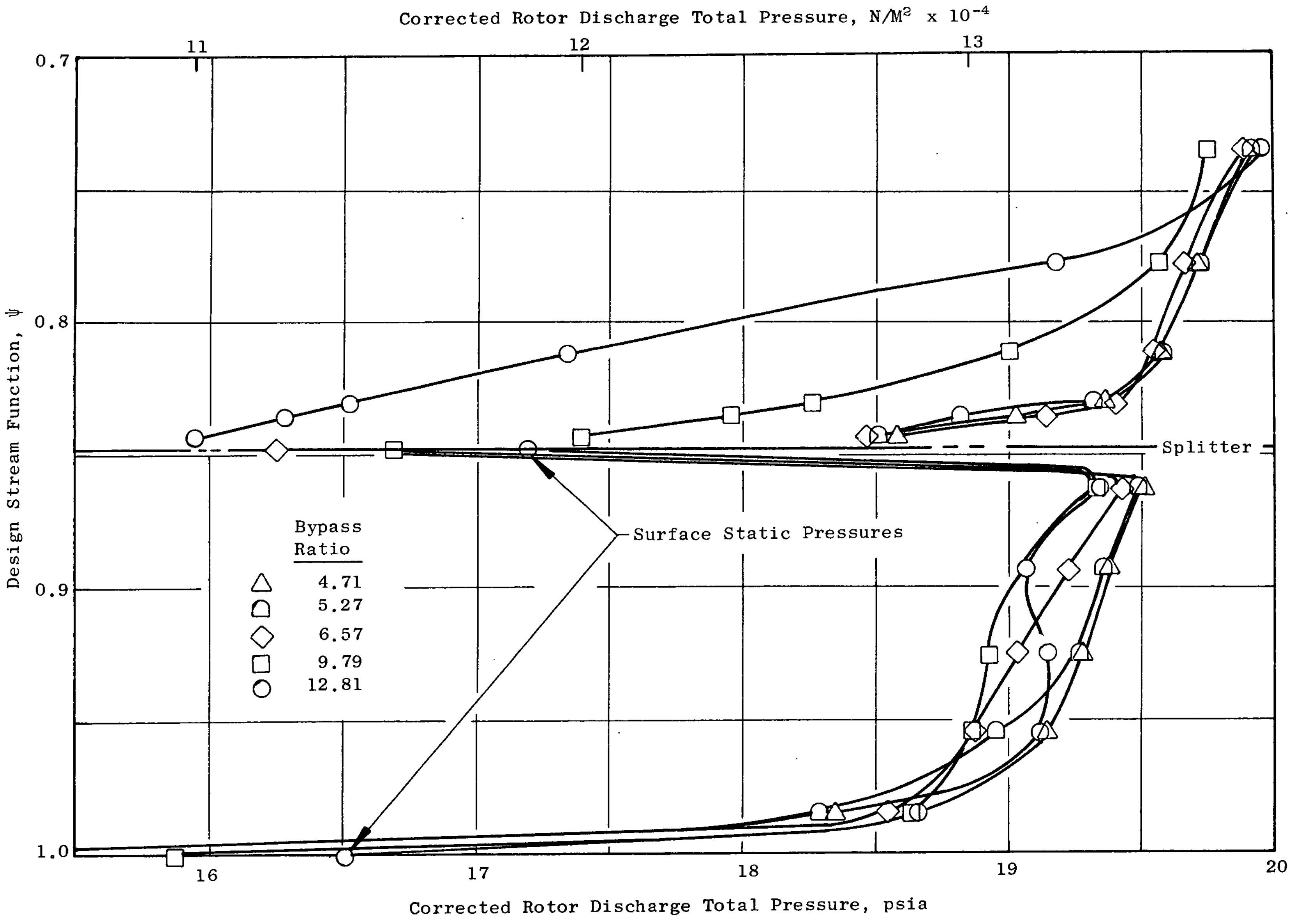

Figure 30. Effect of Bypass Ratio on Rotor Hub Total Pressure Profile.

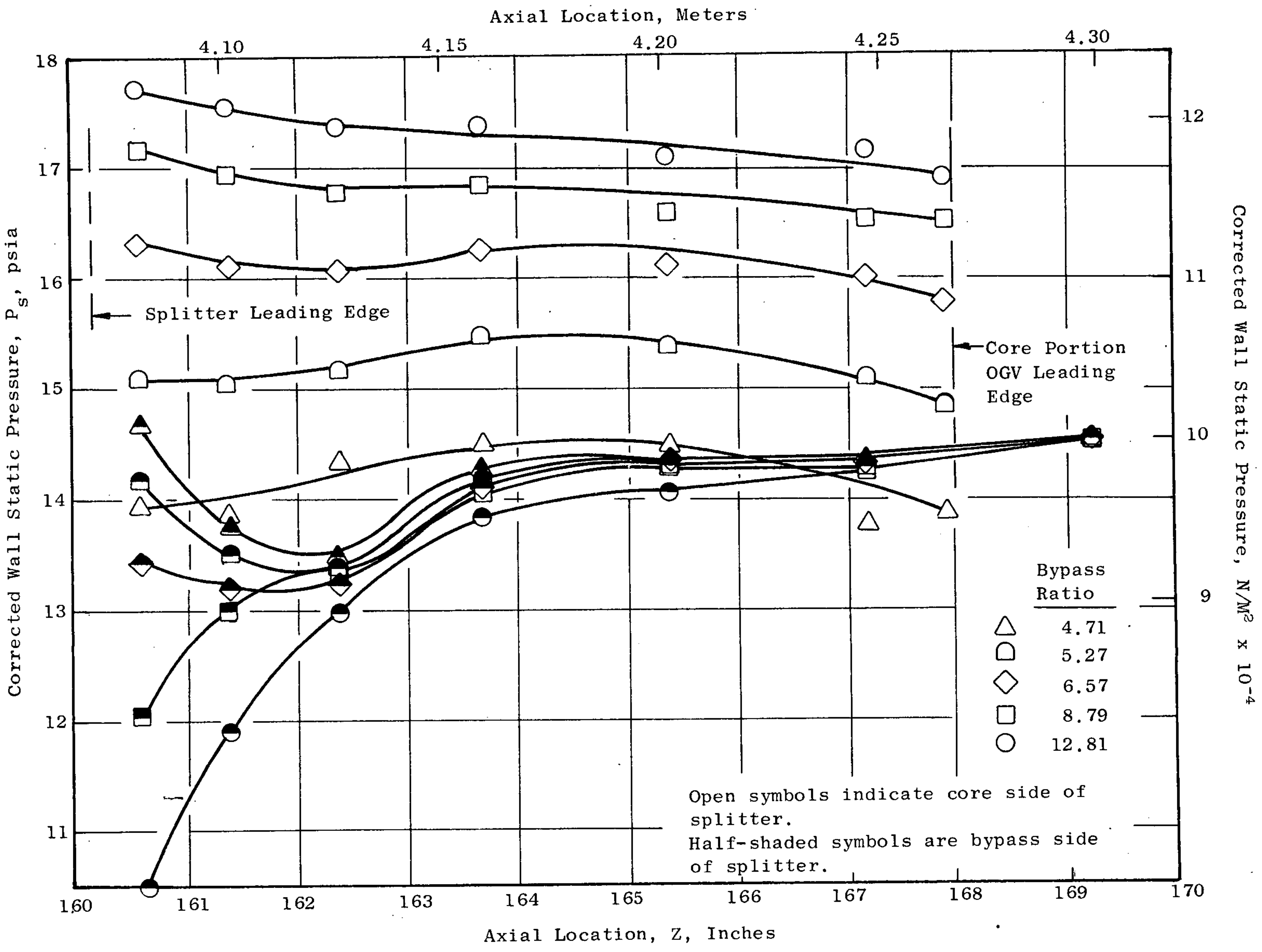

Figure 31. Effect of Bypass Ratio on Splitter Wall Static Pressure.

opening and closing, respectively, compared to a 90.73% bypass overall efficiency with the nominal OGV setting. Examination of the bypass overall performance map, Figure 4, indicates the 90.73% efficiency with the nominal OGV setting to be unreasonably high in that it is not consistent with the data for adjacent throttle settings at 95% corrected speed nor with the data for adjacent speeds. Assuming the map efficiency of 88.6% for the nominal OGV setting, opening or closing of the OGV setting results in an efficiency detoriation. Alternately, consideration of the opening and closing by itself shows a total efficiency spread of 0.50 points which indicates a relatively low sensitivity of efficiency change to setting angle change. Accordingly, it was judged that the nominal vane setting was near optimum at the design operating line.

### 5.2.5 Traverse Data

Traverse data at 100% corrected speed, at an operating point slightly above the design operating line, are presented in Figures 32 through 40. This type of data is used primarily to indicate flow profile trends; it is not used for performance computations. The data was taken at four axial planes; rotor inlet, rotor discharge, bypass OGV inlet, and fan core OGV inlet. A major purpose for the traverses at two axial locations behind the rotor was the determination of any detrimental effects on the flow caused by the large axial gap between blade rows. In the bypass, Figures 32 through 36, no obvious serious defects are observed. This is evidenced by the general agreement between the design and measured radial distributions. The difference between the design and measured levels is not understood except for the small portion attributable to the higher than design back pressure at the traverse reading. Careful examination of the total pressure traverse, Figure 32, indicates a relatively larger wall boundary layer velocity defect at OGV inlet than at rotor exit in the bypass OD and ID regions. This is evidenced by the larger difference between the local tip and hub values of total pressure compared to the adjacent free-stream values of total pressure. This increased velocity defect is a contribution to the larger than design OGV total-pressure-loss coefficients in the vane end regions. For the fan core, Figures 37 through 40 (a replot of the information shown in Figures 32 through 35 with an expanded scale on the core portion), the major defect observed is in total pressure near the hub. Since the work input, temperature rise, remains near the design level, the total pressure defect is a result of the hub efficiency defect. As was previously discussed in relation to Figure 6, the hub defect is in a region, for a conventional fan arrangement, relatively deep within the end wall boundary layer.

## 5.3 DISTORTED FLOW PERFORMANCE

Fan A was tested with tip radial, crosswind, and one-per-rev circumferential inlet flow distortions. The distortion was generated by screens mounted on a support structure which was located approximately 0.6 fan diameters in front of the rotor. The tip radial distortion generating screen covered the outer 40% of the annulus. The crosswind distortion

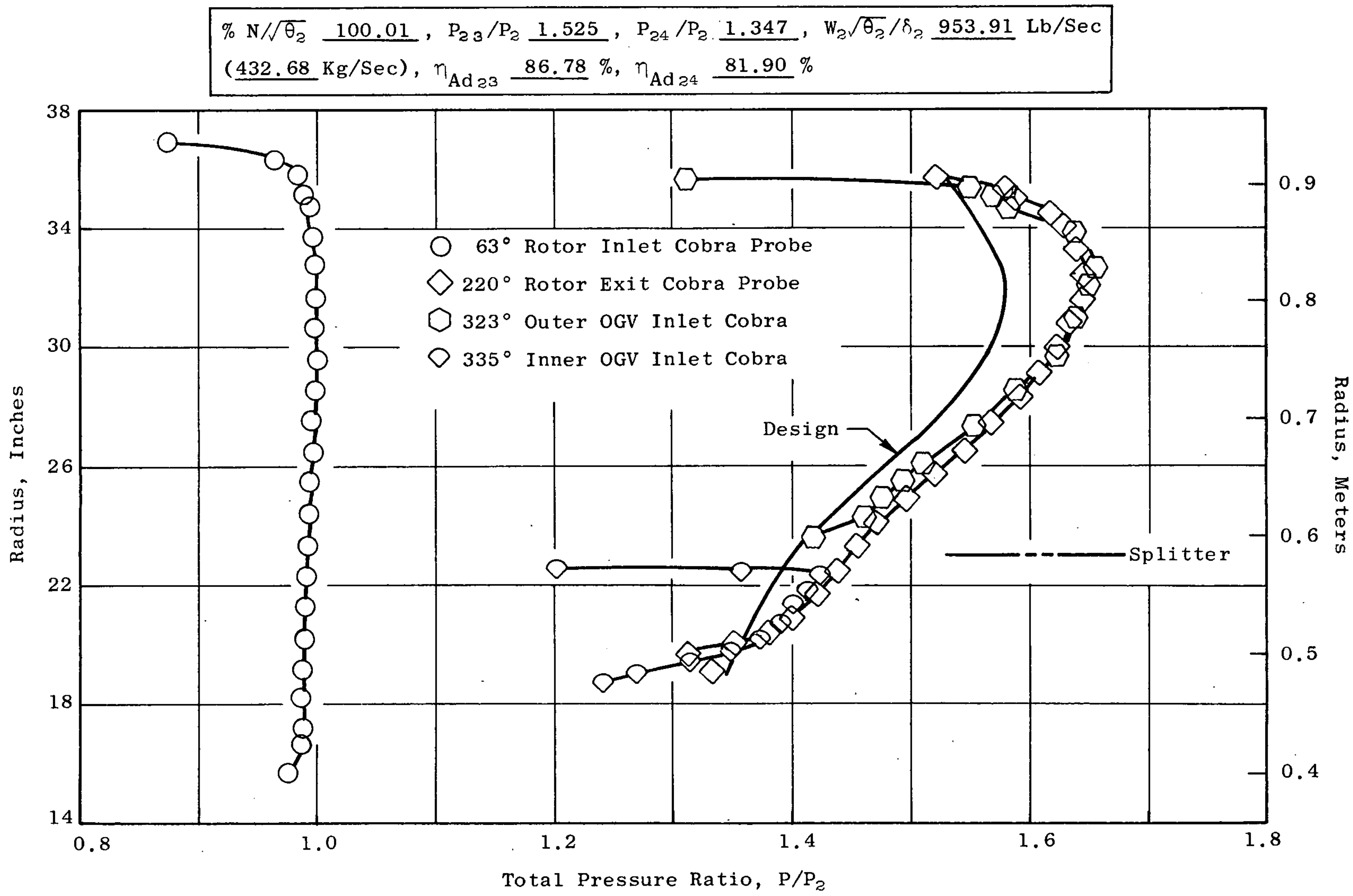

Figure 32. Traverse Radial Profiles, Radius Vs. Total Pressure Ratio (Bypass).

% $N/\sqrt{\theta_2}$ 100.01 , $P_{23}/P_2$ 1.525 , $P_{24}/P_2$ 1.347 , $W_2\sqrt{\theta_2}/\delta_2$ 953.91 Lb/Sec
(432.68 Kg/Sec), $\eta_{Ad_{23}}$ 86.78 %, $\eta_{Ad_{24}}$ 81.90 %

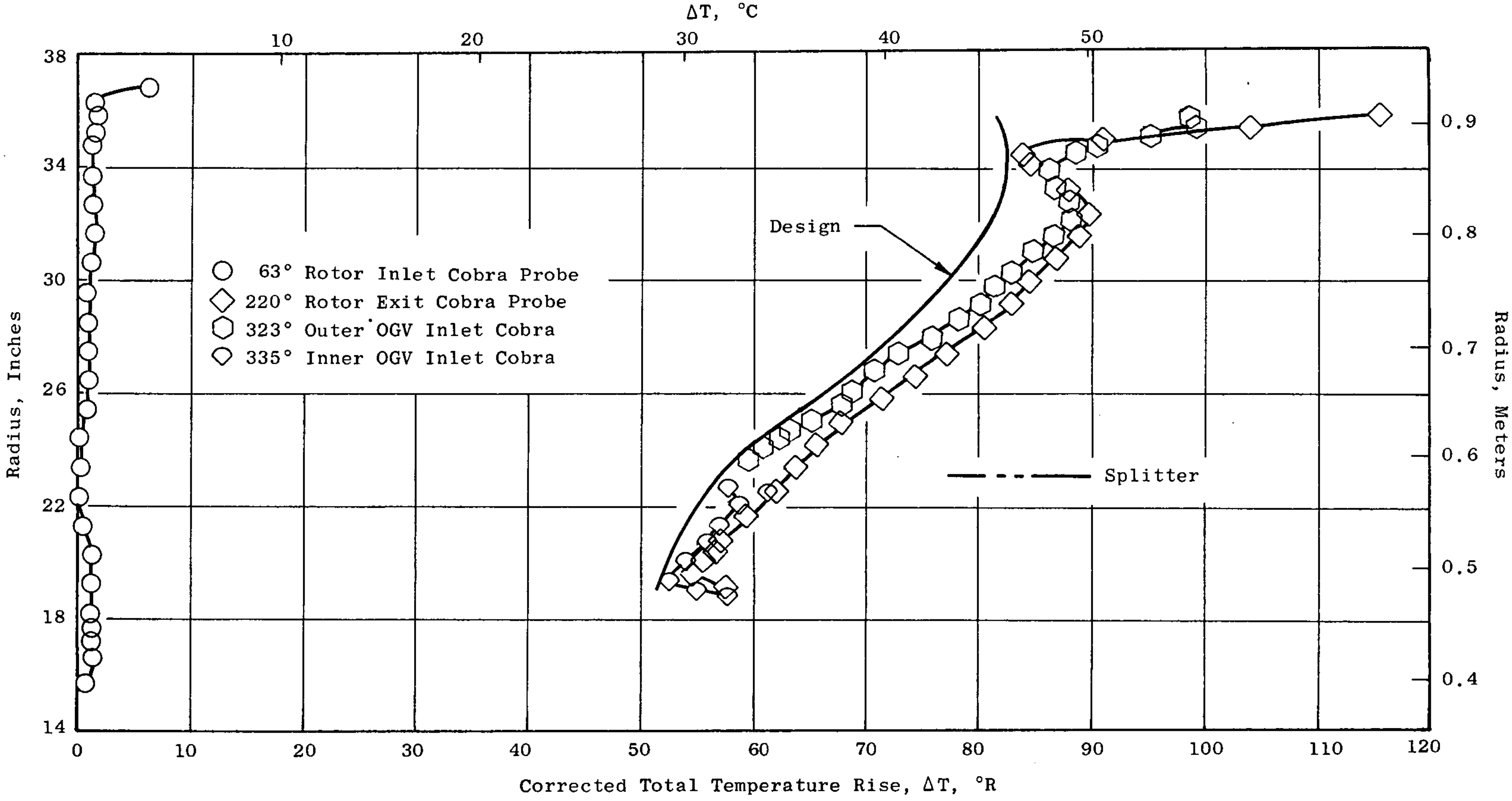

Figure 33. Traverse Radial Profiles, Radius Vs. Corrected Total Temperature Rise (Bypass).

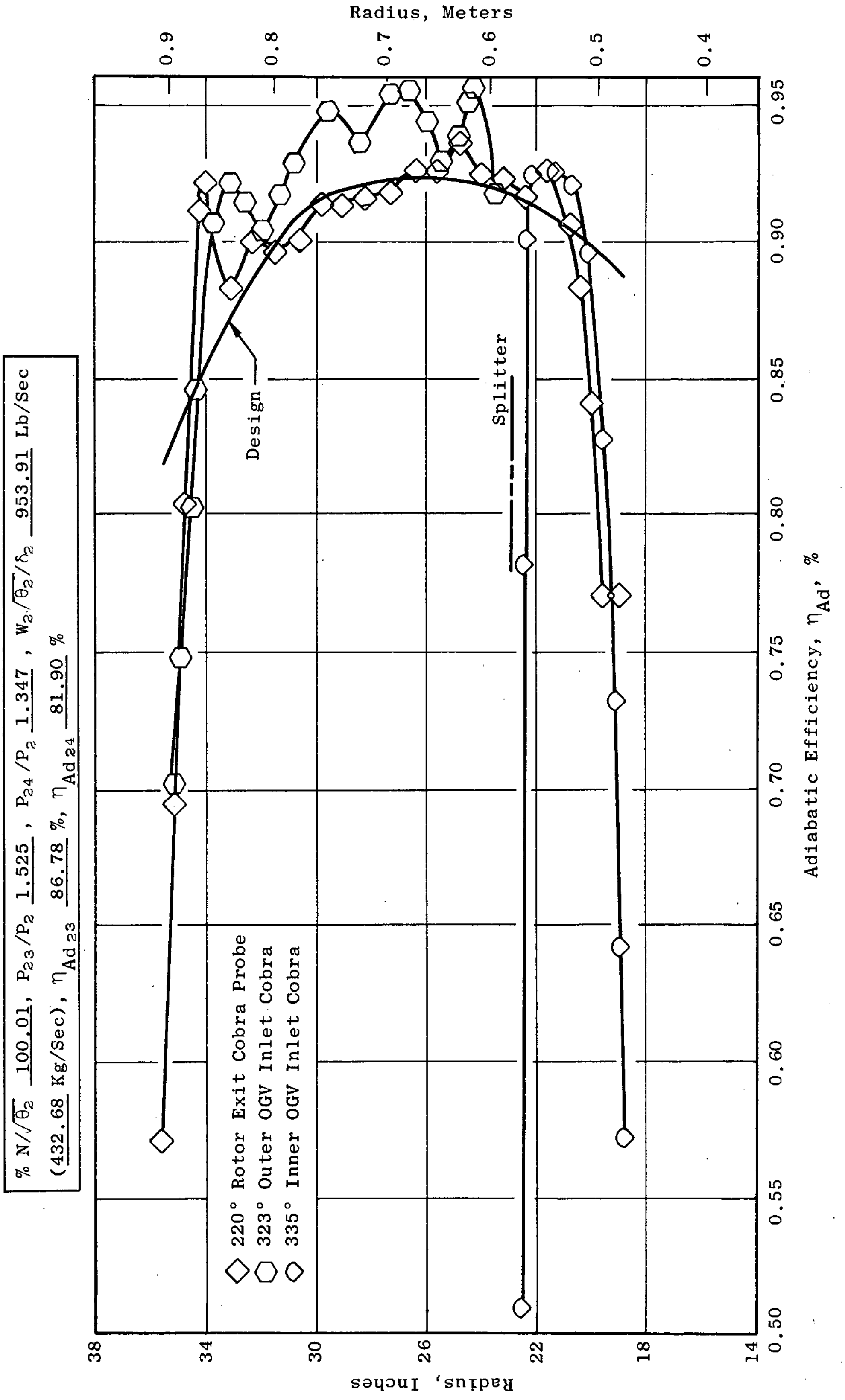

Figure 34. Traverse Radial Profiles, Radius Vs. Adiabatic Efficiency (Bypass).

% $N/\sqrt{\theta_2}$ 100.01 , $P_{23}/P_2$ 1.525 , $P_{24}/P_2$ 1.347 , $W_2\sqrt{\theta_2}/\delta_2$ 953.91 Lb/Sec (432.68 Kg/Sec), $\eta_{Ad\,23}$ 86.78 %, $\eta_{Ad\,24}$ 81.90 %

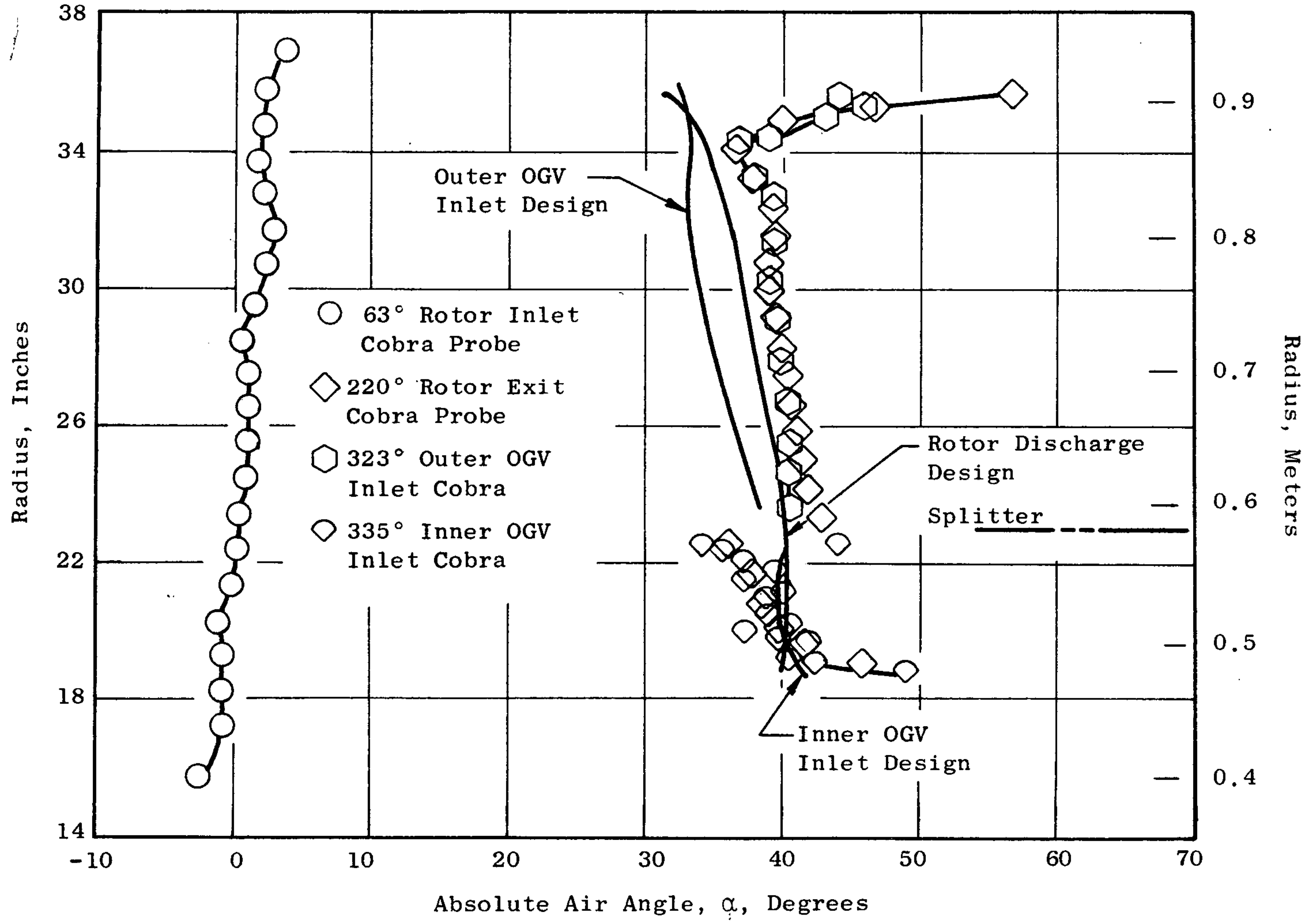

Figure 35. Traverse Radial Profiles, Radius Vs. Absolute Air Angle (Bypass).

$\% \ N/\sqrt{\theta_2}$ 100.01 , $P_{23}/P_2$ 1.525 , $P_{24}/P_2$ 1.347 , $W_2\sqrt{\theta_2}/\delta_2$ 953.91 Lb/Sec (432.68 Kg/Sec), $\eta_{Ad\,23}$ 86.78 %, $\eta_{Ad\,24}$ 81.90 %

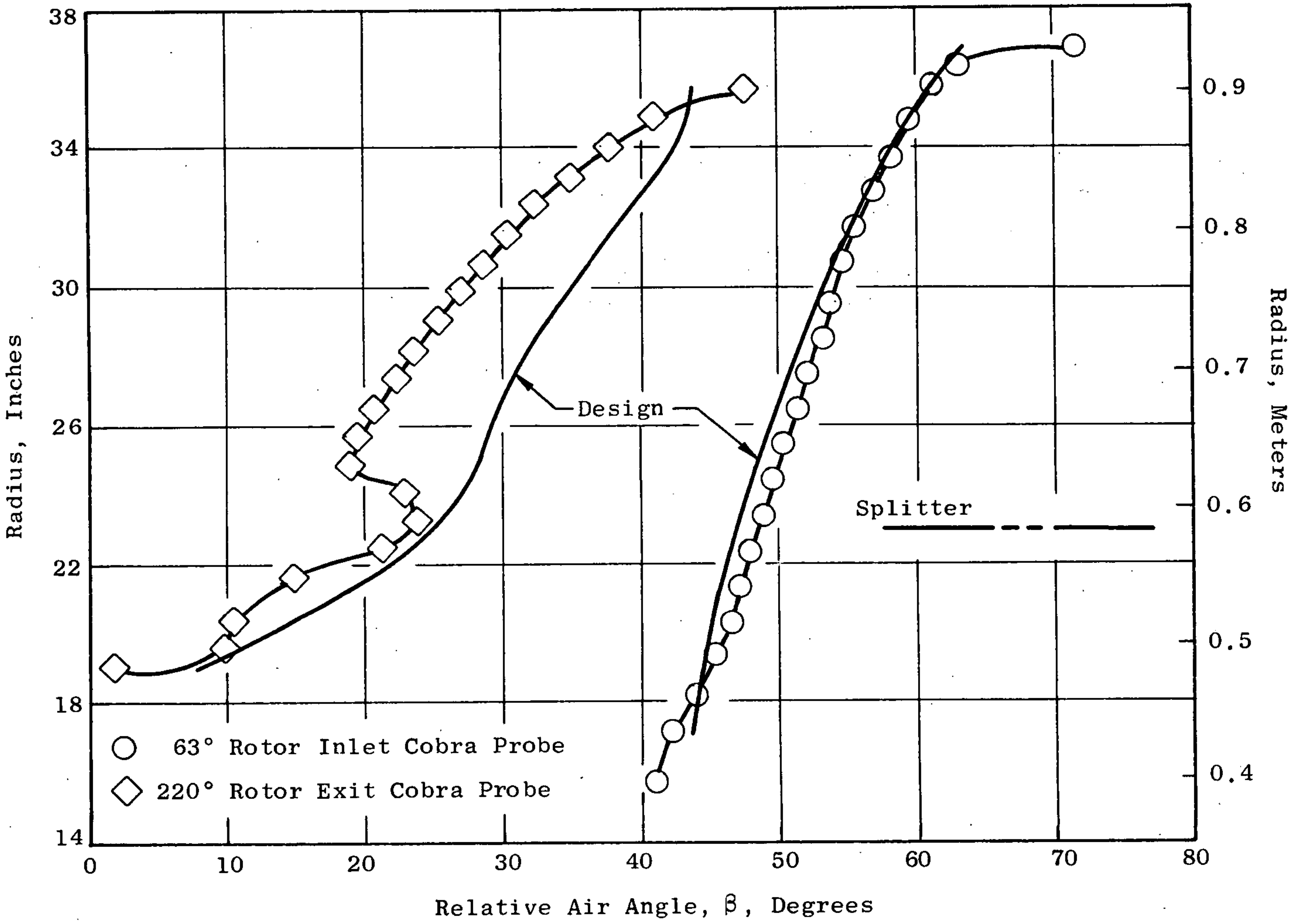

Figure 36. Traverse Radial Profiles, Radius Vs. Relative Air Angle (Bypass).

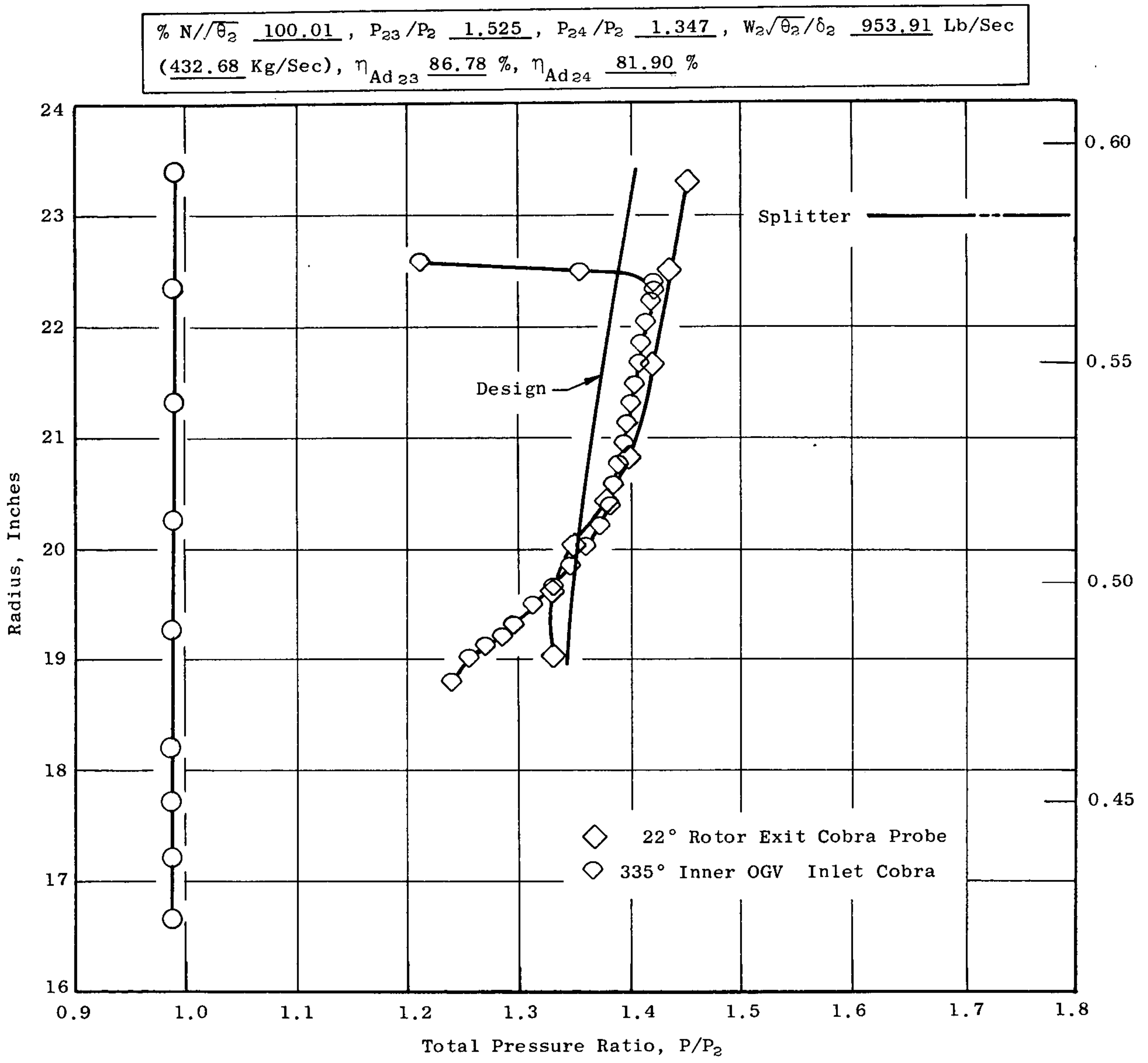

Figure 37. Traverse Radial Profiles, Radius Vs. Total Pressure Ratio (Core).

% $N/\sqrt{\theta_2}$ 100.01, $P_{23}/P_2$ 1.525, $P_{24}/P_2$ 1.347, $W_2\sqrt{\theta_2}/\delta_2$ 953.91 Lb/Sec (432.68 Kg/Sec), $\eta_{Ad\,23}$ 86.78 %, $\eta_{Ad\,24}$ 81.90 %

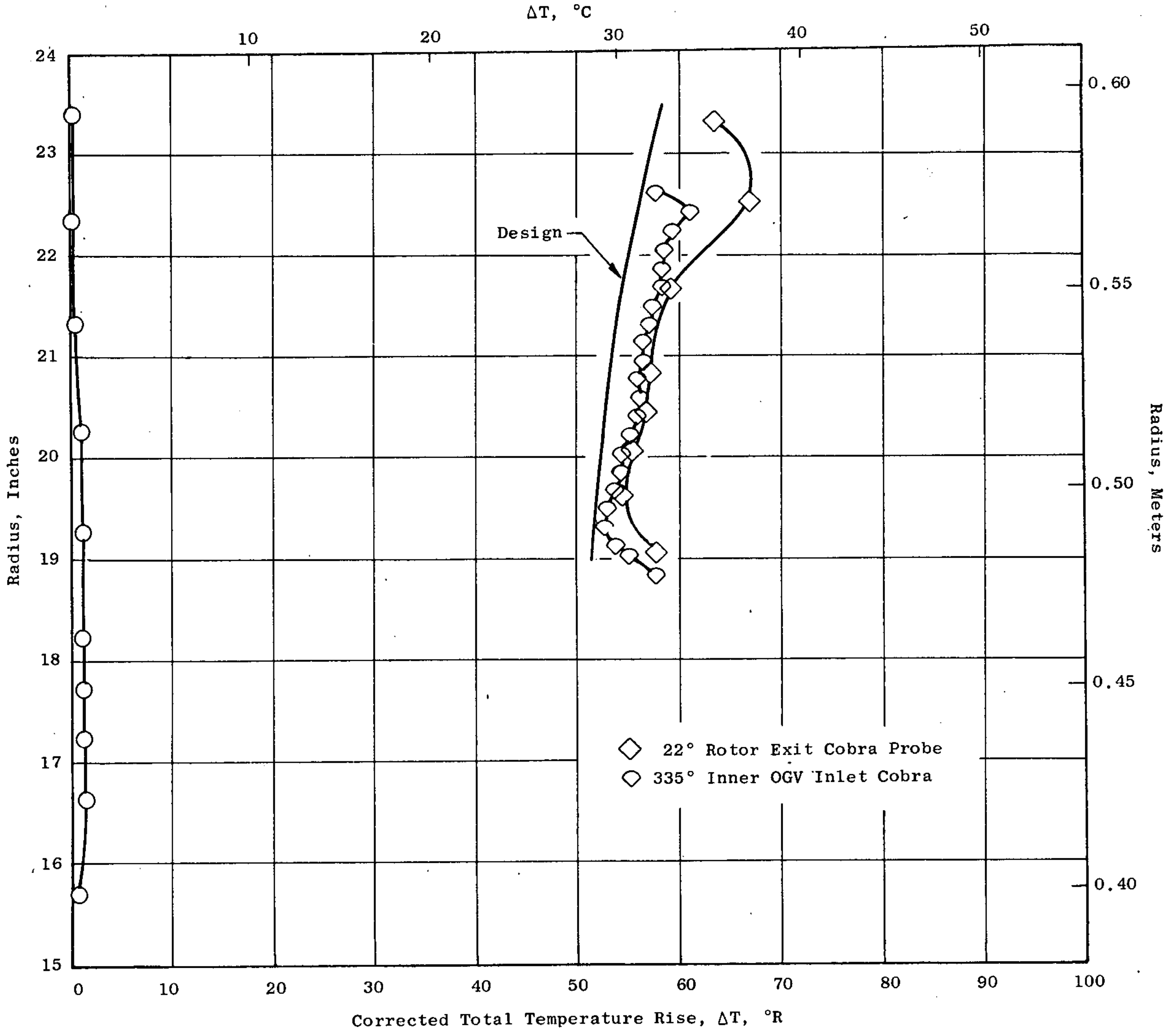

Figure 38. Traverse Radial Profiles, Radius Vs. Corrected Total Temperature Rise (Core).

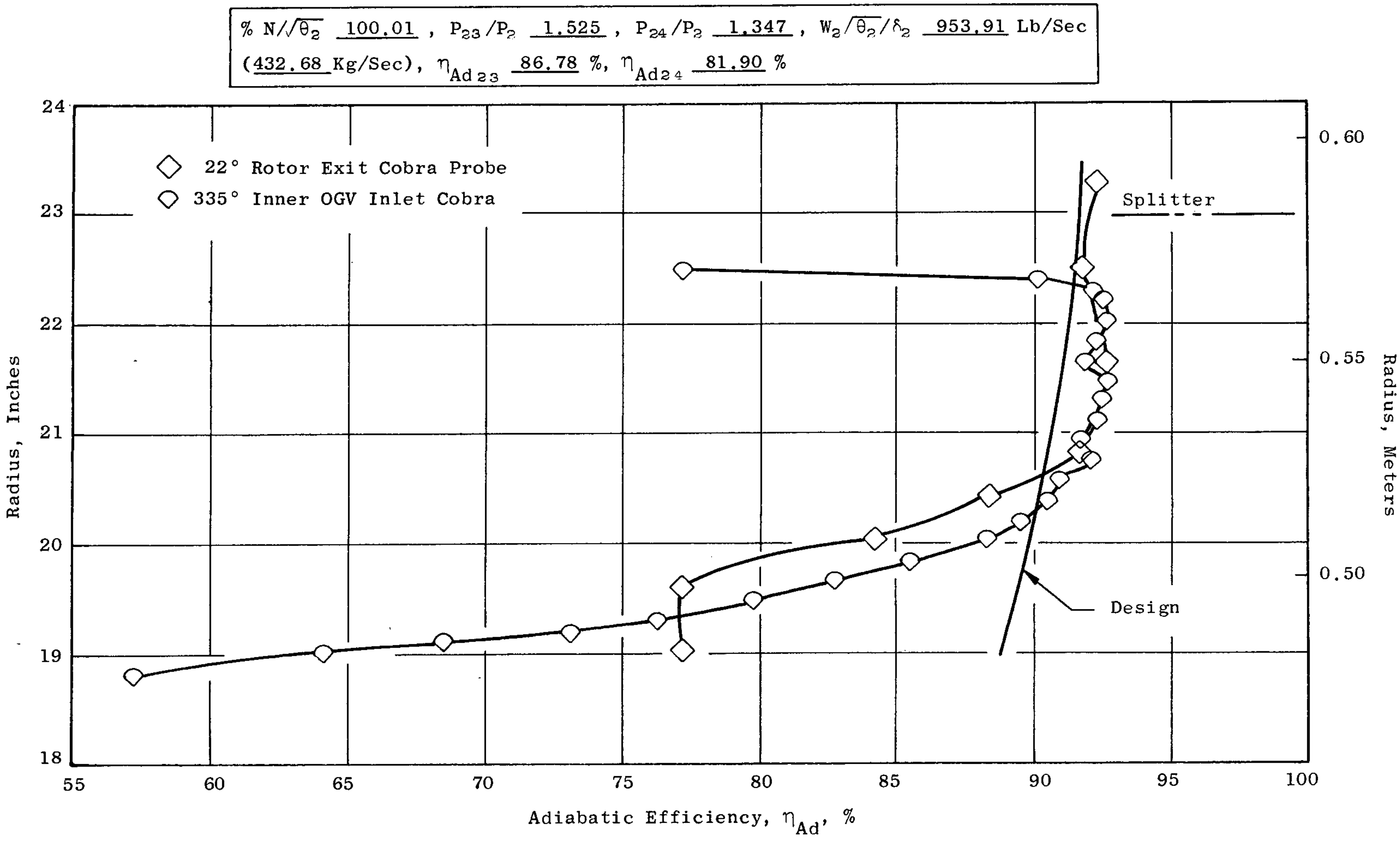

Figure 39. Traverse Radial Profiles, Radius Vs. Adiabatic Efficiency (Core).

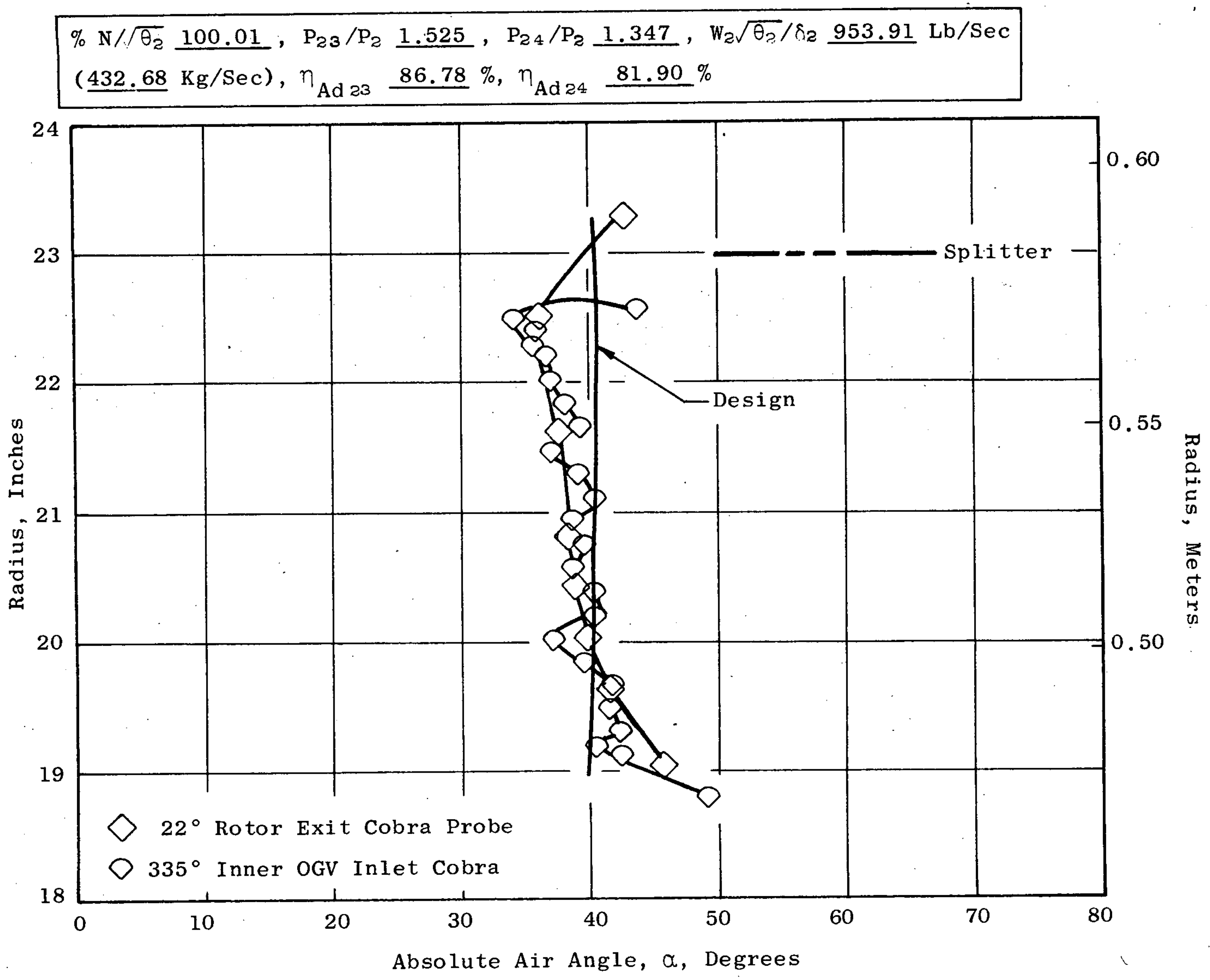

Figure 40. Traverse Radial Profiles, Radius Vs. Absolute Air Angle (Core).

generating screen had a circumferential extent of 160° and a radial extent covering 30% of the annulus area with the outermost 10% and the innermost 60% of the annulus area being open. The one-per-rev distortion generating screen extended over the full annulus height and was 180° in circumferential extent. The distortion levels generated by the screens are shown in Figure 44. Plots of the actual distortion patterns for a relatively closed throttle condition at 90% speed are shown in Figures 42 through 44. A contour plot of the inlet recovery pattern for the crosswind distortion is shown in Figure 45.

The overall performance maps for the distorted flow testing are shown in Figures 46 through 48. Also shown in the background is the undistorted inlet limit line to facilitate comparison. The one-per-rev distortion indicates a stall line improvement at all speeds relative to undistorted inlet testing. This result is generally contrary to past test experience which indicates that one-per-rev circumferential inlet flow distortion yields a small, but definite, stall line degradation relative to undistorted inlet operation. It is believed that the apparent stall line increase is a result of inadequate data sampling and the lack of adequate weighting procedures in the data reduction. The crosswind distortion resulted in a moderate stall line decrease. The tip radial distortion resulted in a far greater stall line reduction than either of the other two patterns. This large stall line reduction with tip radial inlet distortion is consistent with test experience on other single stage fans. In the distortion data reduction, no attempt was made to segregate the inlet pressures to account for a lower than average pressure entering the bypass portion with the tip radial and crosswind distortions.

C.2

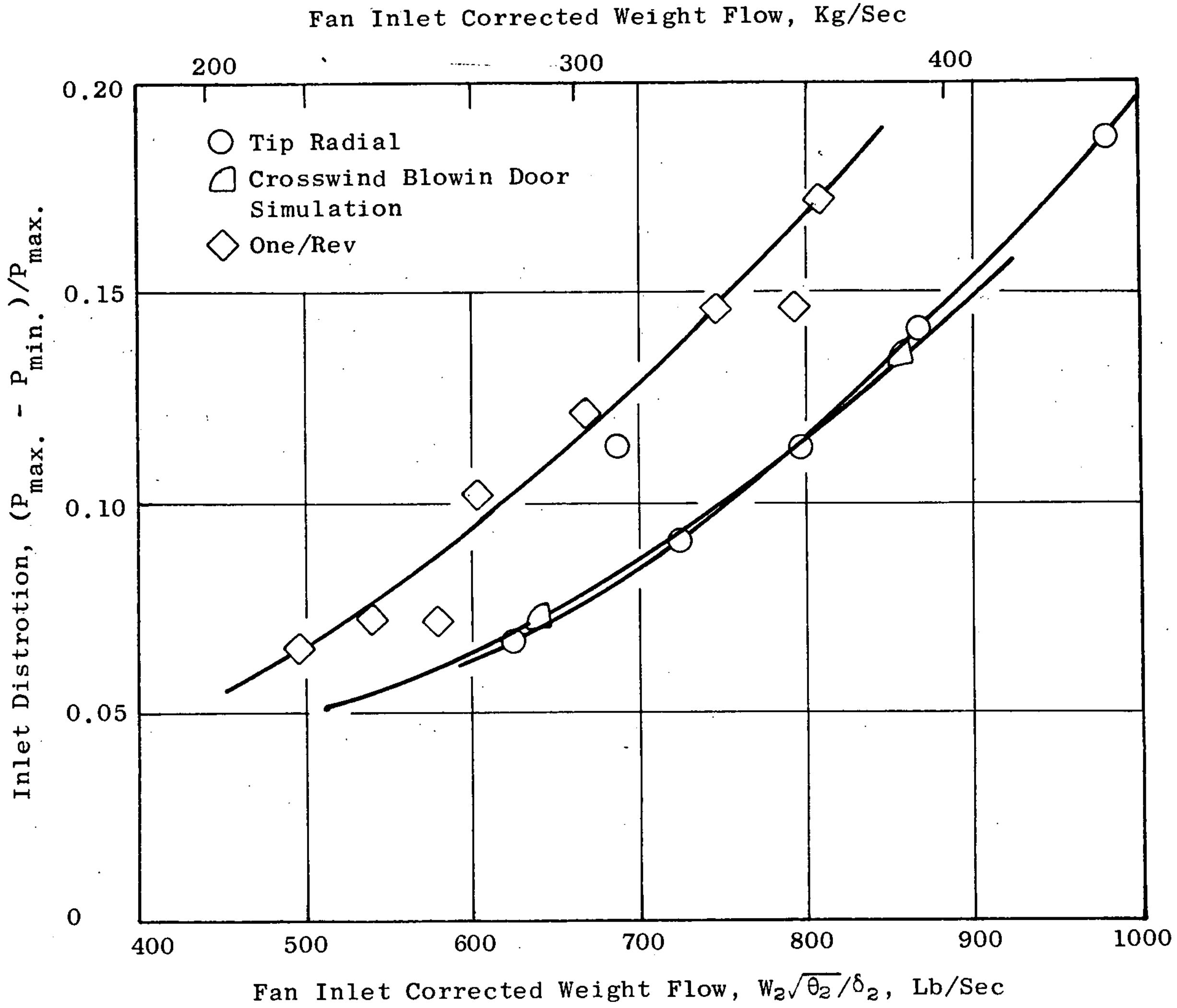

Figure 41. Inlet Flow Distortion Level.

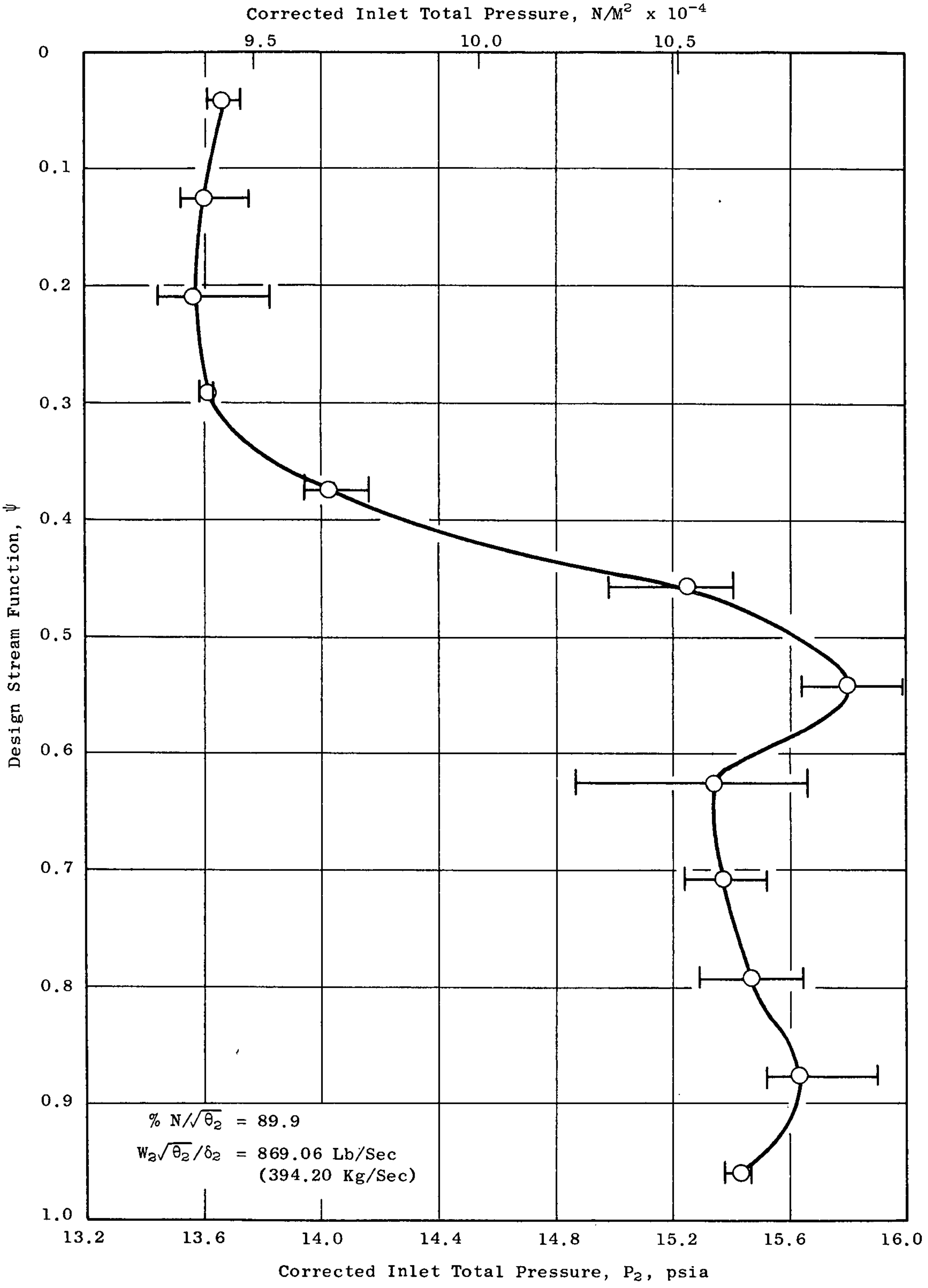

Figure 42. Tip Radial Distortion Inlet Pressure Profile.

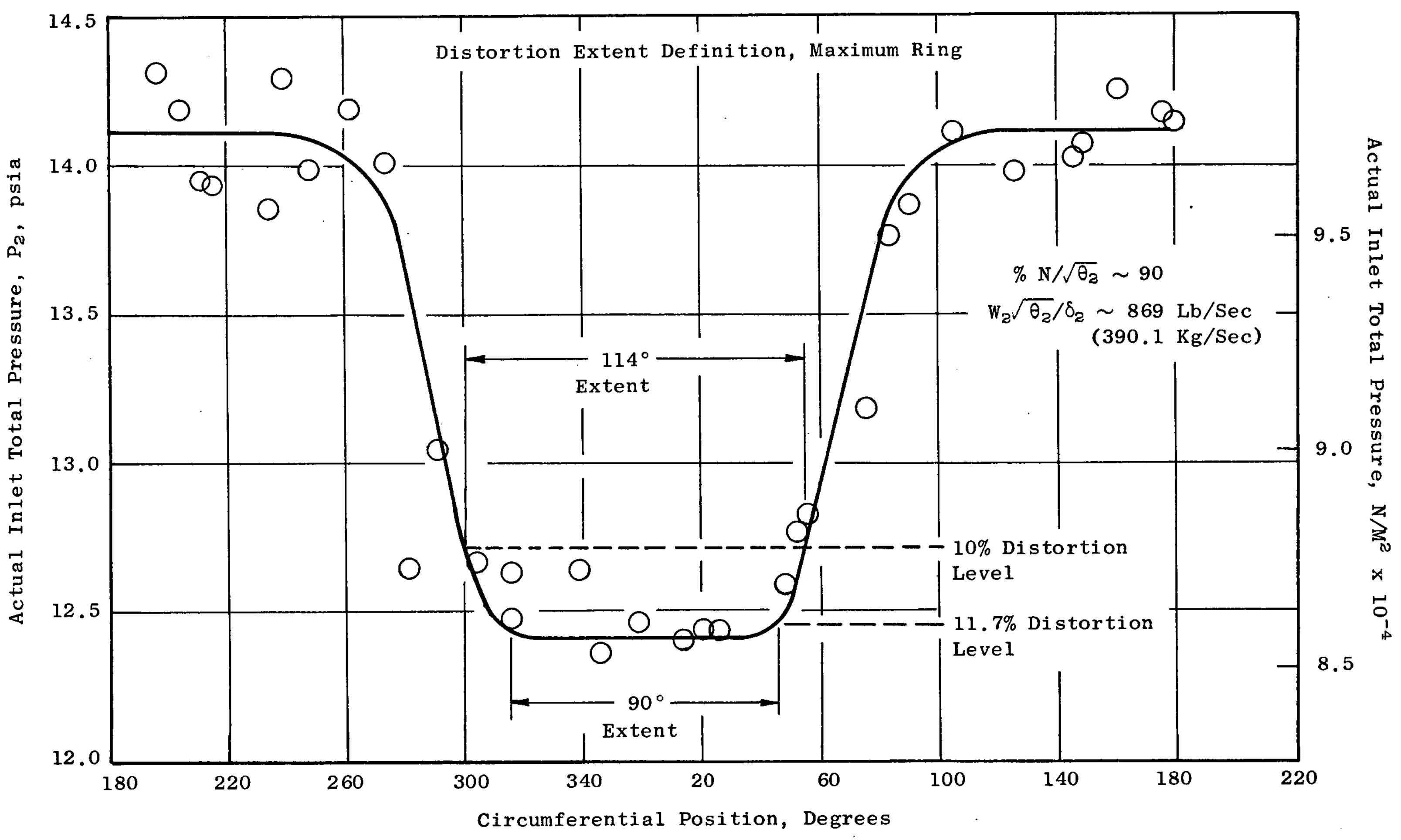

Figure 43. Crosswind Distortion Pattern.

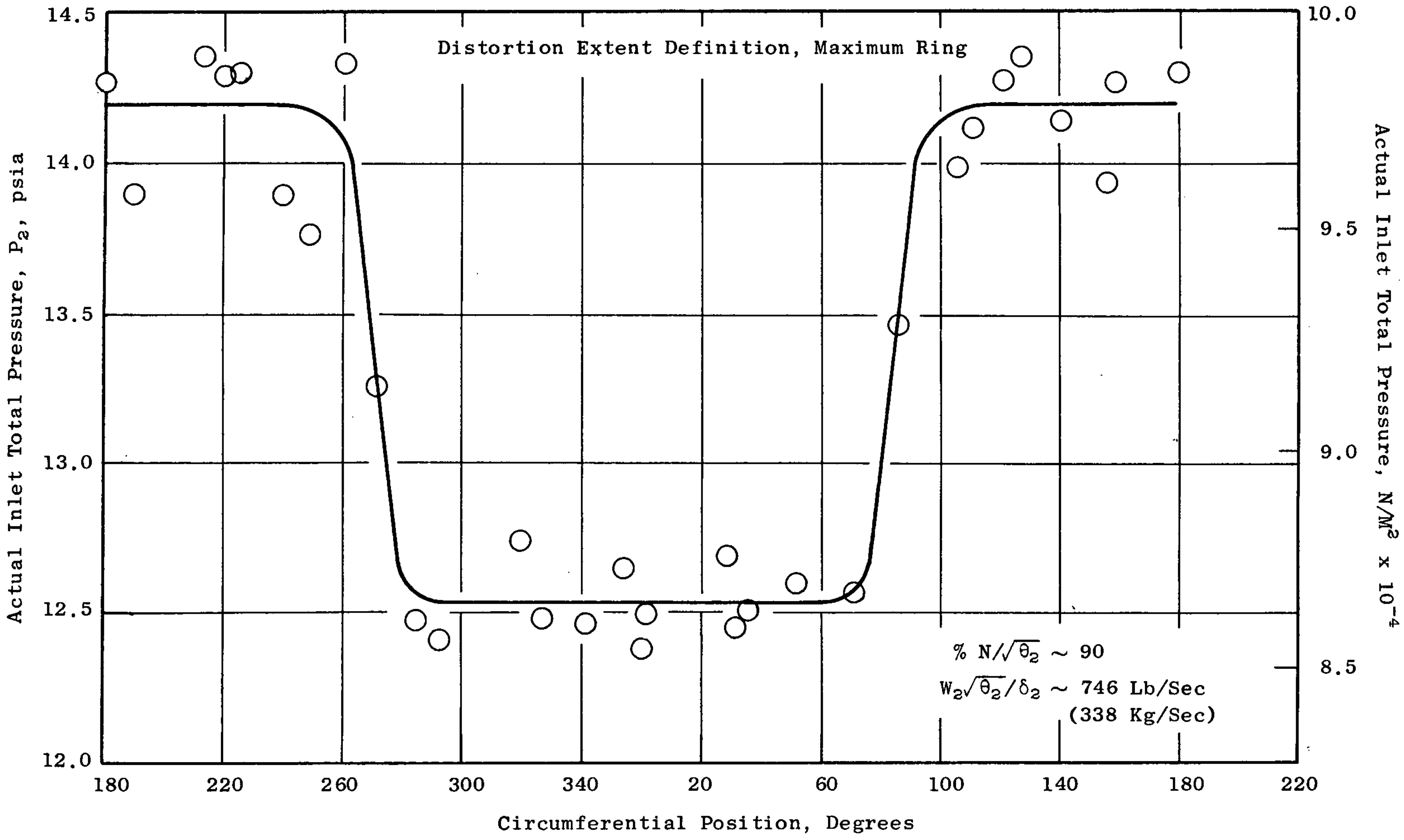

Figure 44. One/Rev Distortion Pattern.

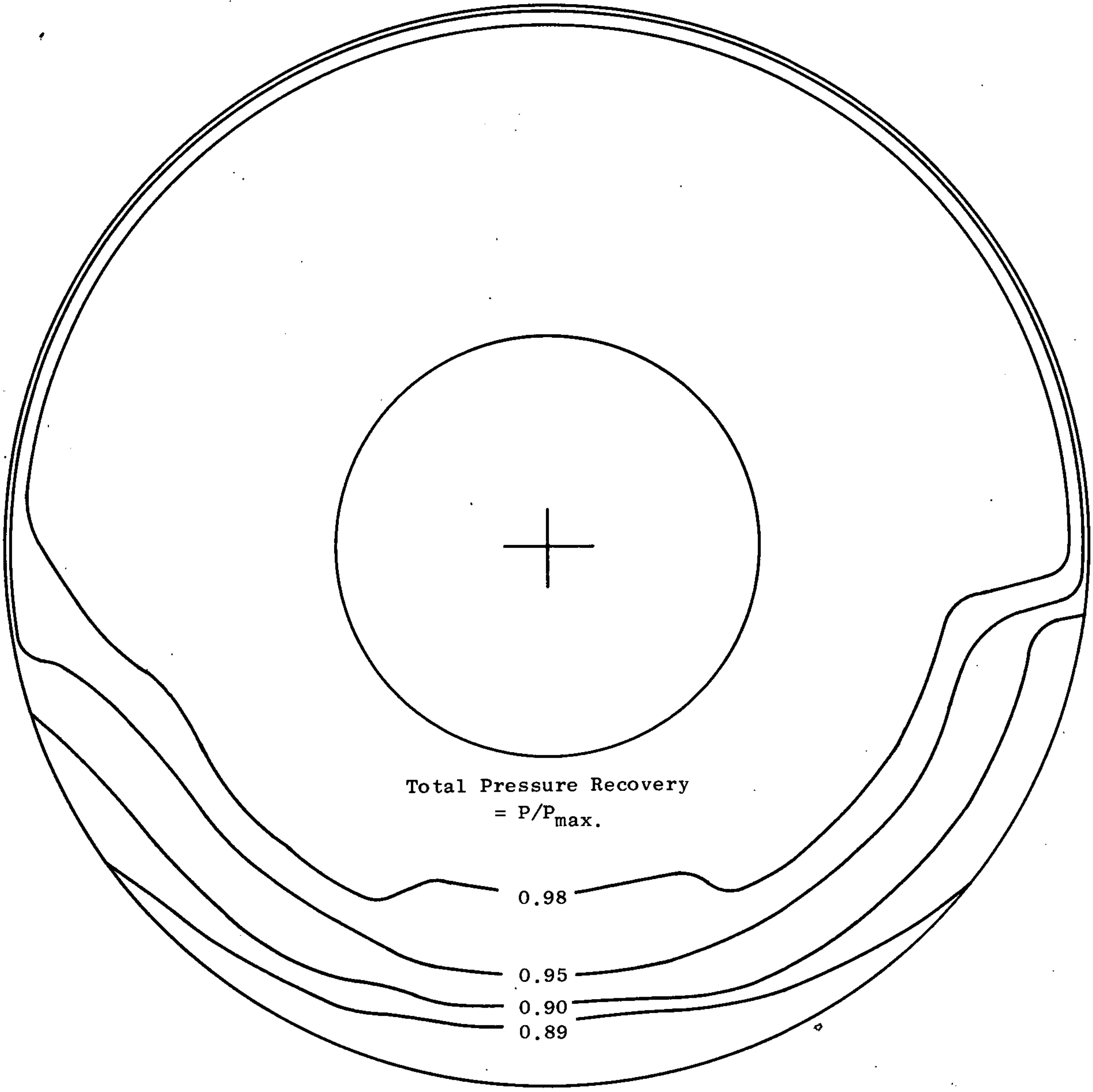

Figure 45. Inlet Pressure Recovery Contour, Crosswind Distortion.

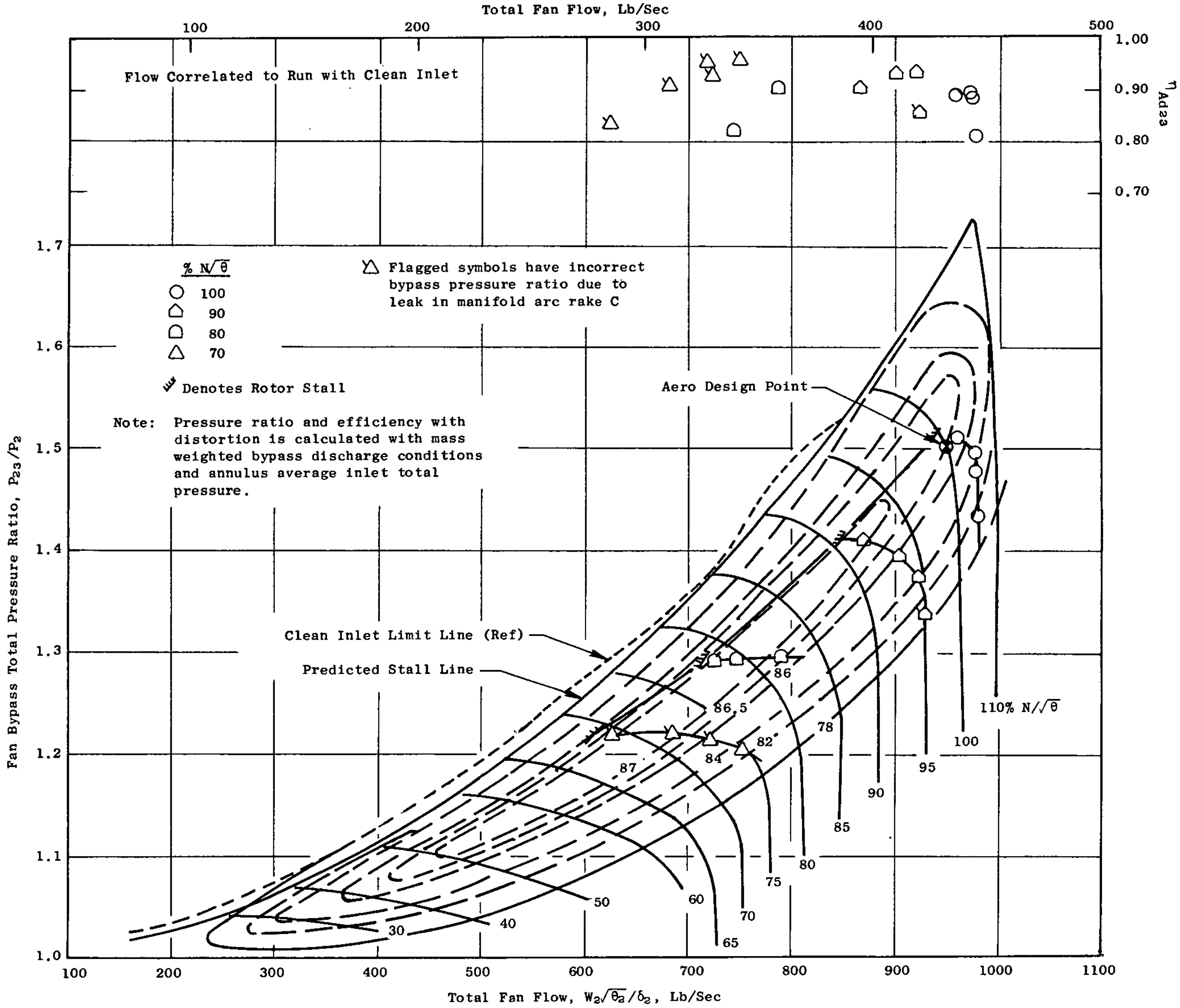

Note: Pressure ratio and efficiency with distortion is calculated with mass weighted bypass discharge conditions and annulus average inlet total pressure.

Figure 46. Fan A Performance Map, Tip Radial Distortion.

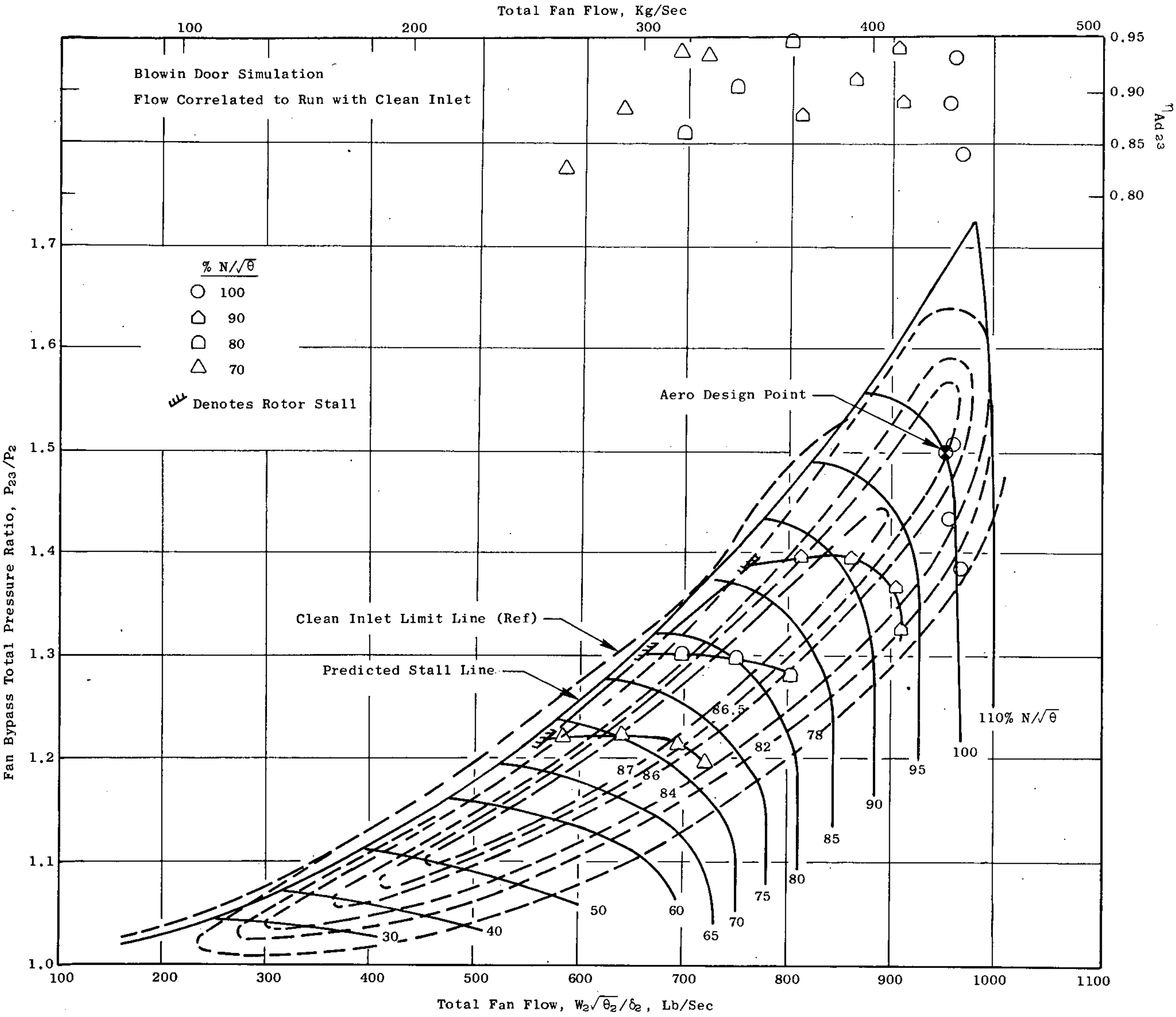

Figure 47. Fan A Performance Map, Crosswind Distortion.

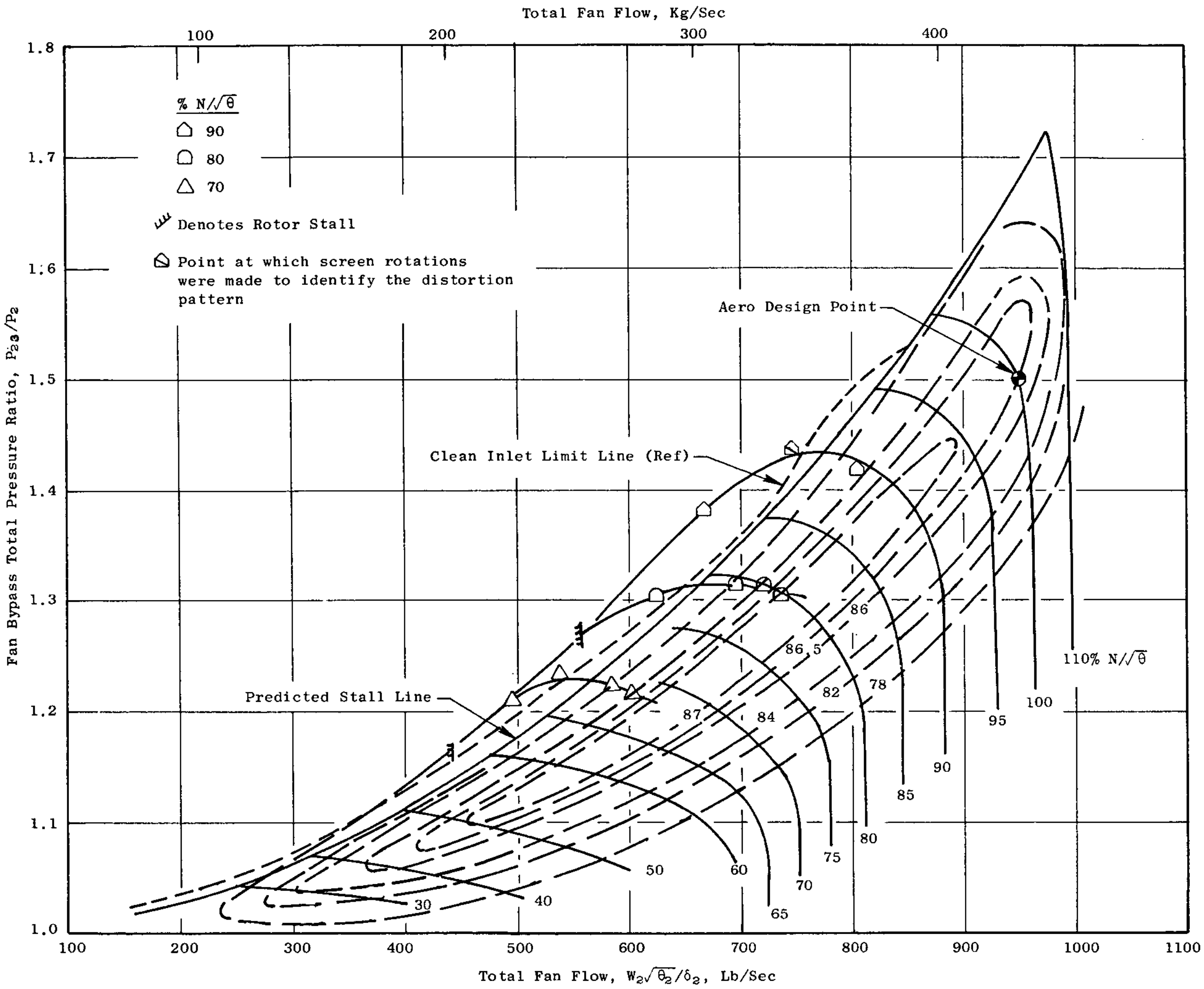

Figure 48. Fan A Performance Map, One/Rev Distortion.

## 6.0 SUMMARY OF RESULTS

The aerodynamic component test results of Fan A, one of two high-bypass-ratio, 1160 feet per second (353.6 m/sec) single-stage fans, which was designed to deliver a bypass pressure ratio of 1.50 with an adiabatic efficiency of 86.5% at a total fan flow of 950 lb/sec (430.9 kg/sec) yielded the following principal results:

1. With undistorted inlet flow, a bypass pressure ratio of 1.52 and an adiabatic efficiency of 88.3% at a total fan flow of 962 lb/sec (436.4 kg/sec) were actually achieved at design speed. The peak adiabatic efficiency at design speed was 88.5% at a bypass portion pressure ratio of 1.505 and a total fan flow of 970 lbs/sec (440.0 kg/sec). The operating margin achieved at design speed was 12.4% above the design point and was 10.8% at 90% speed. However, with the selected engine fan nozzle, the design speed altitude cruise operating margin is 17.2% and the sea level static operating margin is 16.0%, occurring at 90% speed. At 110% corrected speed, a total fan flow of 1010 lb/sec (458.1 kg/sec) was achieved which gave a specific flow of 43.9 lb/sec/ft$^2$ (209.4 kg/sec/m$^2$) of annulus area. A fan core pressure ratio of 1.356 at an adiabatic efficiency of 83.3% was achieved at 100% corrected speed and the design flow of 144.0 lb/sec (65.3 kg/sec).

2. The fan was tested with tip radial, crosswind, and one-per-rev screen-generated inlet distortion patterns. The distortion magnitude was about 15% at 90% speed, which is near the take-off condition. The tip radial pattern caused the stall line to be lowered by an amount equivalent to a loss in operating margin of 9%, and the crosswind pattern caused a 4% loss. With the one-per-rev pattern, the stall line was apparently raised, equivalent to a 4% gain in operating margin. All or part of this apparent gain may be a result of the data sampling or averaging methods employed.

# REFERENCES

1. Experimental Quiet Engine Program, Contract No. NAS3-12430, Phase 1 Engine Design Report, Volume 1, Section 4.0 Fan Aerodynamic Design, NASA CR-72967, March 15, 1970

2. Giffin, R.G., Parker, D.E. and Dunbar, L.W.: Experimental Quiet Engine Program Aerodynamic Performance of Fan B, NASA CR-72993, December, 1971.

3. Seyler, D.R. and Gostelow, J.P.: "Single Stage Experimental Evaluation of High Mach Number Compressor Rotor Blading, Part 2 - Performance of Rotor 1B," NASA CR-54582, Sept. 22, 1967.

# APPENDIX I

## INSTRUMENTATION

An overall meridional view of the test vehicle with the test instrumentation superimposed is shown in Figure 49. The fan inlet conditons were measured by four six-element pitot-static rakes located in the cylindrical section of the inlet duct between the bellmouth and the fan inlet. Twenty-four thermocouples attached to the inlet FOD screens were used for determination of inlet total temperature. The pressure and temperature sensors were located approximately on centers of equal area. The fan discharge total temperature and total pressure were measured by arc rakes. Seven arc rakes were located behind the fan bypass OGV's, and five arc rakes were located behind the fan core OGV's. Radially, the arc rakes were located on centers of equal design mass flow of the bypass portion and fan core portion, respectively.

The bypass portion arc rakes were composed of 12 elements with each element containing one temperature and one pressure sensor. This construction technique enables pressure and temperature sampling from a common fluid region and minimizes the effects of spatial variation in computing efficiency. The arc rakes spanned two OGV spacings. The five core portion arc rakes were of similar construction to that of the bypass portion arc rakes but with seven elements each containing one total pressure and total temperature sensor. These rakes also spanned two OGV spacings.

The rotor discharge total pressure in the fan core portion was measured by three five-element radial rakes. The radial positioning of the elements were on centers of equal design flow. The total pressure at discharge from the transition duct leading to the core compressor was measured by five five-element radial rakes with the elements being located on centers of equal area. (These rakes are identical with those used for core compressor inlet instrumentation on the TF39/CF6 engines.)

In addition to this instrumentation there were wall static pressures located in the inlet duct and along the outer casing, along the inside diameter of the bypass portion, around the splitter leading edge, and throughout the ducting for the fan core portion flow. Total pressure profile rakes were located on the inlet duct outer casing just forward of the fan rotor and on the inside diameter of the bypass portion midway between rotor exit and outer OGV inlet. The total number of pressure sensing elements exceeded the recording capability of the test stand. Three alternate pressure matrices were employed to record those pressures judged most useful for the particular test configuration objectives. Traversing probes were located at fan rotor inlet (a cobra and a wedge static), fan rotor exit (a cobra, a disk static, and a high response Kulite transducer), outer OGV inlet (a cobra), and inner OGV inlet (a cobra). The traverse probes were used only at selected operating points near the aerodynamic design point.

FOLDOUT FRAME 1

FOLDOUT FRAME 2

PRECEDING PAGE BLANK NOT FILMED

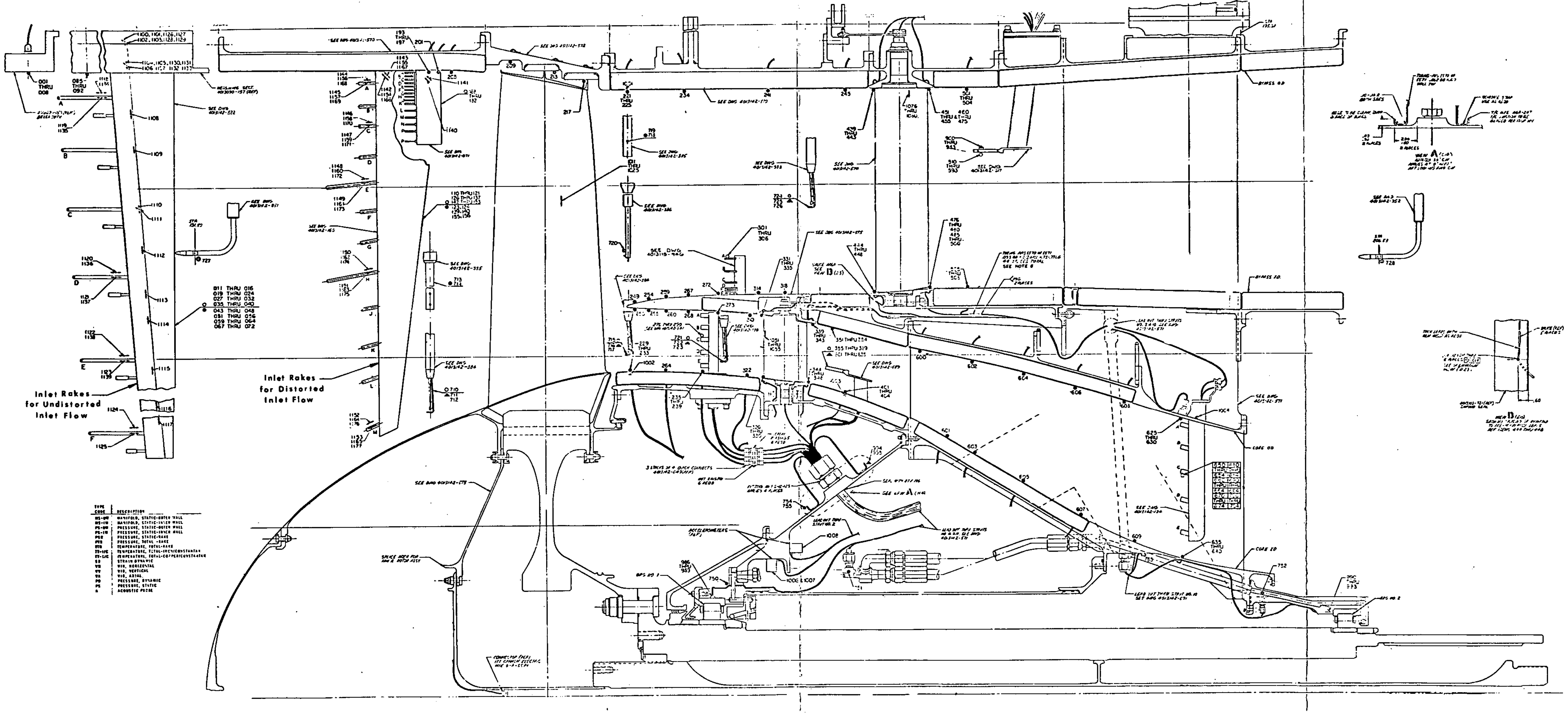

Figure 49. Fan A Test Vehicle Instrumentation Location.

PRECEDING PAGE BLANK NOT FILMED

For the distortion testing, the fan inlet total pressure was measured by three 12-element radial rakes located just upstream of the fan rotor. The elements were positioned radially so as to be on centers of equal design flow.

PRECEDING PAGE BLANK NOT FILMED

## APPENDIX II
## COMPUTATION OF OVERALL FAN PERFORMANCE

The total fan flow was computed from the inlet total and static pressure, the inlet screen total temperature, a measured area, and an assumed flow coefficient of 0.992. Figure 50 is a plot of the normalized outer casing velocity profile forward of the fan face as deduced from the wall static pressure and the total pressure profile rake. (This figure is the same as Figure 49 in reference 2. Since the inlet system for the Fan A testing was the same hardware employed in the testing of Reference 2, no differences would be expected.) The results are presented for four typical flow rates. A computation of the displacement thickness from the boundary layer profile yields an equivalent effective area coefficient of 0.994. The total temperatures and total pressures were recorded individually and arithmetically averaged. Generally, the static pressures were manifolded with only the single manifold value being recorded. However, the first instrumentation matrix recorded the individual static pressures from one of the inlet rakes as a check on the radial pressure profile. The inlet total and static pressure profiles for a typical high flow point are presented in Figure 51. The static pressure profile is nearly constant radially, as expected. The total pressure profile is slightly skewed towards the outside diameter, however; this skew is typical of all data points. It is believed that the closeness of the inlet bellmouth to the facility protection screen is responsible for the skew since the potential flow field in front of the bellmouth will have its highest velocity along the centerline, and, hence, this location will yield the largest screen pressure drop. The fan core flow was measured by a calibrated flow meter located in the facility discharge piping. The bypass flow is obtained by subtracting the fan core flow from the total fan flow; no independent measurement of the fan bypass flow was made.

The fan face total temperature and total pressure was taken as the arithmetic average of the screen mounted total temperatures and pitot-static total pressures. At discharge, the fan bypass portion and fan core portion are treated separately. For each portion, the arithmetic averages of the pressures and temperatures for each arc rake are computed. (The average excludes the last element on each rake, the 12th element on the fan bypass portion rakes, and the seventh element on the fan core portion rakes since this element is spaced one blade pitch from the first element and is, therefore, redundant for performance computation. This last element was incorporated to provide a check on the periodicity of the flow leaving the OGV's.) A linear variation in static pressure between wall measured values at the outside diameter and inside diameter was assumed. The averaged total temperature reading at each immersion is corrected for static wire (the error encountered in measuring an oil bath temperature) and Mach number at the Mach number and temperature of that immersion. The procedure then mass weights, radially, the actual enthalpy to obtain an average discharge total temperature and the ideal enthalpy rise to obtain an average discharge total pressure; Reference 3 presents the calculation procedure in detail. With the average pressure ratio and temperature rise of fan bypass portion and fan core portion, the actual air properties, including the effects of humidity, are used to compute the efficiency of the two streams.

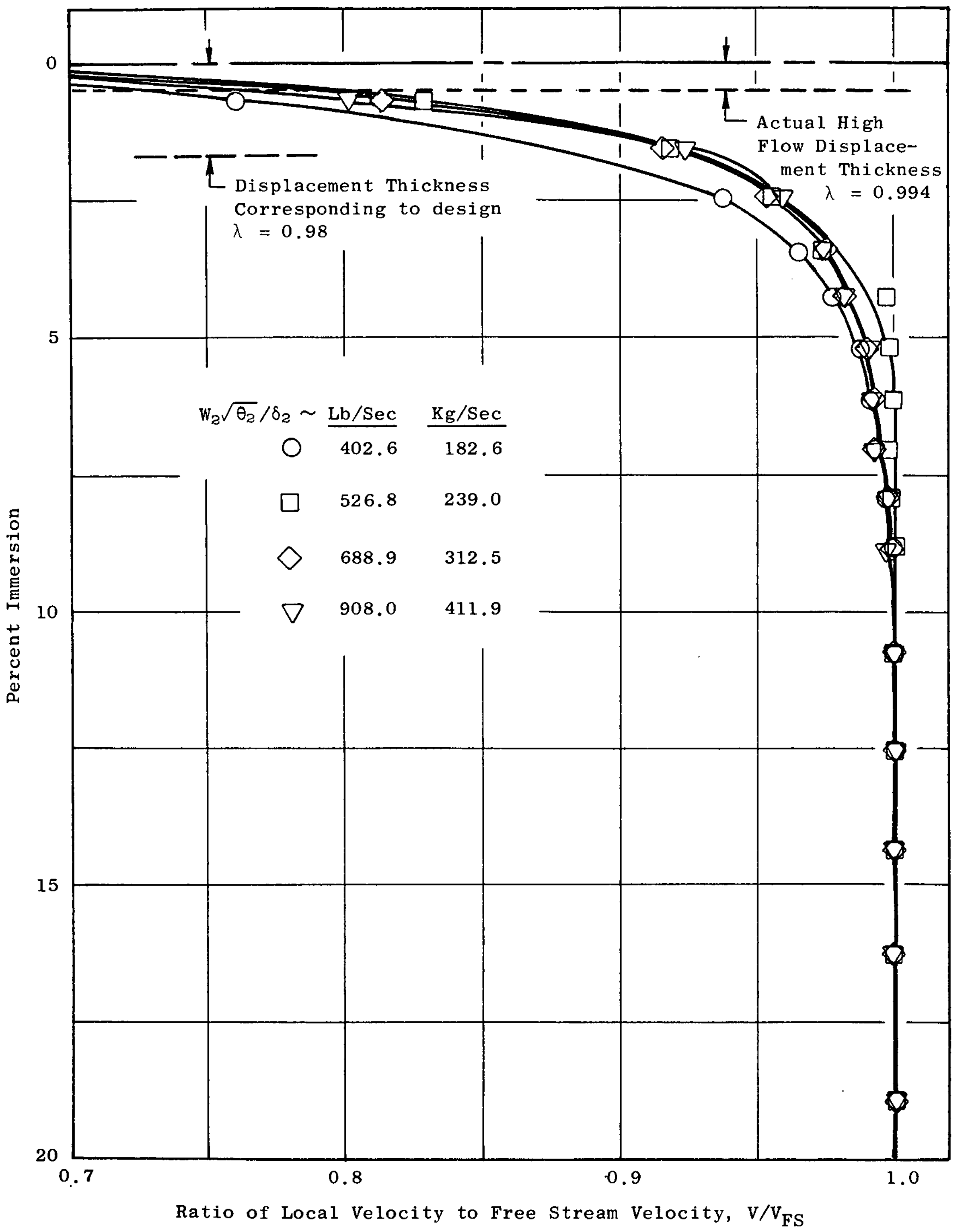

Figure 50. Inlet Boundary Layer Description.

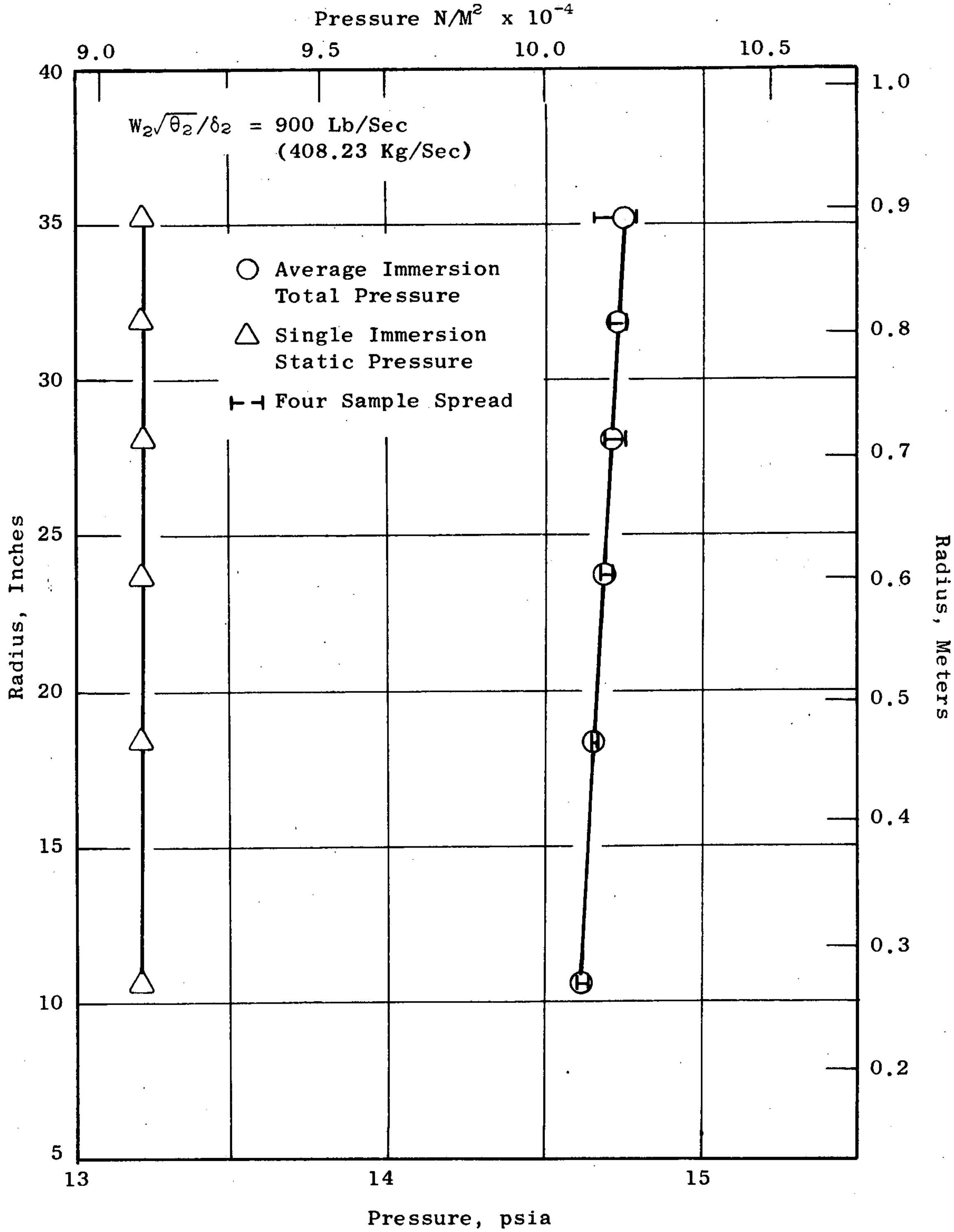

Figure 51. Typical Inlet Duct Pressure Profiles.

A computation was performed to determine the radial variation of stage and rotor only adiabatic efficiency and OGV total-pressure-loss and static-pressure-rise coefficients. A constant ratio of specific heats is used in these computations. The calculations assume the arithmetically averaged wake rake total pressure and total temperatures at OGV discharge. No change in total temperature is permitted through the OGV. For the bypass portion, the average of the three highest total-pressure-wake-rake elements is assumed to be the pressure in front of the OGV. In the fan core portion, the elements at each radius on the three radial rakes at rotor exit were averaged circumferentially to determine the OGV inlet total pressures. At inlet and discharge, the stream static is obtained by linear interpolation between wall values.

Since data from the traverse probes are generally considered to be less reliable than that from fixed instrumentation, traverse probe data is viewed as giving only an indication of trends and is not used in performance calculations.

## DATA ACCURACY

### Pressure

The recording system for pressure uses a method whereby each transducer (which measures up to 10 vehicle pressures) is calibrated on each reading against a CEC electromanometer which in turn is calibrated before and after each test against a dead-weight tester which can be traced to the National Bureau of Standards. This procedure results in an overall accuracy of pressure measurements of ± 0.25% of level

### Temperature

The recording system used for temperatures has a readability of one microvolt and is periodically calibrated against a standard which is traceable to the National Bureau of Standards giving an overall accuracy of recording of ± 3 microvolts or approximately ± 0.12° F.

In addition, static wire and dynamic recovery ratio calibrations are performed on all sensors used for performance measurements. It is estimated that the overall RMS temperature measurement accuracy is ± 0.5° for CC wire and ± 0.75° for CA wire.

### Flow

There is no error in the total pressure sensed by the inlet pitot-static instrument. The static pressure sensed by the inlet pitot-static instrument has, under ideal conditions, an estimated error of 0.35% of the dynamic pressure. However, because of minute differences in probe-to-probe manufacture and or alignment, a sensing error of 1% of the dynamic pressure can be expected.

The data acquisition accuracy (or more appropriately inaccuracy) are the extremes expected for the individual element measurements. Since some elements read high while other elements read low it is more reasonably expected that the overall performance inaccuracies are on the order of one-fourth of the inaccuracies of the individual elements. The problem of data sampling is at least as important in overall performance accuracy as the ability to properly sense and record the data. A treatment of this problem is beyond the scope of the current report.

PRECEDING PAGE BLANK NOT FILMED

# APPENDIX III

# AEROMECHANICAL CHARACTERISTICS OF THE NASA QUIET ENGINE FAN "A" FSFT VEHICLE

By

J.E. Baker

## I. INTRODUCTION

This report is devoted to the aeromechanical aspects of the NASA Quiet Engine Fan "A" FSFT vehicle test program which was conducted at the Lynn Component Test Facility from November 23, 1970 to December 29, 1970. Information on scope limits is also included in order to complete the aeromechanical picture.

The investigation included performance mapping in the 30 to 110% corrected speed range with clean inlet, and in the 70 to 100% corrected speed range with three inlet distortion screen patterns* designed to have a magnitude of about 0.15 at 90% speed **. The three patterns were; tip radial, simulated crosswind, and 1/rev.

By the way of background, terminology which may not be of common understanding, and/or is peculiar to the General Electric Company, is defined below:

| | |
|---|---|
| Aeromechanics | The technical discipline that considers the interaction of the aerodynamic environment with the elastic and mechanical properties of a turbomachine component, such as rotor blades or stator vanes. |
| Vibration Mode | Identification of a variety of ways in which a structure can vibrate, each of which has its own natural frequency. Examples in blading are:<br>• First flex (1F): Vibration normal to the least-moment axis with a node (zero motion) only at the fixed end(s) of the blade.<br>• Second flex (2F): same as first flex except there are two nodes, one at the fixed end(s) and another at some point on the blade airfoil away from the ends.<br>• First torsion (1T): vibration having a twisting motion with a node running radially along the blade near its midchord location. |

---

* Testing at 100% speed with 1/Rev distortion was aborted by excessive fan bypass OGV vibratory stress (see text).

** $\Delta P/P = \frac{P_{Tmax} - P_{Tmin}}{P_{Tmax}}$

- System mode: one in which vibratory coupling occurs between blades as well as between the blades and the disc. The disc involvement involves radial nodes which are called nodal diameters. The disc involvement generally induces lower system mode frequencies than for the corresponding blade modes; and, like blade resonances, system mode resonances to excitations fixed in space (distortion, struts, etc.) can occur when the number of nodal diameters coincides with corresponding integral orders. See Chapter VI of Den Hartog, Mechanical Vibrations for more details.

| | |
|---|---|
| Integral-Order Resonance | This type of blade vibration exists when a natural frequency corresponding to a "mode" of vibration is induced to respond at an integral multiple of rotor speed. These multiples are referred to as "orders" or "per-revs". Such resonances can occur when a blade natural frequency crosses each per-rev. |
| Separated Flow Vibration | This type of blade vibration involves the random amplitude response of the blading to turbulent excitation, either from separated flow on the blade itself or from free-stream turbulence. It occurs in one, or more, of the normal blade vibration modes, those having the lowest frequencies usually being the most responsive. |
| Endurance Limit | Vibratory stress above which fatigue failure will occur in $10^7$ cycles, or less. |

## II CONCLUSIONS

Operation of the tip-shrouded Fan "A" component was demonstrated to be aeromechanically safe for engine use involving little (or no) inlet distortion up to 110% speed with nominal fan exhaust nozzle area ($A_{28}$ = 1790 $in^2$), and up to 105% speed with small (1700 $in^2$ and large (1980 $in^2$) nozzles. Validation of this conclusion is supported by the following maximum response levels of the blading:

| | | Maximum Scope Limit, % | | |
|---|---|---|---|---|
| $A_{28}$(In.$^2$) | Maximum Speed, % | Rotor Blades | Bypass OGV's | Core OGV's |
| 1700 | 105 | 70 | 40 | 16 |
| 1790 | 110 | 60 | 44 | 16 |
| 1980 | 105 | 45 | 30 | 16 |

---

The quantitative interpretation of aeromechanical response to inlet distortion requires the acquisition of such data in the presence of "real" distortions produced by ambient crosswinds. Peebles testing did not include operation during appreciable magnitudes of ambient crosswind. (Note: Turbulent excitation of fan OGV's with artificially produced distortion during the FSFT program induced excessive magnitudes of vibratory stress.

The cause of the unusual rotor tip shroud separated flow vibration is nonapparent, but may be associated with three-dimensional flow in this region due to leakage around the shroud.

Stall-induced blade vibration was not unduly severe, and loss of blading fatigue life due to the overstresses encountered is negligible.

Moderate variation of bypass OGV angle (± 4°) was found to have negligible effect on blade/vane vibration.

Operation with high bypass ratios greatly increased bypass OGV separated flow vibration levels. The character of vibration suggests possible splitter lip flow separation as a major contributor.

## III SCOPE LIMITS

### A. GENERAL PROCEDURE

Only a limited number of so-called "engine" gage locations are utilized in monitoring the vibration characteristics of the blading in a given stage. Accordingly, it is necessary to ascertain the limiting vibratory stress (scope limit), as seen by each "engine" gage/location, for all pertinent modes of blade vibration. For this purpose, the following relation is used:

$$\sigma_{scope} = \frac{2\sigma_e(\sigma_g/\sigma_{cp})}{K_v K_e K_c}$$

where $\sigma_{scope}$ = scope limit, Kpsi-da*

$\sigma_e$ = endurance limit, corresponding to the steady stress, at the critical point (defined below), taken from the Goodman diagram for the proper blading material and temperature (must include three sigma reduction of average endurance limit to represent minimum material properties).

$\sigma_g/\sigma_{cp}$ = ratio of vibratory stress indicated by the "engine" gage to that at the critical point for the vibration mode under consideration.

$K_v$ = blade-to-blade response variation during vehicle operation (1.3 is normally used).

$K_e$ = electronics variation allowance (1.05 is normally used).

$K_c$ = concentration factor at the critical point (varies with local geometry.

Critical Point = Point on the blade at which initial fatigue cracks would be incurred for the vibration mode in question. Selection of the critical point for scope limit calculations is defined by the following equation:

$$\frac{K_{cL}(\sigma_{vL}/\sigma_{v\ max})}{\sigma_{eL}/\sigma_{e\ max}} = \text{Maximum}$$

where, $K_{cL}$ = concentration factor at location being considered on the blade.

---

*"da" is double amplitude, also referred to as peak-to-peak amplitude.

$\sigma_{vL}/\sigma_{max}$ = ratio of the local vibratory stress to that at the maximum vibratory stress point on the blade in the vibration mode under consideration.

$\sigma_{eL}$ = endurance limit at the location being considered on the blade, for the steady-state stress existing at that location, using the applicable Goodman diagram.

$\sigma_{e\ max}$ = endurance limit at the location of maximum vibratory stress on the blade for the vibration mode under consideration, using the applicable Goodman diagram.

Identification of the critical point, as well as the scope limit itself, therefore, requires a knowledge of the steady stress distribution over the entire blade/vane structure at the applicable operating conditions. Steady stress calculations utilize the General Electric "Twisted Blade" and MASS computer programs, and, for complex geometries in the vicinity of the built-in end(s) of the airfoil*, stress levels are modified by the introduction of "end-effects" corrections. These corrections involve, first, the acquisition of measured local steady stresses throughout the critical airfoil root (and shroud, for shrouded blades) area for known magnitudes of torsional moment, radial pull (rotor blades), and bending moment about both the tangential and axial planes. By multiplying these values of local stress per unit load (or moment) by the corresponding computed load and moments present at the airfoil root, much more accurate steady stresses are obtained in these regions.

The process of defining vibratory stress distributions for use in the derivation of scope limits is discussed separately in the rotor and stator scope limit sections, which follow.

## B. ROTOR BLADE SCOPE LIMITS

### 1. Frequency and Vibratory Stress Distribution

The process of calculating frequencies and vibratory stress distributions for the Fan "A" rotor blades was complicated by the presence of a "flexible" tip shroud. In order to model the tip shroud, Twisted Blade computer calculations with various combinations of shroud "springs" were conducted to duplicate vibratory bench test frequencies with the shroud restrained at the contact surfaces. With this information as a basis, the first three shrouded blade modes were calculated, as well as shrouded blade-disc system modes for a variety of nodal diameter/blade mode combinations. Natural frequencies, as well as corresponding vibratory stress distributions, were thus obtained. Pertinent frequencies are shown in Figure 52. As with airfoil steady stresses in the vicinity of the shroud and blade root, bench test end-effects data were applied to computed results to provide correct vibratory stress distribution information in these portions of the airfoil as well as on the tip shroud itself.

---

*Geometries requiring end-effects correction include airfoils with high airfoil twist and/or camber gradient near the root, airfoil root skew, and nonrigid or nonuniform airfoil root support.

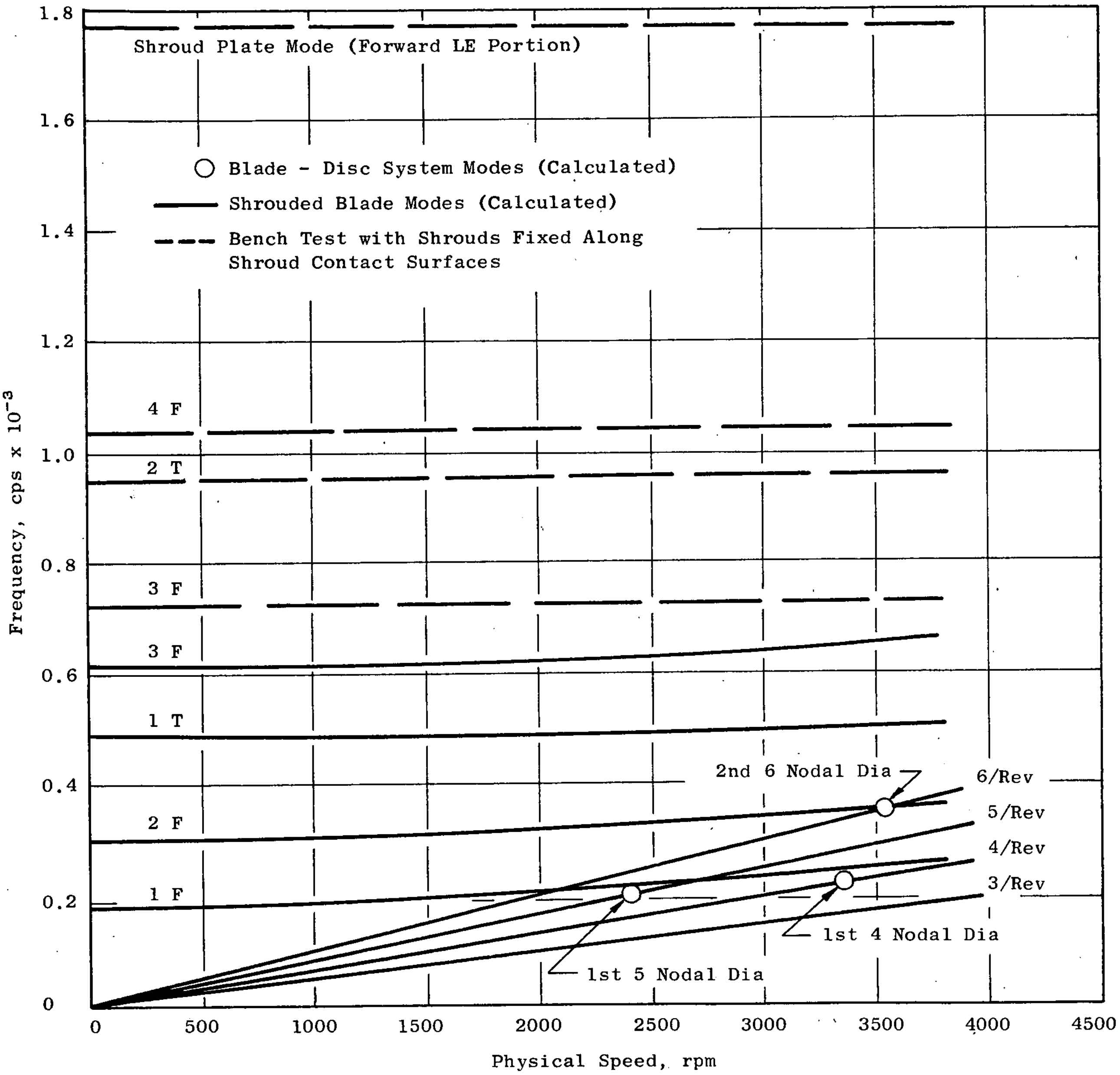

Figure 52. Campbell Diagram, Rotor Blades.

For the higher complex modes, calculation procedures are not reliable. Thus, bench test vibratory stress distribution data were used for these modes, natural frequencies being presented in Figure 52. This vibratory distribution information was obtained by applying a large number of small strain gages over stress in any mode of blade vibration. The relative strain readings were recorded for each gage while holding constant blade vibration amplitude in each mode.

### 2. Engine Gage Selection and Scope Limits

The critical point for most of the pertinent vibration modes fell at various locations on the tip shroud. Therefore, as shown in Figure 53, most of the engine gage locations are located on the shroud (gages 160, 162, 171, and 173). However, as a hedge against possible rapid attrition of these gages, two locations on the airfoil were selected (gages 3 and 46). Scope limits for these gages in each of the vibration modes of interest were calculated per the procedure described in Section IIIA, utilizing the Goodman diagram information shown in Figure 54. These scope limits are provided in Table I.

## C. STATOR VANE SCOPE LIMITS

### 1. Frequency and Vibratory Stress Distribution

In the absence of a centrifugal field, the vane natural frequencies, and associated vibratory stress distributions, for this vehicle are essentially unaffected by operating conditions. Although it is possible to compute vane natural frequencies with reasonable accuracy for these vanes having airfoil leading and trailing edges over-hanging the round vane base, it is acknowledged that bench test vibratory stress distribution data, using a large number of miniature strain gages applied to the vane, provides the most accurate information on which to base scope limits. For these vanes, which are held at one trunnion end, the other being inserted into a hole, the degree of restraint in the engine/vehicle environment is not known exactly. Thus, vibratory stress distribution bench testing was done with the trunnion on the vane-actuation end clamped tightly, but with each of three restraint conditions for the trunnion at the other end; fixed, free and restrained (inserted into a hole with a slightly loose fit). Natural frequencies for fan bypass and core OGV's are presented in Figures 55 and 56, respectively, for trunnion fixity conditions applicable to observed vane vibration frequencies during vehicle investigations.

### 2. Engine Gage Selection and Scope Limits

Study of the bench vibratory stress distribution data indicated that only one engine gage location on both the bypass and core OGV's was required to provide adequate sensitivity to all vibration modes which could be excited up to fan blade-passing per-rev excitation at top speed. These gage locations are shown in Figure 57. Scope limits were calculated at design speed conditions per the approach described in Section IIIA, utilizing the Goodman diagram information shown in Figure 58. These limits are inserted in Figures 55 and 56 opposite the plotted natural frequencies.

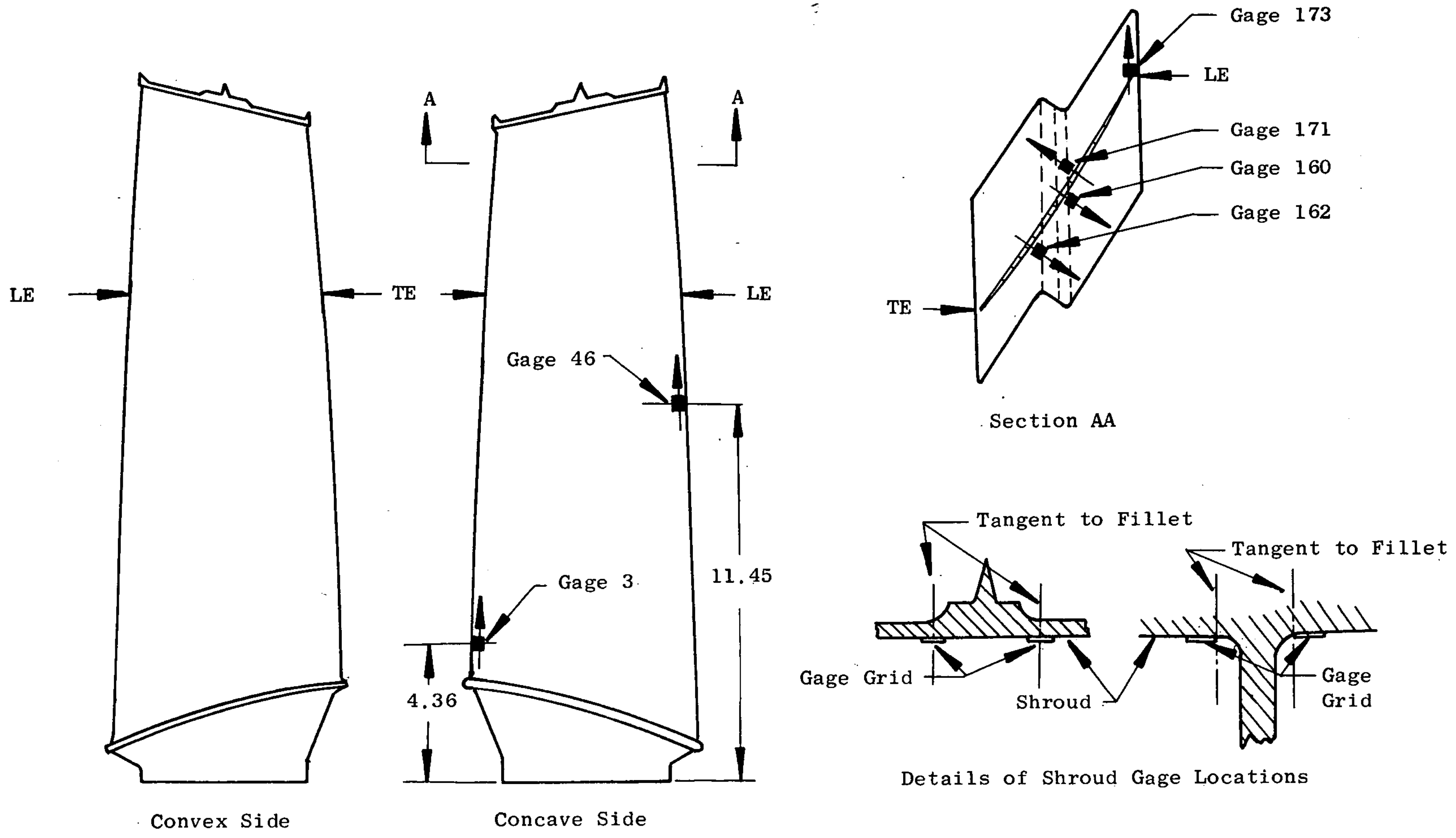

Figure 53. Rotor Blade Strain Gage Locations.

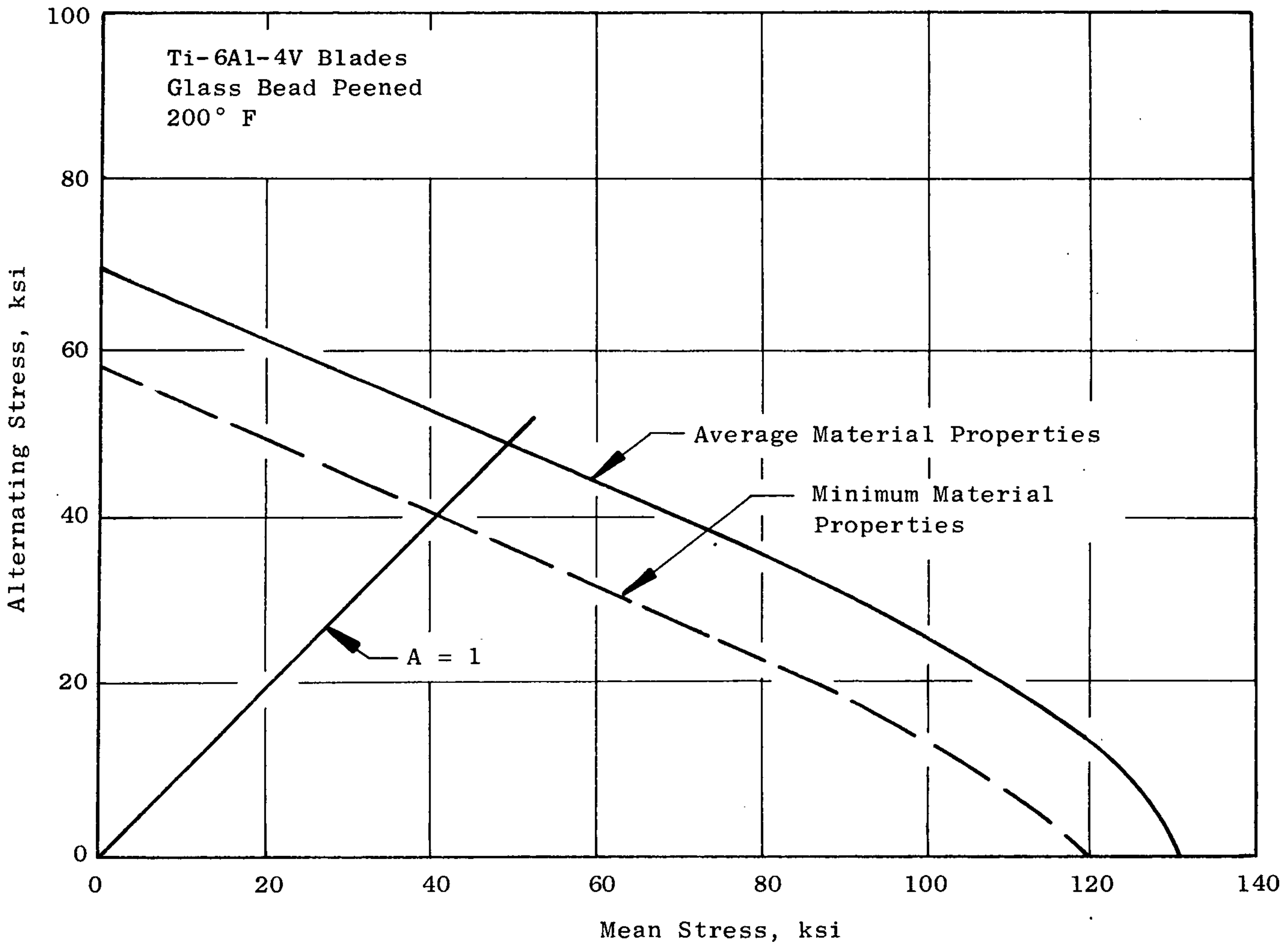

Figure 54. Goodman Diagram for Rotor Blade Scope Limit Calculations.

Table I. Rotor Blade Scope Limits.

| Gage Ident. | Calculated Shrouded Blade Modes | | | | Bench Test Modes: Shroud Restrained * | | | | Blade-Disc System Modes | | |
|---|---|---|---|---|---|---|---|---|---|---|---|
| | 1F | 2F | 1T | 3F | 3F | 2T | 4F | Shroud Plate Mode | 1st 5 Dia. | 1st 4 Dia. | 2nd 6 Dia. |
| | | | | | | 1800 RPM | | | | | |
| Frequency (cps) | 208 | 315 | 490 | 620 | 725 | 956 | 1042 | 1768 | Not applicable in this speed range (See Figure 52) | | |
| 3 | 3.5 | 34.0 | 32.2 | 28.4 | 22.0 | 11.0 | 1.3 | 0 | | | |
| 46 | 22.6 | 31.3 | 17.9 | 1.0 | 2.0 | 24.0 | 1.0 | 0 | | | |
| 160 | 5.6 | 11.5 | 20.6 | 14.0 | 1.6 | 0.6 | 1.0 | 0 | | | |
| 162 | 55.8 | 55.8 | 52.6 | 4.5 | 11.0 | 27.0 | 2.0 | 0 | | | |
| 171 | 29.0 | 46.4 | 53.6 | 33.7 | 35.0 | 15.0 | 3.0 | 0 | | | |
| 173 | 0.6 | 0.6 | 0.3 | 0 | 38.0 | 20.0 | 43.0 | 54.8 | | | |
| | | | | | | 2900 RPM | | | | | |
| Frequency (cps) | 230 | 335 | 501 | 635 | 727 | 957 | 1042 | 1768 | 238 | Not applicable in this speed range (See Figure 52) | |
| 3 | 5.1 | 31.6 | 28.4 | 25.1 | 22.0 | 11.0 | 1.3 | 0 | 16.0 | | |
| 46 | 17.2 | 27.0 | 12.5 | 1.0 | 2.0 | 24.0 | 1.0 | 0 | 25.4 | | |
| 160 | 5.1 | 9.5 | 17.4 | 12.4 | 1.6 | 0.6 | 1.0 | 0 | 8.9 | | |
| 162 | 50.0 | 50.0 | 41.6 | 4.0 | 11.0 | 27.0 | 2.0 | 0 | 59.6 | | |
| 171 | 26.0 | 38.8 | 48.8 | 29.9 | 35.0 | 15.0 | 3.0 | 0 | 37.7 | | |
| 173 | 0.6 | 0.6 | 0.3 | 0 | 38.0 | 20.0 | 43.0 | 47.6 | 0.6 | | |
| | | | | | | 3624 RPM | | | | | |
| Frequency (cps) | 252 | 358 | 514 | 663 | 727 | 957 | 1042 | 1768 | 302 | 240 | 362 |
| 3 | 6.6 | 29.0 | 25.0 | 22.3 | 22.0 | 11.0 | 1.3 | 0 | 11.7 | 3.8 | 7.6 |
| 46 | 11.8 | 23.0 | 7.2 | 1.0 | 2.0 | 24.0 | 1.0 | 0 | 18.7 | 13.9 | 22.0 |
| 160 | 4.6 | 7.5 | 14.0 | 10.6 | 1.6 | 0.6 | 1.0 | 0 | 6.5 | 6.6 | 1.7 |
| 162 | 44.0 | 44.0 | 31.0 | 3.4 | 11.0 | 27.0 | 2.0 | 0 | 44.0 | 44.0 | 26.0 |
| 171 | 23.0 | 30.0 | 42.0 | 26.3 | 35.0 | 15.0 | 3.0 | 0 | 28.0 | 28.0 | 3.4 |
| 173 | 0.6 | 0.6 | 0.3 | 0 | 38.0 | 20.0 | 43.0 | 40 | 0.6 | 0.6 | 0.5 |

* Shrouds Fixed Along Contact Surfaces

Trunnion End Restraint Terminology (See Figure 57)

| | Actuated End | Pivoted End |
|---|---|---|
| F-F | Fixed | Fixed |
| F-R | Fixed | Inserted into Close-Clearance Hole |

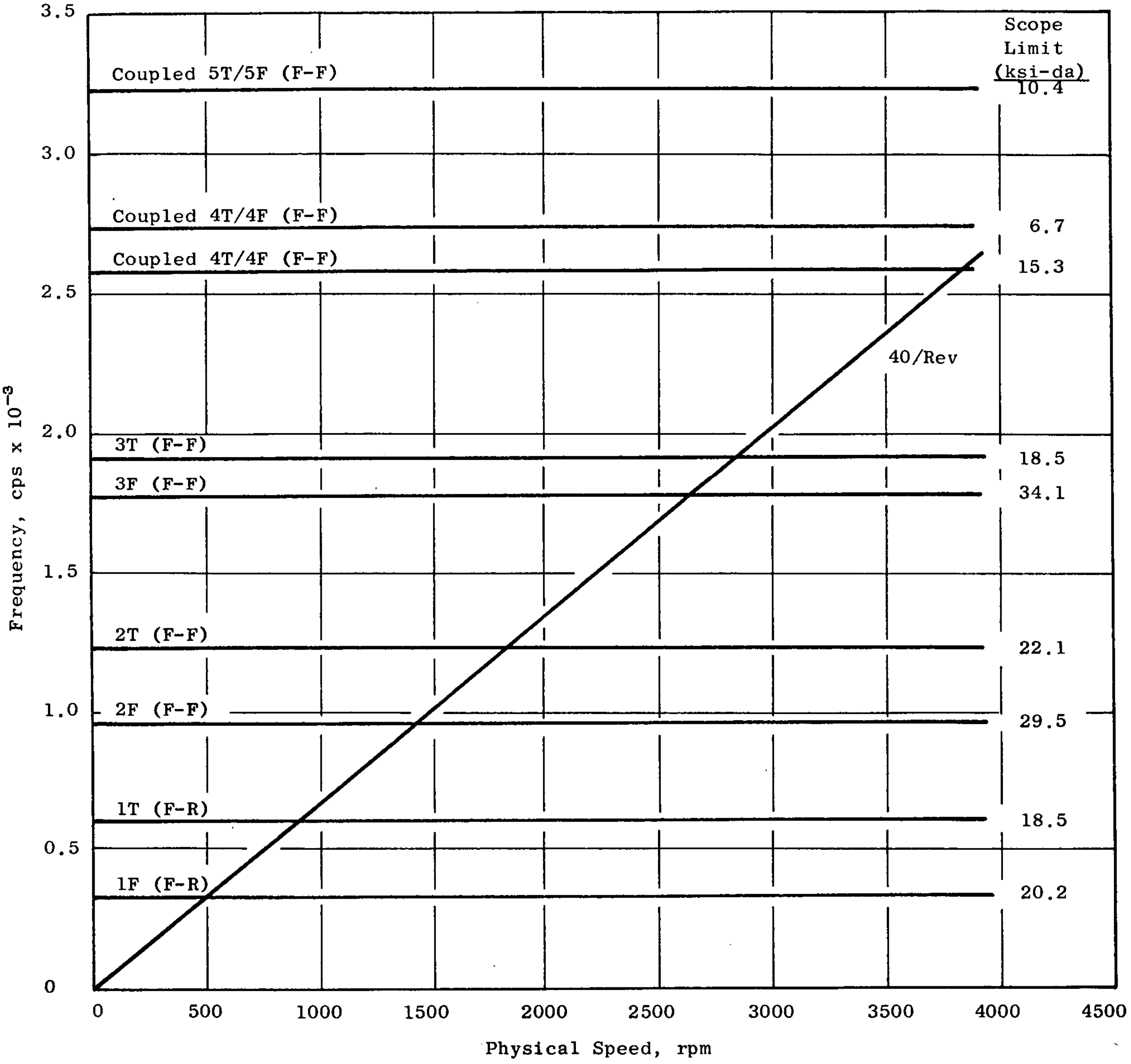

Figure 55. Campbell Diagram and Scope Limits, Bypass OGV.

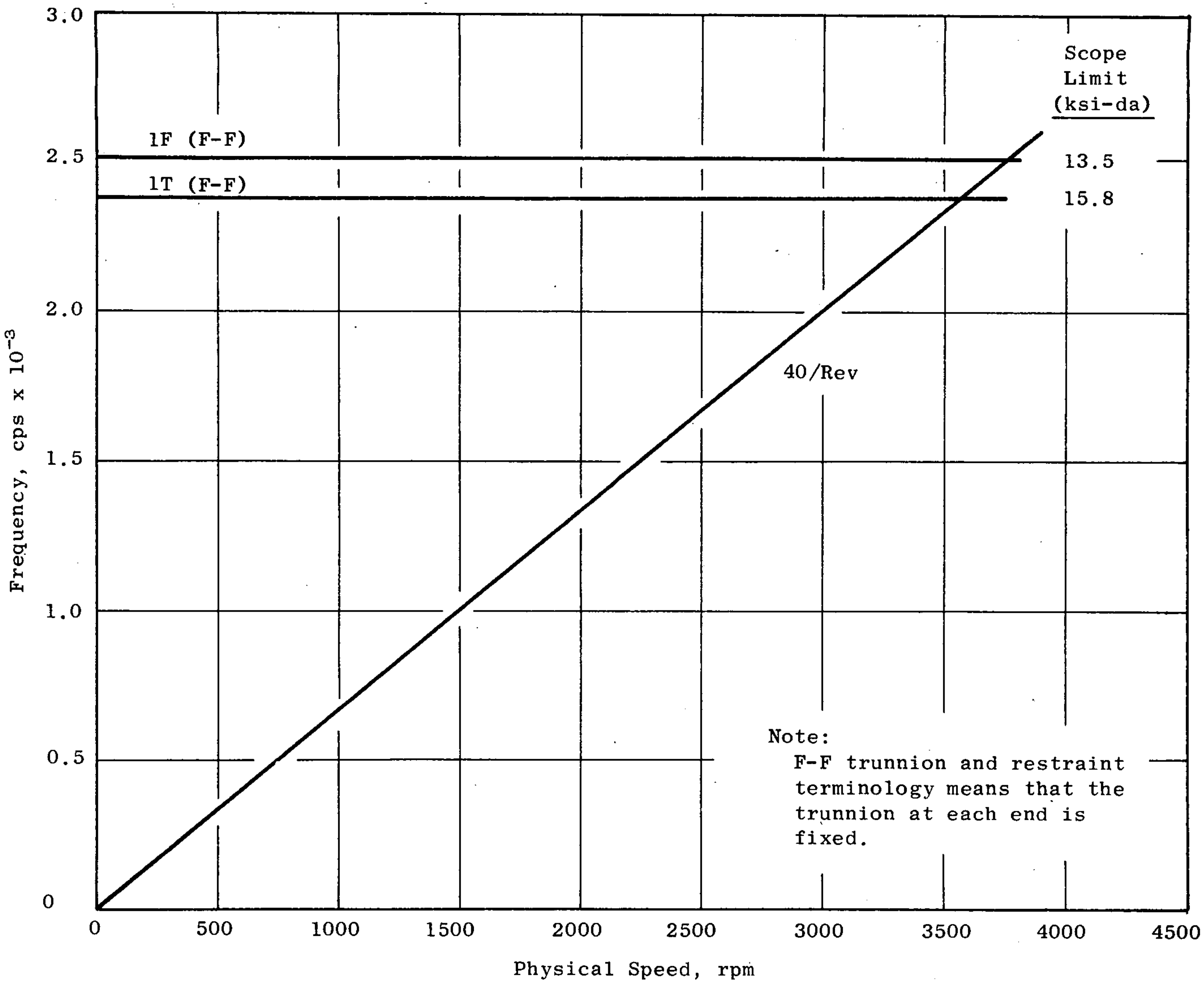

Note:
F-F trunnion and restraint terminology means that the trunnion at each end is fixed.

Figure 56. Campbell Diagram and Scope Limits, Core OGV.

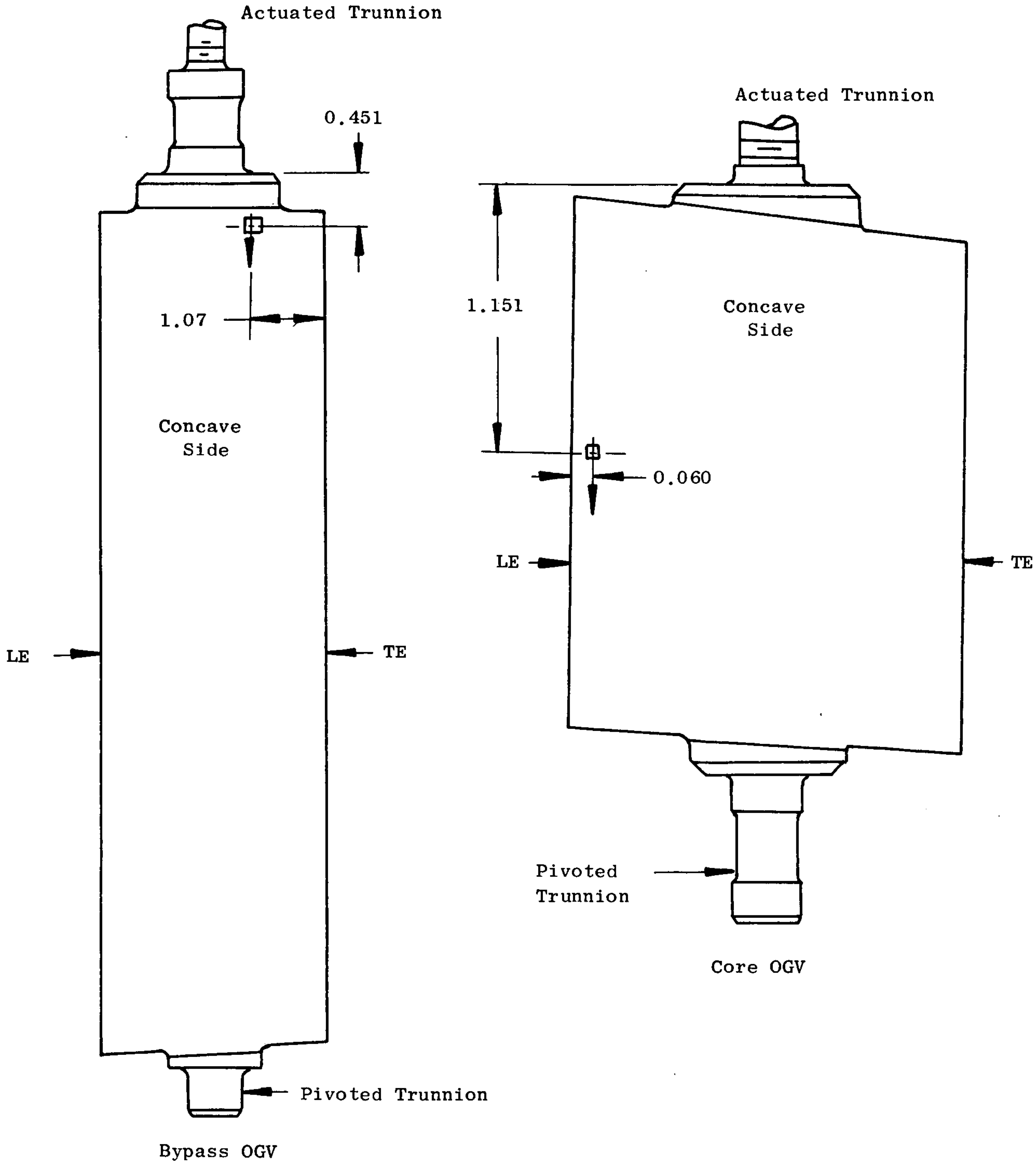

Figure 57. OGV Strain Gage Locations.

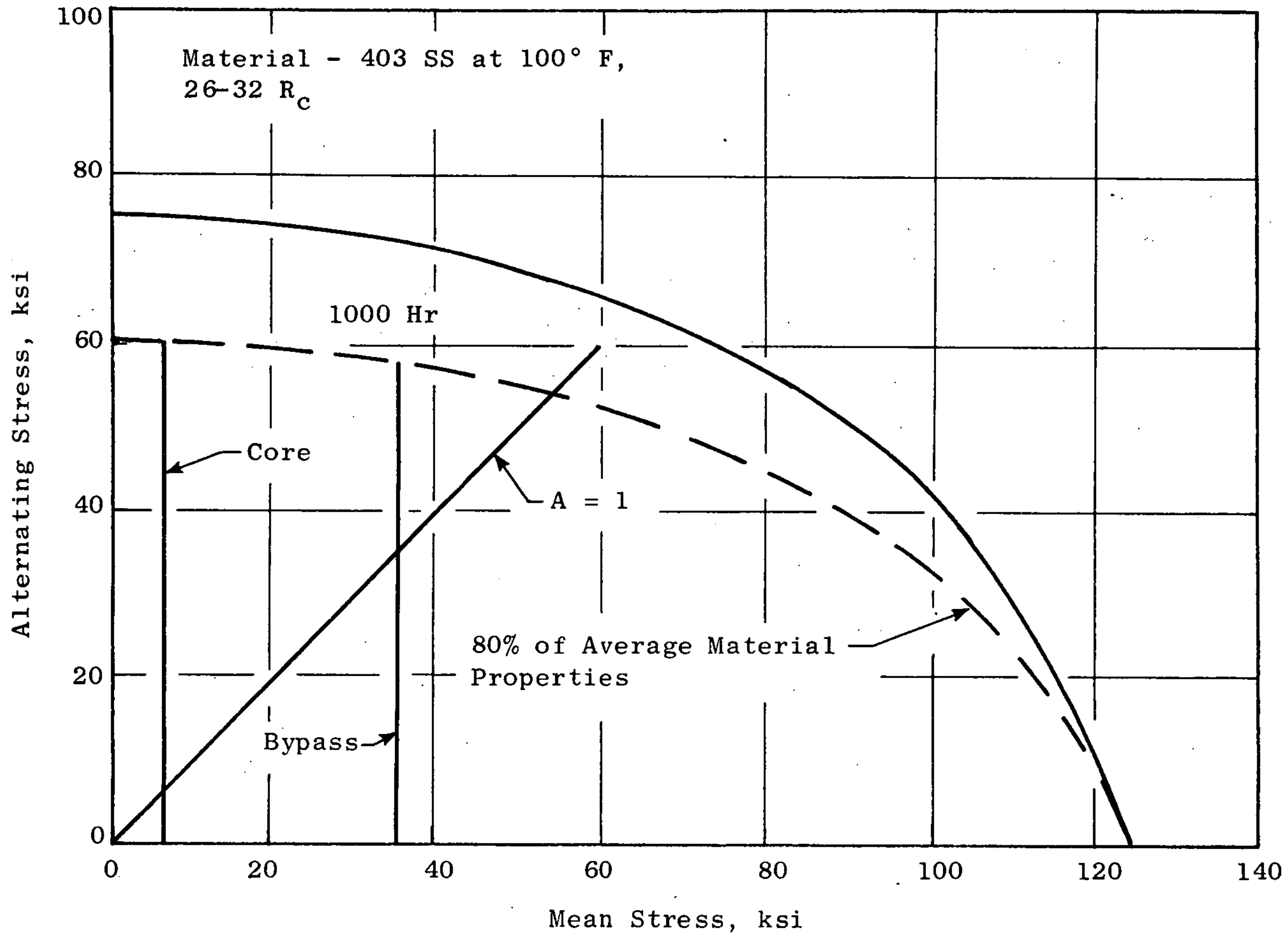

Figure 58. Goodman Diagram for OGV Scope Limit Calculations.

# IV. DISCUSSION

## A. GENERAL COMMENTS

The following discussion deals with the effect of various operating environments on the rotor blade and OGV aeromechanical characteristics. These conditions include:

- With no inlet distortion, operating (throttle) lines corresponding to several fan exhaust nozzle areas ($A_{28}$), as well as near stall.
- Various inlet distortion patterns, for the nominal operating line $A_{28}$ = 1790 in.$^2$), including tip radial, crosswind (inlet lip separation simulation, and 1/rev circumferential.
- High bypass (flow) ratio at selected corrected speeds.
- OGV angle variation at 95% speed. Note: except for this, all investigations were conducted with nominal OGV angles.
- Stall characteristics and aeromechanical response, with distorted as well as clean inlet.

Rotor blade vibratory response characteristics are presented in Figures 59 through 61 and OGV data in Figures 62 through 65. Magnitudes of inlet distortion, for the distortion patterns investigated during this program, are shown in Figure 66.

## B. BASIC AEROMECHANICAL CHARACTERISTICS WITH CLEAN (UNDISTORTED) INLET

### 1. Rotor Blades (Figure 59)

The axial location of the rotor blades far upstream of the OGV's eliminated potential integral-order excitation from the OGV's. Thus, rotor blade vibration characteristics were limited to separated flow vibration and the lower-order per-revs present in the facility inlet flow field. Details are provided as follows:

### a. Rotor Tip Shroud

Unexpectedly, the strongest rotor blade response was found to be separated flow vibration of the leading edge corner of the tip shroud. This response occurred in its lowest plate mode (about 1700 cps), and the vibratory stress was found to be quite sensitive to stage loading (see Figure 59), reaching 78% of scope limit near stall at 100% speed. The cause of this shroud vibration is not apparent, although it might be associated with recirculation.

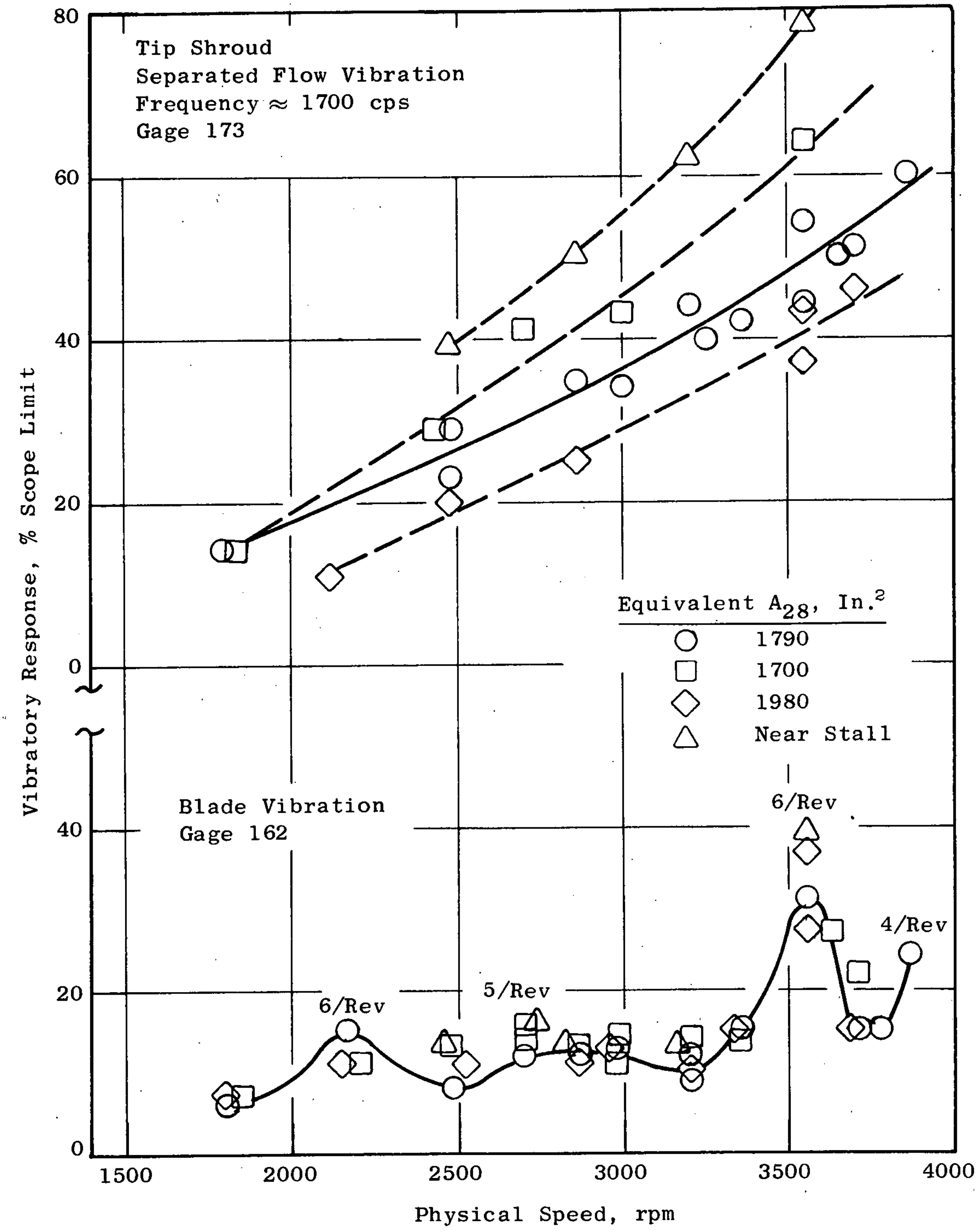

Figure 59. Rotor Blade Vibration, Clean Inlet.

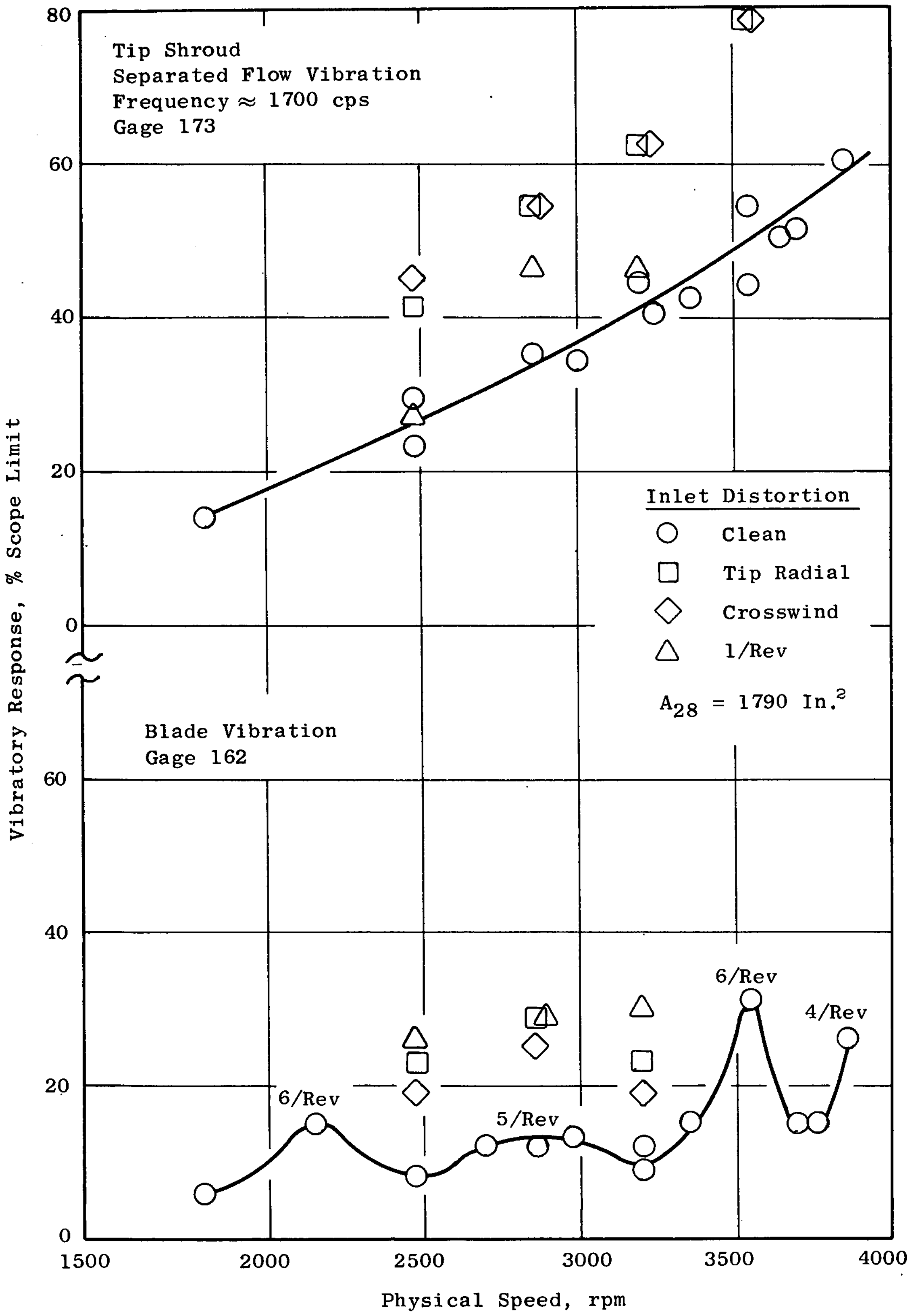

Figure 60. Rotor Blade Vibration, Effect of Inlet Distortion.

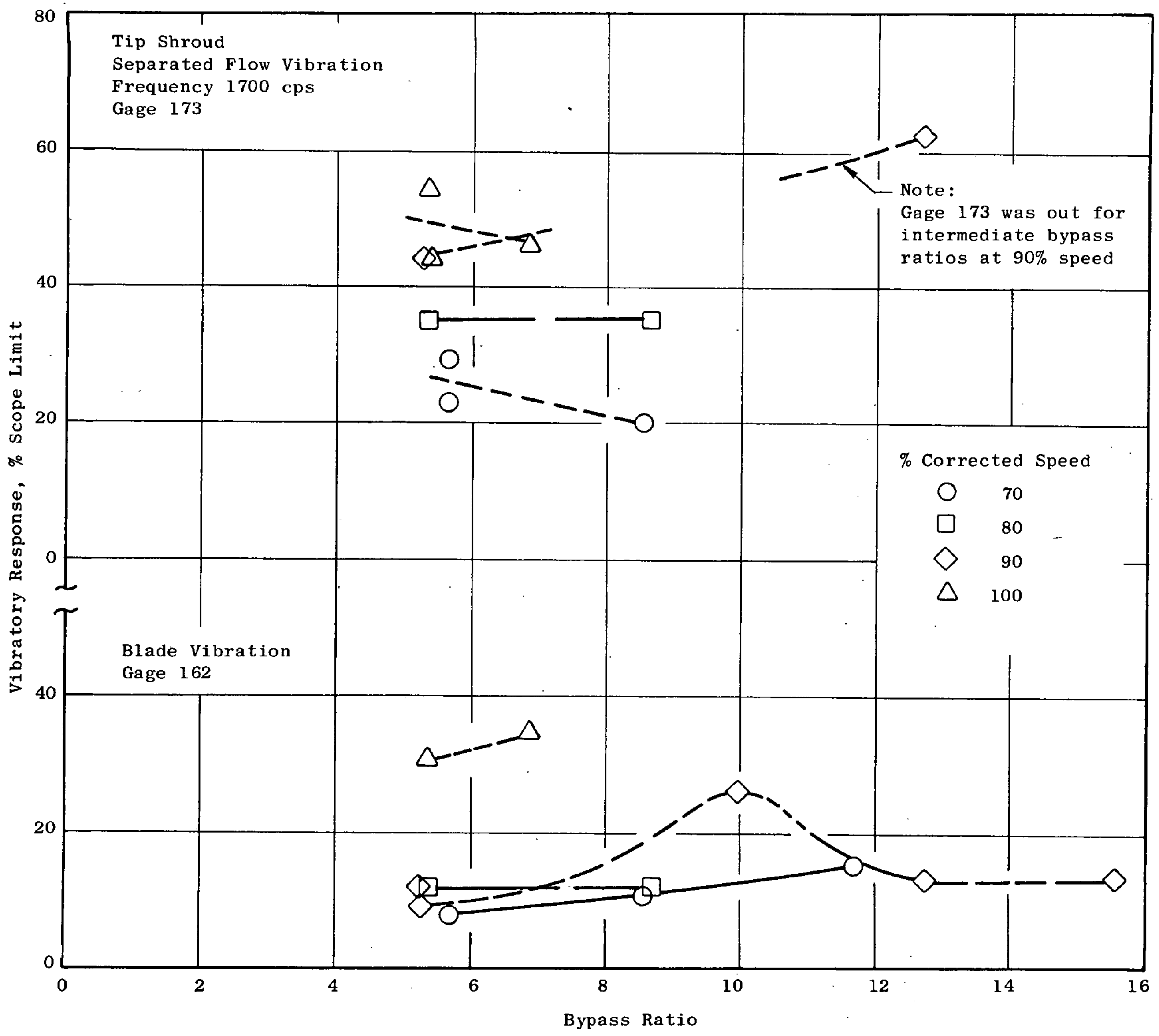

Figure 61. Rotor Blade Vibration, Effect of Bypass Ratio.

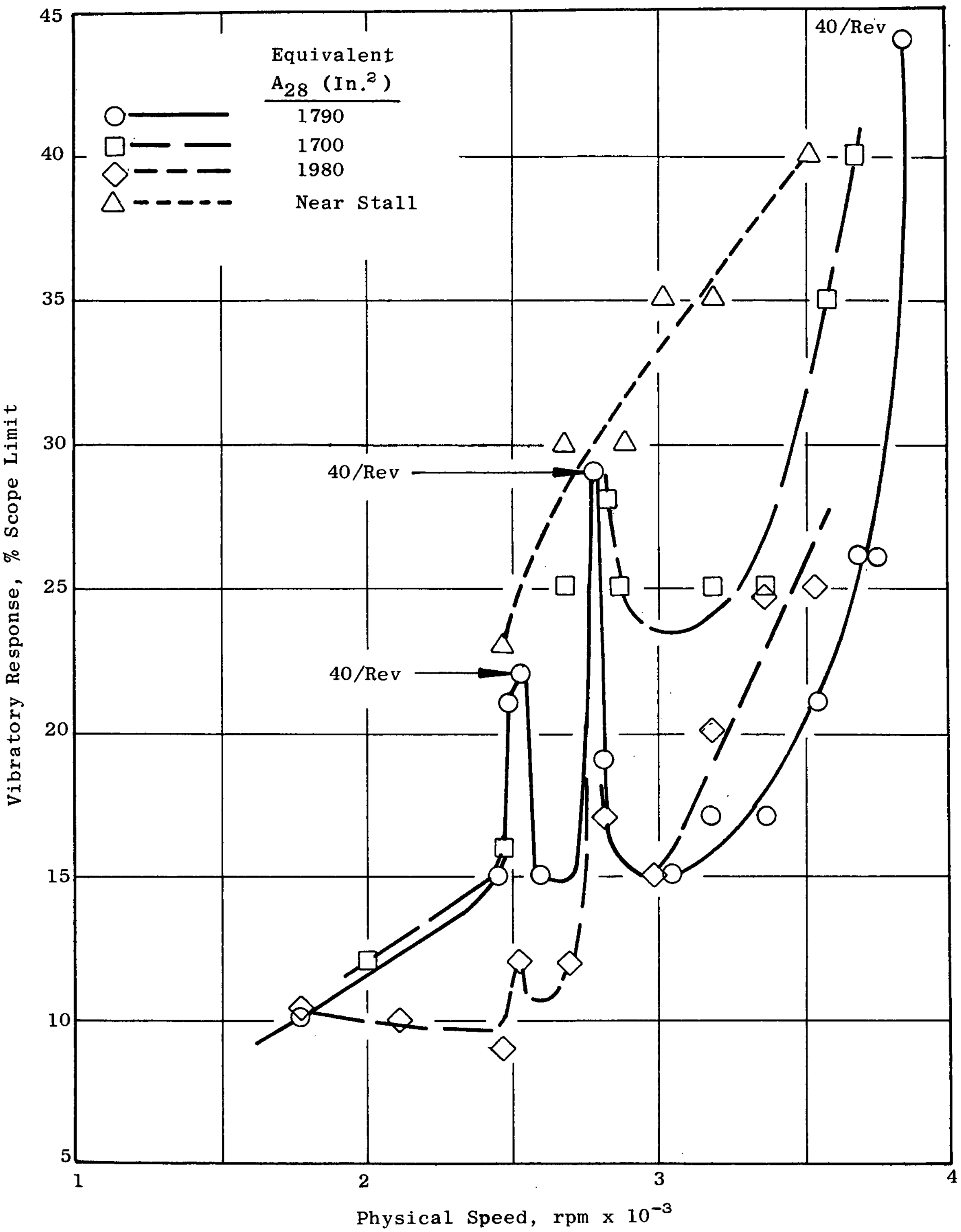

Figure 62. Fan Bypass OGV Vibration, Clean Inlet.

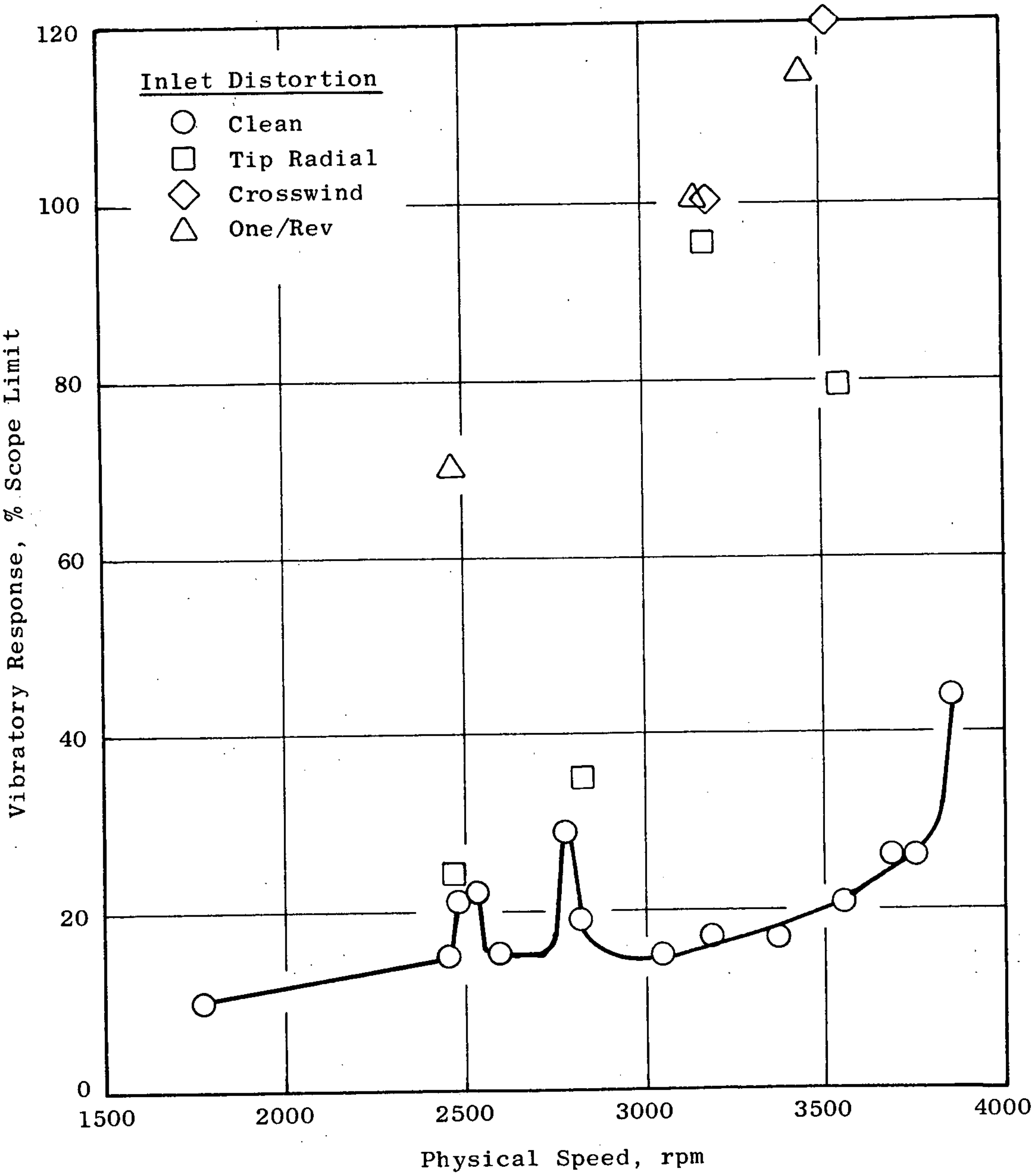

Figure 63. Fan Bypass OGV Vibration, Effect of Inlet Distortion.

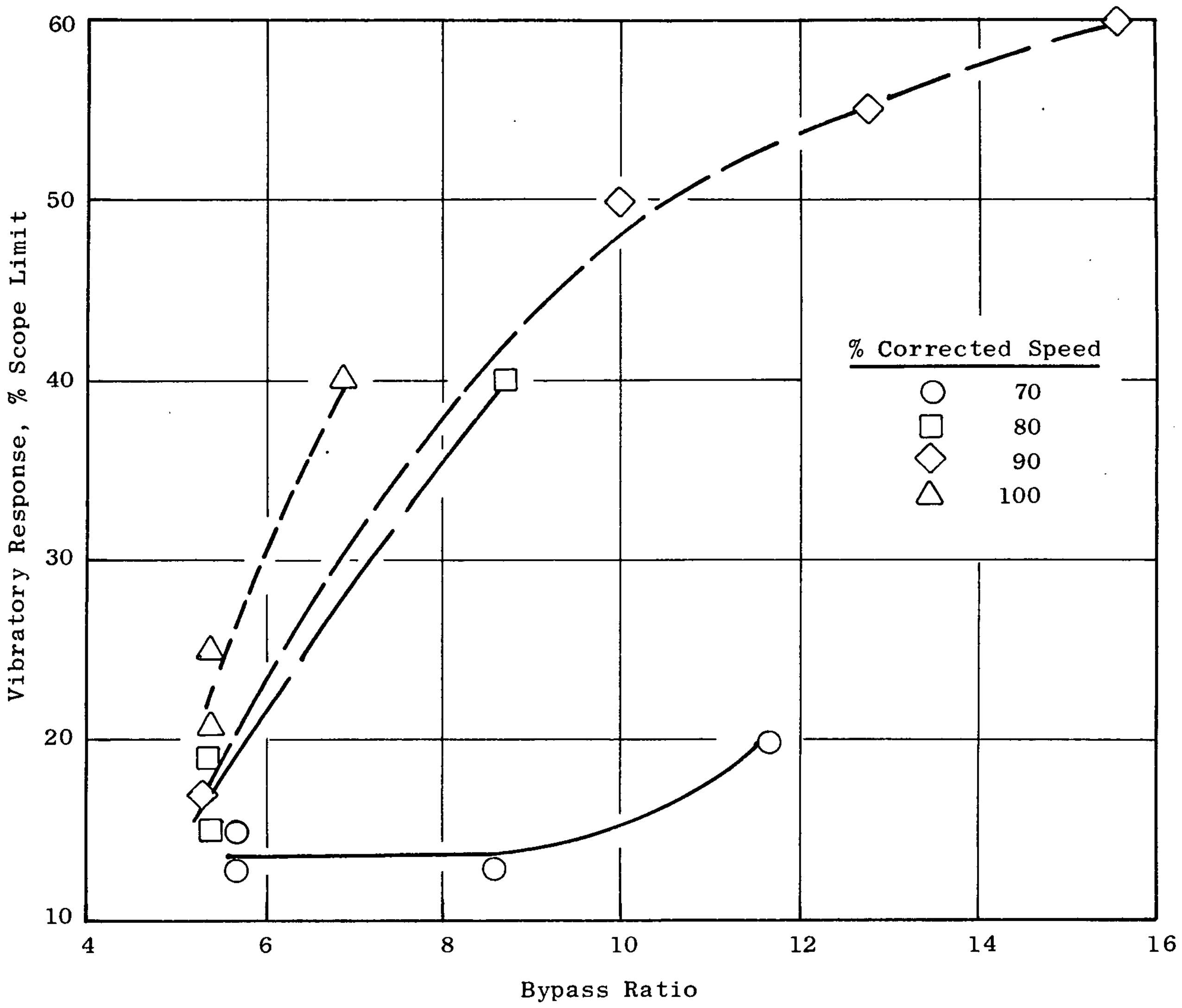

Figure 64. Fan Bypass OGV Vibration, Effect of Bypass Ratio.

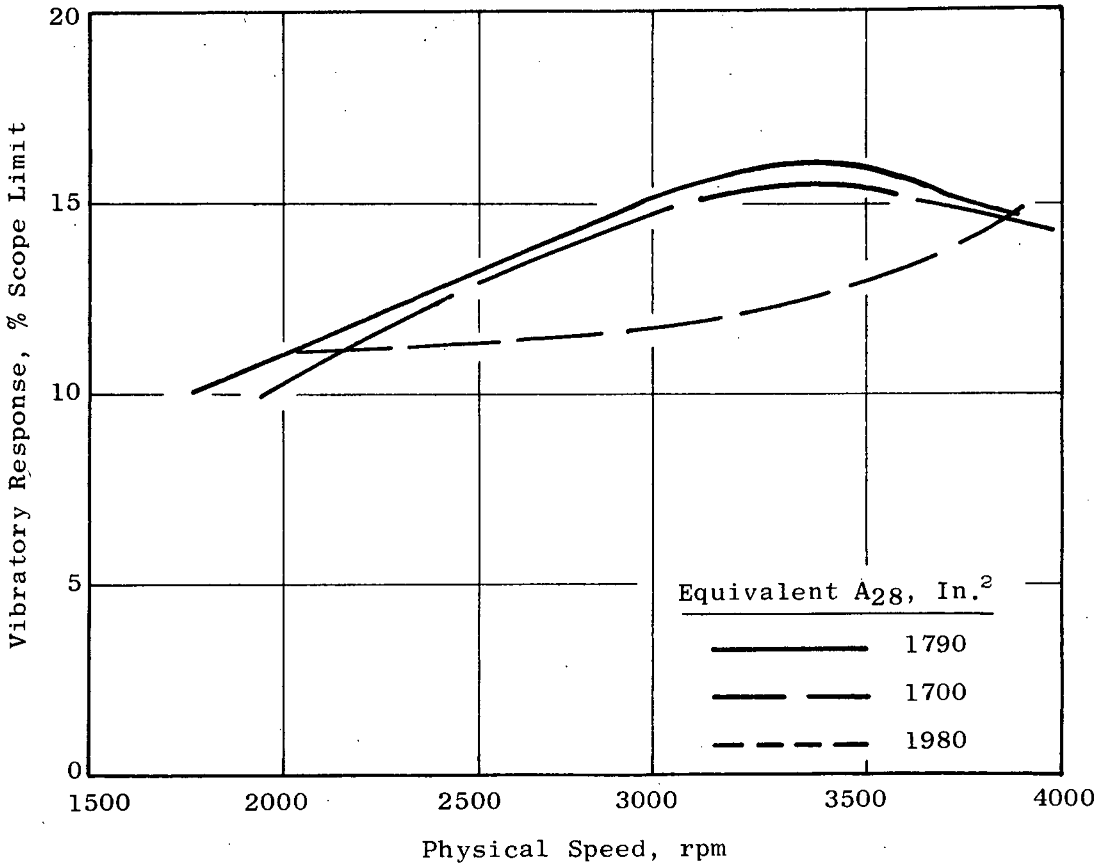

Figure 65. Fan Core OGV Vibration, Clean Inlet.

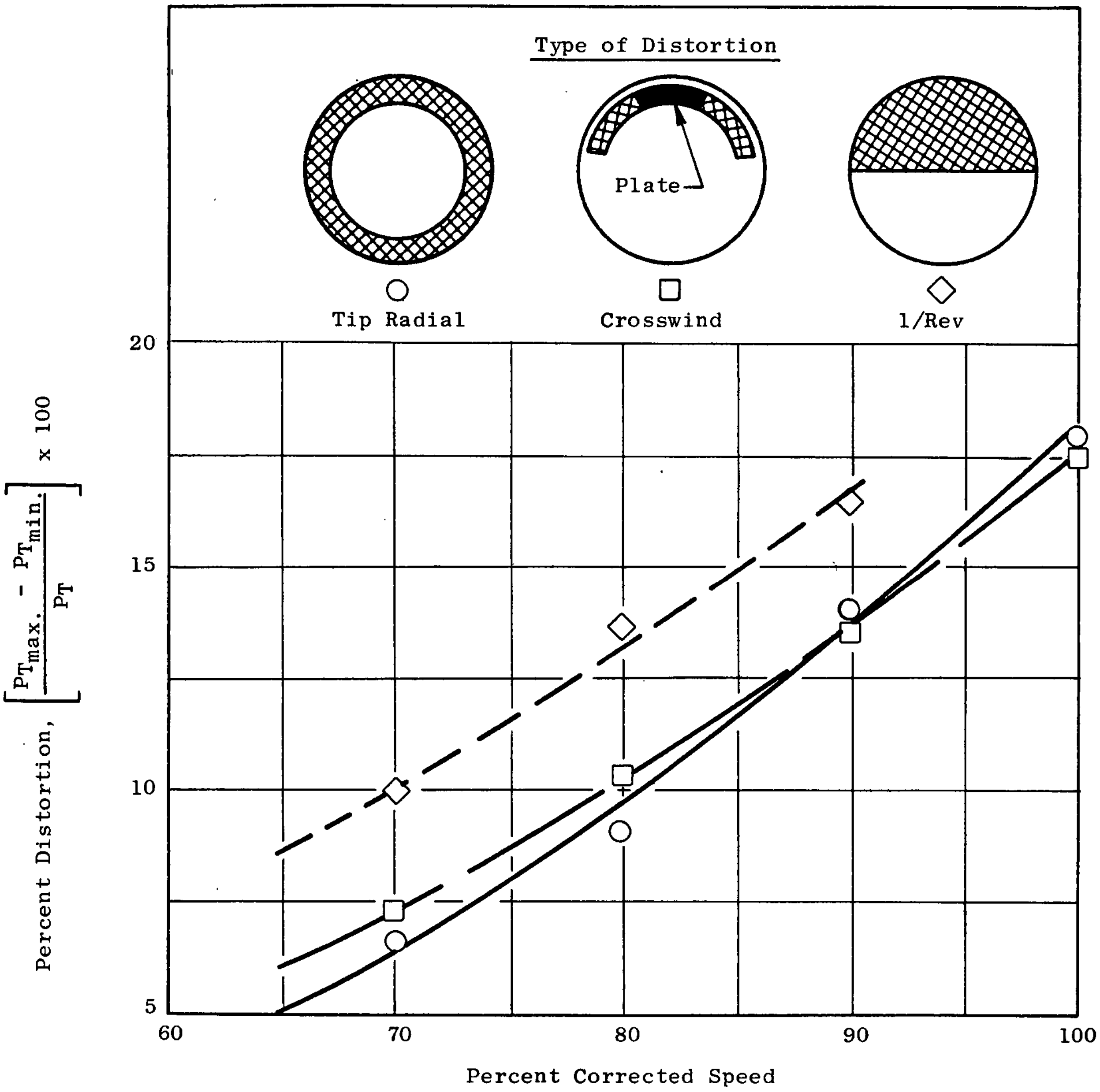

Figure 66. Inlet Distortion Magnitudes.

#### b. Rotor Blade

Aside from shroud separated flow vibration, normal rotor blade response followed a predictable pattern. As shown in Figure 59, relatively mild separated flow vibration was obtained, involving the first and second flex shrouded blade mode resonant peaks superimposed (Ref: Figure 52 for mode identification). Maximum response was experienced in the six nodal diameter resonance at 3550 rpm, with vibratory stresses remaining at a tolerable 40% scope limit, this occurring near stall. Most of the increase of integral-order resonant peaks at high pressure ratios was due to increased baseline separated flow vibration.

### 2. Fan Bypass OGV's (Figure 62)

These vanes, being downstream of the fan blades, were subjected to 40/rev rotor blade-passing excitation as well as separated flow vibration. Separated flow vibration occurred predominately in the first flex mode, with some contribution of second flex in the high speed range (see Figure 55 for mode identification). Its magnitude followed the normal pattern of increasing steadily with airflow (speed) as the turbulent energy of excitation increased. The greatly increased vibratory response near stall implies that cascade flow separation was the primary source of turbulent excitation. Superimposed on separated flow vibration were 40/rev resonant peaks for each mode which passed through 40/rev in the mid-to-high-speed range. Although these resonances were fairly strong, the most responsive one (3850 rpm) did not exceed 45% scope limit, which is considered safe for normal operation. Near stall, the grossly increased separated flow vibration levels mostly masked the 40/rev component of response. This increased vibratory stress, however, remained tolerably low (40% limit) up to 100% speed.

### 3. Fan Core OGV's (Figure 65)

Response was entirely separated flow vibration, predominately in the first flex mode (see Figure 56 for mode identification). Vibratory stress levels were very low at all operating conditions, not exceeding 16% scope limits. This minimal response is probably due to the combination of high vane stiffness, as indicated by the high first flex frequency, and mechanical damping of the vane trunnions.

## C. EFFECT OF INLET DISTORTION AND AEROMECHANICAL CHARACTERISTICS

### 1. General Comments

Inlet distortion conditions, for investigations of aerodynamic sensitivity, were simulated by inserting predetermined screen and solid-plate (where necessary) segments into the inlet flow field to produce both the desired patterns and magnitudes of total pressure variation entering the fan. The screen/plate patterns are shown in Figure 66, along with distortion magnitudes produced by them. From the aeromechanical standpoint, the only "real engine" excitations that are reasonably reproduced by screens are the lower-order harmonics of circumferential distortion patterns. Local velocities, vorticity levels and content by actual crosswinds with inlet lip separation, blow-in door airflow, reingestion during reversed thrust operation, etc. Accordingly, blade and vane aeromechanical characteristics obtained with artificially produced inlet distortion do not provide a valid indication of response magnitudes to be expected in "real" life. Of course it is necessary to monitor (and record) stresses during distortion testing as a safety precaution. The aeromechanical results of this portion of the program are discussed in the following paragraphs.

### 2. Rotor Blades (Figure 60)

Imposition of inlet distortion contributed to both tip shroud separated flow vibration as well as integral-order system mode resonances. Details are as follows:

#### a. Rotor Tip Shroud

The two distortions which were concentrated near the outer diameter (tip radial and crosswind patterns) increased shroud separated flow vibration levels by about 50%. At 100% speed the response reached 78% of scope limit with 17.5-18% distortion (Figure 66). It was found that operation along the 1700 and 1980 $in.^2$ fan exhaust nozzle throttle lines had only minor effect on shroud vibratory stress levels. Subject to verification during engine testing at Peebles, it appears that these rotor blades are aeromechanically satisfactory for engine testing with inlet distortion.

#### b. Rotor Blade

Both separated flow vibration and integral-order system mode responses were increased by the inlet distortions investigated. Stress levels were essentially doubled, but the only instance of significance was the 6/rev peak at 100% speed. Crosswind distortion of 17.5% magnitude induced 69% scope limit at 3550 rpm. Although testing with the small fan exhaust nozzle was not conducted at this speed, the relative insensitivity of stress with $A_{28}$ for other speeds indicates that significantly higher levels (than 69% limit) should not be expected. Thus, the favorable conclusion stated in Section (a), above, is further substantiated by these data.

### 3. Fan Bypass OGV's (Figure 63)

Separated flow vibration of bypass OGV's, located in the distorted portion of the flow field generated by crosswind and 1/rev distortion patterns, was increased greatly by the inlet distortions investigated (see Figure 66). With nominal $A_{28}$ (1790 $in.^2$), vane response exceeded the scope limit above 90% of design speed. However, response to tip radial distortion was somewhat less severe. Although screen circumferential positions producing maximum response of monitored OGV's were not set for operation at pressure ratios simulating $A_{28}$ = 1700 in.$^2$, relationships for $A_{28}$ = 1790 in.$^2$ indicate that response levels should reach 130-140 scope limit at 90% speed. However, as indicated in Section C1, the turbulent excitation induced by abnormal flow conditions around the edges of the distortion screens (and plate) are not representative of these experienced with actual distortions. Therefore, engine investigations under crosswind conditions are necessary in order to ascertain the problem level (if any) of OGV stress levels.

### 4. Fan Core OGV's

Core OGV vibration was completely unaffected by inlet distortion.

## D. EFFECT OF BYPASS RATIO ON AEROMECHANICAL CHARACTERISTICS

### 1. Rotor Blades (Figure 61)

The only significant effect of increased bypass ratio on rotor blade vibration was the tip shroud separated flow response. Grossly increased bypass ratio (12.8 Vs. normal 5.3) at 90% speed increased its level to 62% limit with the 1700 in.$^2$ $A_{28}$ magnitudes still falling within safe operating limits. This increase was probably induced by higher local air velocities in the tip shroud region.

### 2. Fan Bypass OGV's (Figure 64)

Separated flow vibration of the bypass OGV's was increased dramatically in the high-speed range by increased bypass ratio. The pulsing character of vane vibration suggests that the normal increase in separated flow vibration with higher air velocities was aggravated greatly by flow separation and associated turbulence from the splitter lip, separating core and bypass flow fields. Thus, operation at high bypass flow ratio would undoubtedly require attention to the splitter lip geometry. For this program, however, vibratory stresses with clean inlet did not exceed 60% scope limits at the maximum bypass ratio used (15.6 at 90% speed). High bypass ratios with inlet distortion were not investigated since this operation was not a part of the test plan.

### 3. Fan Core OGV's

Vibratory response of the core OGV's was sufficiently small that no significant effect on core OGV stress levels was discernible during high bypass ratio operation.

## E. FAN STALL CHARACTERISTICS

A summary of the stalls sustained during this program is provided in Table II. The tabulation includes identity of stall conditions, stall characteristics, and blade and vane vibratory stress levels during many of the stalls.

### 1. Clean Inlet

#### a. Stall Warning

Stalls at all speeds were preceded by appreciable aeromechanical stall warning. Primary warning was supplied by increased bypass OGV separated flow vibration with increased fan pressure ratio. Rotor tip shroud separated flow vibration also increased, but to a lesser extent.

#### b. Stall Characteristics

Stalls in the 30-95% speed range occurred as full rotating stall, the stall cell extending axially through the rotor and bypass OGV's. At 100% $N_c$, however, throttling toward stall was aborted when bypass OGV separated flow vibration had reached 120% scope limit. Further indication of mismatch of rotor and bypass OGV aerodynamic loading near stall at high speeds is indicated by the onset of local rotating stall in the bypass OGV's immediately prior to full rotating stall (see Table II).

#### c. Stall Stress

Vibratory response of the blading was not severe, exceeding scope limits appreciably only on the bypass OGV's during the 90 and 95% speed stalls (150 and 180% limit, respectively - see Table II). However, fatigue damage to the vanes was negligible, since stalls were cleared expeditiously, and the number of high stress vibration cycles was thus very few. Rotor tip shroud stress barely exceeded scope limits during the 95% speed stall, and core OGV vibration was essentially unaffected by stalls.

#### d. Stall at High Bypass Ratio

The only stall sustained at high bypass ratios was at 70% speed with 10.25 bypass ratio. It was very mild and occurred as rotor blade rotating stall, bypass OGV's not being involved. Implications of this stall characteristic for other speeds, however, are not apparent.

### 2. Tip Radial Distortion

The most significant influence of tip radial distortion on stall characteristics involved the way in which stall occurred. Increased

## Table II. Stall Summary.

| Date | $IN_c$ | RPM | OGV Angle | $P_{T2}$ ("Hg) | Inlet Distortion At Stall |  | M/BP*** DV (% Open) | Type** of Stall | Stall Stress**** (% Scope Limits) |  |  | Comments |
|---|---|---|---|---|---|---|---|---|---|---|---|---|
|  |  |  |  |  | Type | %* |  |  | Rotor 1F Mode | Rotor Tip Shroud | Bypass OGV's |  |
| 11/23/70 | 50 | 1793 | 0 | 30 | Clean | 0 | 33/26 | RS |  |  |  |  |
|  | 70 | 2488 | 0 | 30 | Clean | 0 | 42/28.7 | RS |  |  |  |  |
|  | 70 | 2488 | 0 | 30 | Clean | 0 | 39/30.1 | RS |  |  |  |  |
|  | 90 | 3199 | 0 | 30 | Clean | 0 | 49.4/30 | RS |  | 100 | 150 |  |
| 11/24/70 | 100 | 3545 | 0 | 30 | Clean | 0 | 52/32 | SS |  |  | 120 | No rotor stall - OGV stress limit |
|  | 95 | 3370 | 0 | 30 | Clean | 0 | 48.1/30.6 | RS | 50 | 120 | 180 | B.P. OGV's stalled at 48.1/31.5 |
|  | 60 | 2119 | 0 | 30 | Clean | 0 | 38/30.4 | RS | 25 | 23 | 50 |  |
|  | 30 | 1058 | 0 | 30 | Clean | 0 | 34/30 | RS |  |  |  |  |
| 12/04/70 | 75 | 2689 | 0 | 30 | Clean | 0 | 43/32.8 | RS | 11 | 17 | 105 |  |
|  | 80 | 2866 | 0 | 30 | Clean | 0 | 43/32.9 | RS | 28 | 20 | 92 |  |
|  | 85 | 3036 | 0 | 30 | Clean | 0 | 45/32.9 | RS | 40 |  | 115 |  |
|  | 70 | 2493 | 0 | 30 | Clean | 0 | 17.8/36 | RS |  |  |  | High B.P. Ratio (10.25) rotor stall; no stator stall |
| 12/16/70 | 90 | 3173 | 0 | 30 | Tip Radial | 14 | 41.8/41 | SS |  |  | 110 | No rotor stall - only B.P. OGV's |
|  | 90 | 3173 | 0 | 30 | Tip Radial | 14 | 86/41.1 | RS | 35 | 54 | 110 | B.P. OGV's stall at 95/41.8 |
|  | 70 | 2468 | 0 | 30 | Tip Radial | 7 | 63/40.5 | RS | 12 | 35 | 72 |  |
|  | 80 | 2820 | 0 | 30 | Tip Radial | 9 | 65/41.1 | RS | 40 | 46 | 78 | Preceded by bypass OGV stall at 65/44 |
|  | 80 | 2820 | 0 | 30 | Tip Radial | 9 | 65/42 | RS |  |  |  | B.P. OGV's stall at 65/44 DV |
|  | 100 | 3529 | 0 | 30 | Tip Radial | 17 | 78/41.1 | B/P OGV Stress Limit |  |  | 110 | No rotor stall |
| 12/18/70 | 70 | 2470 | 0 | 30 | Crosswind | 6 | 53/36.1 | RS |  |  |  |  |
|  | 90 | 3182 | 0 | 30 | Crosswind | 11 | 70/36.6 | RS | 50 |  | 113 |  |
|  | 90 | 3179 | 0 | 30 | Crosswind | 11 | 65/36.2 | RS | 40 | 63 | 167 | 197° screen position |
|  | 90 | 3123 | 0 | 30 | Crosswind | 11 | 65/36.3 | RS |  |  |  | 275° screen position |
|  | 90 | 3173 | 0 | 30 | Crosswind | 11 | 65/36.5 | RS |  |  |  | 90° screen position |
|  | 80 | 2817 | 0 | 30 | Crosswind | 7 | 60/36.2 | RS | 36 |  | 105 |  |
|  | 70 | 2465 | 0 | 30 | Crosswind | 6 | 53/36.1 | RS | 29 |  | 60 |  |
| 12/21/70 | 90 | 3176 | 0 | 30 | 1/Rev | 11 | 65/37.6 | B/P OGV Stress Limit |  |  | 90 | No rotor stall |
|  | 70 | 2455 | 0 | 30 | 1/Rev | 6 | 48/37.4 | RS | 27 |  | 77 |  |
|  | 80 | 2808 | 0 | 30 | 1/Rev | 8 | 63/38 | RS | 33 |  | 100 |  |
|  | 90 | 3154 | 0 | 30 | 1/Rev | 11 | 65/38 | B/P OGV Stress Limit |  |  | 110 | No rotor stall |
|  | 50 | 1749 | 0 | 30 | Clean with Egg Crate | 0 | 36/32.4 | RS |  |  |  |  |
|  | 70 | 2447 | 0 | 30 |  | 0 | 44/33.3 | RS |  |  |  |  |
|  | 80 | 2797 | 0 | 30 |  | 0 | 48/33.7 | RS |  |  | 50 |  |
|  | 90 | 3149 | 0 | 30 |  | 0 | 54.5/33.5 | RS |  |  | 70 |  |
| 12/29/70 | 70 | 2458 | 0 | 30 | Clean | 0 | 43/32.8 | RS | 22 | 28 | 55 |  |

*% Distortion = $\dfrac{P_{Tmax} - P_{Tmin}}{P_{Tmax}}$ x 100: See Figure 66

**RS = Full rotating stall; SS = Bypass OGV stall (only)

***M/BP: Main (core)/Bypass discharge throttle valve positions

****Core OGV's did not respond appreciably during stall loading on the bypass OGV's was evidenced by the onset of local rotating stall in the OGV's prior to full rotating stall (both rotor and OGV) as low as 80% speed. Throttling toward stall at 100% speed was still limited by excessive OGV separated flow vibration levels. Stall-induced vibratory stress levels were similar to, or perhaps slightly lower than, those experienced with clean inlet.

### 3. Crosswind Distortion

Stalls with this distortion were not conducted above 90% speed due to excessive vibratory response of bypass OGV's located in the distorted part of the flow field (see Section C3). All stalls encountered were similar to those with clean inlet, occurring as full rotating stall. Blade and vane vibratory stress levels were also similar. As indicated in Section C3, raising the fan pressure ratio toward stall increased bypass OGV separated flow vibration considerably, thus providing ample aeromechanical warning of impending stall.

### 4. 1/Rev Distortion

Although the magnitude of 1/rev distortion was somewhat stronger than for the crosswind pattern (Figure 66), similar bypass OGV separated flow vibratory stress levels were experienced while throttling toward stall. However, throttling with 1/rev distortion was aborted short of stall at 90% speed as a precautionary safety measure (Table II). Stall characteristics and stress levels essentially duplicated those obtained with crosswind distortion.

## F. EFFECT OF FAN OGV ANGLE

The only explorations involving bypass OGV angle variation were conducted at 95% speed at a pressure ratio corresponding to $A_{28} = 1790$ in.$^2$ The OGV's were moved ± 4 degrees from nominal angle to search for the aerodynamically optimum value. During these modest angle gyrations neither rotor blade nor OGV aeromechanical characteristics were significantly affected.

# LIST OF SYMBOLS

| | |
|---|---|
| $A_t$ | throttle area, nozzle throat area required to pass measured weight flow assuming isentropic expansion from measured discharge total pressure and total temperature to ambient static pressure, $ft^2$ |
| BPR | bypass ratio |
| B/U | build up |
| $C_p$ | static-pressure-rise coefficient, $\Delta p/q^*$ |
| DV | Discharge Valve |
| $N$ | rotational speed, rpm |
| $P$ | total pressure, psia |
| $p$ | static pressure, psia |
| $\Delta p$ | static pressure rise across OGV, psia |
| $q^*$ | $P - p$, psia |
| $R$ | radius, in. |
| $T$ | total temperature, °R |
| $V$ | velocity, ft/sec |
| $W$ | weight flow, lb/sec |
| $\alpha$ | absolute air angle, deg |
| $\beta$ | relative air angle, deg |
| $\delta$ | ratio: $-\ \frac{\text{total pressure}}{\text{standard pressure}},\ \frac{\text{psia}}{14.696\ \text{psia}}$ |
| $\eta$ | efficiency |
| $\theta$ | ratio: $-\ \frac{\text{total temperature}}{\text{standard temperature}},\ \frac{°\text{R}}{518.688°\text{R}}$ |
| $\lambda$ | effective-area coefficient |
| $\psi$ | stream function, percent flow passing between O.D. and point of interest, $\psi_{O.D.} = 0$, $\psi_{I.D.} = 1$ |
| $\overline{\omega}$ | total-pressure-loss coefficient |

Subscripts:

| | |
|---|---|
| Ad | adiabatic |
| fs | free stream |
| 1 | local |
| max | maximum |
| OGV | outlet guide vane |
| 2 | fan inlet |
| 2c | fan inlet, core portion |
| 23 | fan discharge, bypass portion |
| 24 | fan discharge, core portion |